UNIVERSIDADE ESTADUAL DE CAMPINAS
INSTITUTO DE QUÍMICA

RAUL BRUNO MACHADO DA SILVA

CeO_x-ZrO_2 POROUS NANORODS DECORATED WITH Au NANOPARTICLES FOR THE CATALYSIS OF PREFERENTIAL OXIDATION OF CARBON MONOXIDE (PROX-CO)

NANOBASTÕES POROSOS DE CeO_2-ZrO_x DECORADOS COM NANOPARTÍCULAS DE OURO PARA A CATÁLISE DA REAÇÃO DE OXIDAÇÃO PREFERENCIAL DE MONÓXIDO DE CARBONO

CAMPINAS
2020

RAUL BRUNO MACHADO DA SILVA

CeO_X-ZrO_2 POROUS NANORODS DECORATED WITH Au NANOPARTICLES FOR THE CATALYSIS OF PREFERENTIAL OXIDATION OF CARBON MONOXIDE (PROX-CO)

NANOBASTÕES POROSOS DE CeO_2-ZrO_X DECORADOS COM NANOPARTÍCULAS DE OURO PARA A CATÁLISE DA REAÇÃO DE OXIDAÇÃO PREFERENCIAL DE MONÓXIDO DE CARBONO

Dissertação de Mestrado apresentada ao Instituto de Química da Universidade Estadual de Campinas como parte dos requisitos exigidos para a obtenção do título de Mestre em Química na área de Química Inorgânica.

Master's Dissertation presented to the Institute of Chemistry of the University of Campinas as part of the requirements to obtain the title of Master of Chemistry in the area of Inorganic Chemistry.

Supervisor: Prof. Dr. Italo Odone Mazali

O arquivo digital corresponde à versão final da Dissertação defendida pelo aluno Raul Bruno Machado da Silva e orientada pelo Prof. Dr. Italo Odone Mazali.

CAMPINAS

2020

Ficha catalográfica
Universidade Estadual de Campinas
Biblioteca do Instituto de Química
Simone Luiz Alves - CRB 8/9094

Si38c

Silva, Raul Bruno Machado da, 1994-
CeO_x-ZrO_2 porous nanorods decorated with Au nanoparticles for the catalysis of preferential oxidation of carbon monoxide (PrOX-CO) / Raul Bruno Machado da Silva. – Campinas, SP : [s.n.], 2020.

Orientador: Italo Odone Mazali.
Dissertação (mestrado) – Universidade Estadual de Campinas, Instituto de Química.

1. Catálise. 2. Ouro. 3. Óxidos de cério. 4. Oxidação preferencial de CO. 5. Nanotecnologia. I. Mazali, Italo Odone, 1972-. II. Universidade Estadual de Campinas. Instituto de Química. III. Título.

Informações para Biblioteca Digital

Título em outro idioma: Nanobastões porosos de CeO2-ZrOx decorados com nanopartículas de ouro para a catálise da reação de oxidação preferencial de monóxido de carbono
Palavras-chave em inglês:
Catalysis
Gold
Cerium oxide
Preferential CO oxidation
Nanotechnology
Área de concentração: Química Inorgânica
Titulação: Mestre em Química na área de Química Inorgânica
Banca examinadora:
Italo Odone Mazali [Orientador]
Juliana dos Santos de Souza
Pedro Paulo Corbi
Data de defesa: 17-01-2020
Programa de Pós-Graduação: Química

Identificação e informações acadêmicas do(a) aluno(a)
- ORCID do autor: https://orcid.org/0000-0002-8659-4617
- Currículo Lattes do autor: http://lattes.cnpq.br/4634574905178731

BANCA EXAMINADORA

Prof. Dr. Italo Odone Mazali (Orientador) (IQ – UNICAMP)

Profa. Dra. Juliana dos Santos de Souza (CCNH – UFABC)

Prof. Dr. Pedro Paulo Corbi (IQ – UNICAMP)

A Ata da defesa com as respectivas assinaturas dos membros da Comissão Examinadora encontra-se no SIGA/Sistema de Fluxo de Dissertação e Tese e na Secretaria do Programa da Unidade.

Este exemplar corresponde à redação final da Dissertação de Mestrado defendida pelo(a) aluno(a) **RAUL BRUNO MACHADO DA SILVA**, aprovado pela Comissão Julgadora no dia 17 de janeiro de 2020.

DEDICATION

The solitude of Latin America

By Gabriel Garcia Marquéz (1927 – 2014)

Nobel Lecture - 8 December, 1982, at the Royal Swedish Academy

Antonio Pigafetta, a Florentine navigator who went with Magellan on the first voyage around the world, wrote, upon his passage through our southern lands of America, a strictly accurate account that nonetheless resembles a venture into fantasy. In it he recorded that he had seen hogs with navels on their haunches, clawless birds whose hens laid eggs on the backs of their mates, and others still, resembling tongueless pelicans, with beaks like spoons. He wrote of having seen a misbegotten creature with the head and ears of a mule, a camel's body, the legs of a deer and the whinny of a horse. He described how the first native encountered in Patagonia was confronted with a mirror, whereupon that impassioned giant lost his senses to the terror of his own image.

This short and fascinating book, which even then contained the seeds of our present-day novels, is by no means the most staggering account of our reality in that age. The Chronicles of the Indies left us countless others. Eldorado, our so avidly sought and illusory land, appeared on numerous maps for many a long year, shifting its place and form to suit the fantasy of cartographers. In his search for the fountain of eternal youth, the mythical Alvar Núñez Cabeza de Vaca explored the north of Mexico for eight years, in a deluded expedition whose members devoured each other and only five of whom returned, of the six hundred who had undertaken it. One of the many unfathomed mysteries of that age is that of the eleven thousand mules, each loaded with one hundred pounds of gold that left Cuzco one day to pay the ransom of Atahualpa and never reached their destination. Subsequently, in colonial times, hens were sold in Cartagena de Indias, that had been raised on alluvial land and whose gizzards contained tiny lumps of gold. One founder's lust for gold beset us until recently. As late as the last century, a German mission appointed to study the construction of an interoceanic railroad across the Isthmus of Panama concluded

that the project was feasible on one condition: that the rails not be made of iron, which was scarce in the region, but of gold.

Our independence from Spanish domination did not put us beyond the reach of madness. General Antonio López de Santa Anna, three times dictator of Mexico, held a magnificent funeral for the right leg he had lost in the so-called Pastry War. General Gabriel García Moreno ruled Ecuador for sixteen years as an absolute monarch; at his wake, the corpse was seated on the presidential chair, decked out in full-dress uniform and a protective layer of medals. General Maximiliano Hernández Martínez, the theosophical despot of El Salvador who had thirty thousand peasants slaughtered in a savage massacre, invented a pendulum to detect poison in his food, and had streetlamps draped in red paper to defeat an epidemic of scarlet fever. The statue to General Francisco Moraz´n erected in the main square of Tegucigalpa is actually one of Marshal Ney, purchased at a Paris warehouse of second-hand sculptures.

Eleven years ago, the Chilean Pablo Neruda, one of the outstanding poets of our time, enlightened this audience with his word. Since then, the Europeans of good will – and sometimes those of bad, as well – have been struck, with ever greater force, by the unearthly tidings of Latin America, that boundless realm of haunted men and historic women, whose unending obstinacy blurs into legend. We have not had a moment's rest. A promethean president, entrenched in his burning palace, died fighting an entire army, alone; and two suspicious airplane accidents, yet to be explained, cut short the life of another great-hearted president and that of a democratic soldier who had revived the dignity of his people. There have been five wars and seventeen military coups; there emerged a diabolic dictator who is carrying out, in God's name, the first Latin American ethnocide of our time. In the meantime, twenty million Latin American children died before the age of one – more than have been born in Europe since 1970. Those missing because of repression number nearly one hundred and twenty thousand, which is as if no one could account for all the inhabitants of Uppsala. Numerous women arrested while pregnant have given birth in Argentine prisons, yet nobody knows the whereabouts and identity of their children who were furtively adopted or sent to an orphanage by order of the military authorities. Because they tried to change this state of things, nearly two hundred thousand men and women have died throughout the continent, and over one hundred thousand have lost their lives in three small and ill-fated countries of Central

America: Nicaragua, El Salvador and Guatemala. If this had happened in the United States, the corresponding figure would be that of one million six hundred thousand violent deaths in four years.

One million people have fled Chile, a country with a tradition of hospitality – that is, ten per cent of its population. Uruguay, a tiny nation of two and a half million inhabitants which considered itself the continent's most civilized country, has lost to exile one out of every five citizens. Since 1979, the civil war in El Salvador has produced almost one refugee every twenty minutes. The country that could be formed of all the exiles and forced emigrants of Latin America would have a population larger than that of Norway.

I dare to think that it is this outsized reality, and not just its literary expression, that has deserved the attention of the Swedish Academy of Letters. A reality not of paper, but one that lives within us and determines each instant of our countless daily deaths, and that nourishes a source of insatiable creativity, full of sorrow and beauty, of which this roving and nostalgic Colombian is but one cipher more, singled out by fortune. Poets and beggars, musicians and prophets, warriors and scoundrels, all creatures of that unbridled reality, we have had to ask but little of imagination, for our crucial problem has been a lack of conventional means to render our lives believable. This, my friends, is the crux of our solitude.

And if these difficulties, whose essence we share, hinder us, it is understandable that the rational talents on this side of the world, exalted in the contemplation of their own cultures, should have found themselves without valid means to interpret us. It is only natural that they insist on measuring us with the yardstick that they use for themselves, forgetting that the ravages of life are not the same for all, and that the quest of our own identity is just as arduous and bloody for us as it was for them. The interpretation of our reality through patterns not our own, serves only to make us ever more unknown, ever less free, ever more solitary. Venerable Europe would perhaps be more perceptive if it tried to see us in its own past. If only it recalled that London took three hundred years to build its first city wall, and three hundred years more to acquire a bishop; that Rome laboured in a gloom of uncertainty for twenty centuries, until an Etruscan King anchored it in history; and that the peaceful Swiss of today, who feast us with their mild cheeses and apathetic watches, bloodied Europe as soldiers of fortune, as late as the Sixteenth Century. Even at the height of the Renaissance, twelve thousand lansquenets in the pay of

the imperial armies sacked and devastated Rome and put eight thousand of its inhabitants to the sword.

I do not mean to embody the illusions of Tonio Kröger, whose dreams of uniting a chaste north to a passionate south were exalted here, fifty-three years ago, by Thomas Mann. But I do believe that those clear-sighted Europeans who struggle, here as well, for a more just and humane homeland, could help us far better if they reconsidered their way of seeing us. Solidarity with our dreams will not make us feel less alone, as long as it is not translated into concrete acts of legitimate support for all the peoples that assume the illusion of having a life of their own in the distribution of the world.

Latin America neither wants, nor has any reason, to be a pawn without a will of its own; nor is it merely wishful thinking that its quest for independence and originality should become a Western aspiration. However, the navigational advances that have narrowed such distances between our Americas and Europe seem, conversely, to have accentuated our cultural remoteness. Why is the originality so readily granted us in literature so mistrustfully denied us in our difficult attempts at social change? Why think that the social justice sought by progressive Europeans for their own countries cannot also be a goal for Latin America, with different methods for dissimilar conditions? No: the immeasurable violence and pain of our history are the result of age-old inequities and untold bitterness, and not a conspiracy plotted three thousand leagues from our home. But many European leaders and thinkers have thought so, with the childishness of old-timers who have forgotten the fruitful excess of their youth as if it were impossible to find another destiny than to live at the mercy of the two great masters of the world. This, my friends, is the very scale of our solitude.

In spite of this, to oppression, plundering and abandonment, we respond with life. Neither floods nor plagues, famines nor cataclysms, nor even the eternal wars of century upon century, have been able to subdue the persistent advantage of life over death. An advantage that grows and quickens: every year, there are seventy-four million more births than deaths, a sufficient number of new lives to multiply, each year, the population of New York sevenfold. Most of these births occur in the countries of least resources – including, of course, those of Latin America. Conversely, the most prosperous countries have succeeded in accumulating powers of destruction such as to annihilate, a hundred times over, not only all the human

beings that have existed to this day, but also the totality of all living beings that have ever drawn breath on this planet of misfortune.

On a day like today, my master William Faulkner said, “I decline to accept the end of man”. I would fall unworthy of standing in this place that was his, if I were not fully aware that the colossal tragedy he refused to recognize thirty-two years ago is now, for the first time since the beginning of humanity, nothing more than a simple scientific possibility. Faced with this awesome reality that must have seemed a mere utopia through all of human time, we, the inventors of tales, who will believe anything, feel entitled to believe that it is not yet too late to engage in the creation of the opposite utopia. A new and sweeping utopia of life, where no one will be able to decide for others how they die, where love will prove true and happiness be possible, and where the races condemned to one hundred years of solitude will have, at last and forever, a second opportunity on earth.

"Science is a cooperative enterprise, spanning the generations. It's the passing of a torch from teacher, to student, to teacher. A community of minds reaching back to antiquity and forward to the stars."

Neil deGrasse Tyson (1958 -), American astrophysicist

Dedicated at first to all my family and, in special, to my parents, Isaac and Damiana, for being my safe haven at the most difficult and tortuous times, and secondly to all the people in my life who have shown me that questioning is the only way to find freedom.

.

ACKNOWLEDGEMENTS

I devote a sincere thanks to my advisor, Prof. Dr. Italo Odone Mazali, to whom I dedicate my *grazie de cuore* for his guidance, attention, ideas and corrections. His enthusiasm for science and his detail-oriented zeal are his great driving forces.

I also dedicate a thank you to Prof. Dr. Fernando Aparecido Sigoli, who together with Prof. Italo, coordinates the Functional Materials Laboratory. I leave here my thanks for the scientific and professional contributions.

I am aware that my personal formation is a result of a domino effect who traces back to my earliest days, and for this, I would like to leave an important thanks to Emanuel Maciel, Sérgio Matos, Antonino Fontenele and Regina Celi, my teachers in Fortaleza, who allowed me to delve deeper early in to more advanced Chemistry topics and instigated me to the scientific thinking process and fostered in me the desire to always look beyond.

I would like to give special thanks to all the Chemistry Institute employees whose names, faces, and histories are often unfortunately unknown to the vast majority of the academic community, but who are essential for scientific research performed at the institute, from the most elemental to the most complex.

I would also like to thank some of the Chemistry Institute technicians, like Claudia Martelli (UV-VIS), Milene Martins (Raman) and Deborah Simoni (XRD), for your patience, kindness and for helping me out in performing the isoelectric point, Raman Spectroscopy and X-ray Diffraction measurements found in this work.

I would like to thank my LMF co-workers for the company and all the good time I spent during my stay at the lab. Adriana, Amanda, Anerise, Cláudia, Edison, Filipe, Gesiane, Isabela, Isaias, Jaciara, Lanousse, Lohana, Raisa, Rafael, Rodrigo, Sérgio, Tainá and William, whose contributions varied in intensity and presence, but which in the whole, were very important for me and contributed to this work.

One special thanks to the trinity of my lab friends which is composed by the women who are amidst the strongest I have ever met in my life. Flávia, thank you for being a daily dose of inspiration, for running along my side and teaching me that, even though aching in unavoidable, suffering is indeed optional. Josiane, thank you for your reviews about my work and for being this sensible and sensitive person. You are an example of what a humanistic

scientist should be. Naiara, thank you for the productive driving lessons, for reviewing my work and for sharing countless meals with me. I will never forget you three.

I thank Érico for his assistance in obtaining the Transmission Electronic Microscopy images.

I also would like to devote my sincere thanks to Profa. Dra. Daniela Zanchet and all GCN members for the fruitful discussions and for the help in the PROX-CO catalytical measurements

I would like to pay special thanks to my friend Thalyta, for being my occasional lunchmate, running partner and German classes colleague. I would also like to thank my friends, Breno Saldanha, Tiago Ferreira and Fernanda Palmeira, my fellow chemical engineers who are *nordestinos* like me and participated in this journey during this master's degree. Thanks for all the couscous, tapioca, lunches and trips together, and for bringing to Campinas the unique light and sunshine only *nordestinos* have.

I also dedicate a thank you to all the people who took part of this time of my life that was to live in the neighbourhood of Barão Geraldo, either during the master's degree or during my undergraduate studies. Altogether, I have spent almost one fourth of my entire life here which was a period of significant personal growth of my early adulthood. There is a prolific list of names I would like to thank, and it would be impossible to cite all of you, but you know who you were to me. Many thanks for all the surprise birthdays, qualification and defence celebrations and barbecues.

And I could not forget to dedicate this work to my partner and boyfriend Arthur Gabriel, who was of unspeakable importance for development of this work. In addition to his scientific enthusiasm and dialectic materialism views which fuelled my eagerness to conclude this project, thank you for your patience, understanding and love. I will be eternally grateful for the help you provided me to arrive at this very point of my life.

This study was financed in part by the Conselho Nacional de Desenvolvimento Científico e Tecnológico (CNPQ) - Process Number 131182/2018-8.

This study was financed in part by the Coordenação de Aperfeiçoamento de Pessoal de Nível Superior - Brasil (CAPES) - Finance Code 001

I also thank **FAPESP** for the financial support through the grant #**2018/07853-2, São Paulo Research Foundation (FAPESP).** It is stressed that the opinions, hypotheses and

conclusions or recommendations expressed in this material are the responsibility of the author and do not necessarily reflect the views of FAPESP.

.

RESUMO

Este trabalho traz uma nova classe de catalisadores para a reação de oxidação preferencial de monóxido de carbono (PROX-CO) baseados em nanobastões de céria decorados com nanopartículas de ouro na superfície. Uma síntese hidrotérmica com diversas vantagens tais como *one-step*, *one-pot* e fácil de purificar possibilitou a preparação de nanopartículas de céria com alto grau de pureza, além de tamanho e morfologia controlados. Um inédito processo de lixiviação baseado na exposição das nanopartículas a uma solução de ácido sulfúrico foi empregado, no qual os poros nativos dos nanobastões foram expandidos, melhorando a capacidade total de armazenamento de oxigênio (OSC) do material. Os resultados da espectroscopia de emissão óptica de plasma acoplada indutivamente (ICP-OES) revelaram que as condições de lixiviação ácida empregadas foram eficazes para expandir a estrutura dos poros sem comprometer a estrutura das facetas cristalinas dos nanobastões de céria e evitar sua dissolução. Além disso, os resultados de espectroscopia Raman confirmaram o aumento da concentração de vacâncias de oxigênio na amostra lixiviada. Os nanobastões também foram dopados com íons Zr (IV) por meio de uma por co-precipitação. Para completar o catalisador, nanopartículas de ouro foram depositadas na superfície do óxido por deposição-precipitação (DP), na qual $HAuCl_4$, é depositado na superfície do óxido após um ajuste controlado do pH da solução para 3, precipitando $Au(OH)_3$, e posteriormente ouro metálico depois de tratamento térmico tratamento com a superfície do suporte desempenhando um papel como agente de nucleação. Diferentes métodos para aumentar o pH da solução, como adição de NaOH e decomposição térmica da ureia e diferentes temperaturas de tratamento térmico foram empregados, o que levou a diferentes desempenhos catalíticos. Demonstrou-se que os catalisadores compostos pelos nanobastões lixiviados são catalisadores mais apropriados para a reação de PROX-CO, aumentando a conversão total de CO e diminuindo a temperatura de conversão máxima, o que é favorável para o uso potencial deste material como catalisador em células combustíveis. Os nanobastões dopados com Zr também foram determinados como suportes mais eficientes, o que foi atribuído à capacidade dos íons Zr(IV) de elevar a OSC do material.

ABSTRACT

This work brings a novel class of catalysts for the reaction of preferential oxidation of carbon monoxide (PROX-CO) based on ceria nanorods decorated with gold nanoparticles on the surface. A hydrothermal synthesis with several advantages such as a one-step, one-pot, low-cost and easy-to-purify process that enables the preparation of high purity ceria nanoparticles of controlled size and morphology. Afterward, a novel acid lixiviation process based on treating the nanoparticles with sulfuric acid solution was employed in which the native pores of ceria nanorods were expanded improving the total oxygen storage capacity (OSC) of the material, a physical-chemical property of utmost importance to understand chemisorption phenomena in catalysis. Inductively coupled plasma optical emission spectroscopy (ICP-OES) results revealed that the acid leaching conditions employed were effective to expand the pore structure without compromising the facets structure of ceria nanorods and avoiding their dissolution. Raman results confirmed the increase in oxygen vacancies concentration in the lixiviated sample of nanorods. Cerium nanorods were also successfully doped with Zr (IV) ions via a co-precipitation technique. In order to complete the nanohierarchy of the catalyst, gold nanoparticles were placed down onto the oxide surface by the deposition-precipitation (DP) method. In the methodology carried out in this work, gold precursor, $HAuCl_4$, is brought out of the solution in the presence of a suspension onto the support by increasing the pH in order to precipitate $Au(OH)_3$, which gives out metallic gold after thermal treatment. The surface of the support plays a role as a nucleating agent controlling. Different methods to increase the pH of the solution, such as addition of NaOH and thermal decomposition of urea and different annealing temperatures were employed, which led to different catalytic performances. The catalysts composed by lixiviated ceria nanorods were proved to be better for PROX-CO reaction as they increased the total CO conversion and decreased the maximum conversion temperature, which is appropriate for the potential use of this catalyst in fuel cells. The Zr-doped nanorods also were determined to be more effective which was attributed to the capacity of Zr (IV) to improve the oxygen vacancy concentration of the nanorods.

RÉSUMÉ

Ce travail-ci apporte une nouvelle classe de catalyseurs pour la réaction d'oxydation préférentielle du monoxyde de carbone (PROX-CO) à base de nanotiges de ceria décorées de nanoparticules d'or à la surface. Une synthèse hydrothermale avec plusieurs avantages en tant qu'il s'agit d'un procédé en une étape, à faible coût et facile à purifier, ce qui permet la préparation de nanoparticules de ceria de haute pureté avec taille et morphologie contrôlées. Par la suite, un nouveau procédé de lixiviation acide basé sur le traitement des nanoparticules avec une solution d'acide sulfurique a été utilisé, dans lequel les pores natifs des nanotiges de ceria ont été élargis améliorant la capacité totale de stockage d'oxygène (OSC) du matériau. Les résultats de spectroscopie d'émission optique à plasma à couplage inductif (ICP-OES) ont révélé que les conditions de lixiviation acide utilisées étaient efficaces pour accroître la structure poreuse sans compromettre la structure des facettes des nanotiges de céria, en échappant leur dissolution. Les résultats de la spectrométrie photoélectronique X et Raman ont confirmé l'augmentation de la concentration des lacunes d'oxygène dans l'échantillon lixivié de nanotiges. Les nanotiges de cérium ont également été dopées avec succès avec des ions Zr (IV) via coprécipitation. Afin de compléter la nanohiérachie du catalyseur, des nanoparticules d'or ont été déposées sur la surface de l'oxyde par la méthode de dépôt-précipitation (DP). Le précurseur d'or, $HAuCl_4$, est precipité de la solution sur le support en augmentant le pH afin de précipiter $Au(OH)_3$, qui se transforme em or métallique après traitement thermique. Différentes méthodes pour augmenter le pH de la solution, telles que l'addition de NaOH et la décomposition thermique de l'urée et différentes températures de traitement thermique ont été utilisées, ce qui a conduit à différentes performances catalytiques. Les catalyseurs composés par les nanotiges de ceria lixiviées se sont avérées être meilleur pour la réaction de PROX-CO, une fois qui ils ont augmenté la conversion totale de CO et diminué la température de conversion maximale, ce qui rend ce máteriau approprié pour l'utilisation potentielle dans des piles à combustible. Les nanotiges dopés au Zr ont également été jugés plus efficaces, ce qui a été attribué à la capacité du Zr (IV) à améliorer la concentration de lacunes d'oxygène dans les nanotiges.

LIST OF FIGURES

LIST OF TABLES

LIST OF ABBREVIATIONS AND ACRONYMS

- BET ..... Brunauer-Emmet-Teller
- BJH ..... Barret-Joyner-Halenda
- DP ..... Deposition-precipitation
- EDS ..... Energy-Dispersive X ray Spectroscopy
- FC ..... Fuel Cell
- FTIR ..... Fourier-Transform Infrared Spectroscopy
- HRTEM ..... High-Resolution Transmission Electron Microscopy
- IEP ..... Isoelectric point
- ICP-OES ..... Inductively Coupled Plasma Optical Emission Spectroscopy
- JCDPS ..... Joint Committee on Powder Diffraction Standards
- L-H ..... Langmuir-Hinshelwood
- LNRCeO_2 ..... Lixiviated Ceria Nanorods
- LTS ..... Low temperature Water Gas Shift Reaction
- MkV ..... Mars Van-Krevelen
- NP ..... Nanoparticle
- NRCeO_2 ..... Ceria Nanorods
- OSC ..... Oxygen Storage Capacity
- PEM, PEMFC ..... Proton Exchange Membrane Fuel Cell
- PGM ..... Platinum Group Metals
- POM ..... Polyoxometalate
- POX ..... Partial oxidation of Carbon Monoxide
- PROX-CO ..... Preferential Oxidation of Carbon Monoxide
- R-WGS ..... Reverse Water Gas Shift Reaction
- SRM ..... Steam Reforming Process of Methane
- TCD ..... Thermal Conductivity Detector
- TPR ..... Thermal Programmed Reduction
- UV-Vis ..... Ultraviolet-Visible Radiation
- WGSR, WGS…… Water Gas Shift Reaction
- XRD ..... X ray Diffraction

LIST OF SYMBOLS

- F_{2g} – Irreducible representation of the 1st order CeO_2 Raman spectrum active mode found close to 464 cm^{-1}.
- d – Interplanar distance
- θ – Bragg angle
- R – Reflectance
- h – Planck's constant
- λ – Radiation wavelength
- a – Lattice constant
- (hkl) – Miller index
- I_D/I_{F2g} – Intensity ratio between the defect band of ceria and the F_{2g} band
- $V_o^{\cdot\cdot}$ – Oxygen vacancy in ceria
- E_g – Band gap energy
- eV – electron-volt
- T_{max} – Temperature of maximal conversion of CO into CO_2

SUMMARY

1. INTRODUCTION

1.1 – Hydrogen, a multitask chemical

Hydrogen is the most abundant chemical element in the Universe and modern human society relies heavily on its applications. [1] [2] This element, which in its elemental form is found as a diatomic molecule, H_2, is a fundamental building block to produce ammonia, and therefore fertilizers, and methanol, a precursor to make acetic acid and formaldehyde, which in turn are used in products like adhesives, foams, construction materials, solvents and windshield washer fluids. [3]

Hydrogen is also widely used for the processing of intermediate oil products, such as in hydrodesulfuring and cracking processes. Thus, about 55 % of the hydrogen produced around the world is used for ammonia synthesis, 25 % in refineries and about 10 % for methanol production. The other applications worldwide account for only about 10 % of global hydrogen production. [4]

Although hydrogen finds itself a plenitude of applications, its production faces one major problem in a sustainable designed society, as there is no economically viable natural source of hydrogen in Earth.

The most common method for obtaining H_2 is steam reforming process of methane (SRM), in which hydrocarbons react with water vapor producing a non-equimolar gas mixture of H_2 and CO, according to Equation 1. [5]

$$CH_{4(g)} + H_2O_{(g)} \rightarrow 3H_{2(g)} + CO_{(g)} \qquad \Delta H = +206.3\ kJ\ mol^{-1} \qquad (1)$$

The H_2/CO mixture, which is obtained in steam reforming and other industrial processes for H_2 production is called water gas. However, for certain industrial uses, as in the synthesis of ammonia or its use in many types of fuel cells, it is necessary to obtain H_2 with extremely high degree of purity, that is, with lower CO contents, since this gas also poisons industrial catalysts involved in the synthesis of ammonia or in fuel cells (FC's) catalysts. Therefore, in order to maximize H_2 content, a post-steam reforming step was introduced, in which most of the remaining CO is converted into CO_2 in a process called the "water gas shift reaction" (WGSR). In this reaction, carbon monoxide reacts with a water vapor flow, producing CO_2 and

hydrogen gas, according to Equation 2. Then, CO_2 is removed through an alkaline treatment or via zeolite capture. [6]

$$CO_{(g)} + H_2O_{(g)} \leftrightarrows CO_{2(g)} + H_{2(g)} \qquad \Delta H = -41.6\ kJ\ mol^{-1} \qquad (2)$$

Afterwards, hydrogen gas purified by the WGSR still has a CO content above the operational threshold for its application in fuel cells, in which values below 50 ppm are more suitable. This limitation stems from the fact that platinum (material which is one of the main constituents of the cell electrode) strongly adsorbs CO at low temperatures, with severe loss of its catalytic activity. [5] Thus, to reduce CO content to even lower values (< 10 ppm), a reactional step called **preferential oxidation of carbon monoxide** (PROX-CO) is used, as indicated in Equation 3.

$$2CO_{(g)} + O_{2(g)} \rightarrow 2CO_{2(g)} \quad mol^{-1} \qquad \Delta H = -565.9\ kJ\ mol^{-1} \qquad (3)$$

Hydrogen used as a fuel has the potential to be a powerful effective accelerator towards a low-carbon energy system, adequate of addressing multiple energy challenges at a time: from facilitating the massive integration of renewables and decarbonisation of energy production, to energy transportation in a zero carbon energy economy, to electrification of end uses. [5]

The main goal of this project is to develop a new effective catalyst for PROX-CO reaction based on gold nanoparticles deposited over cerium (IV) oxide nanoparticles and study its chemical, optical, surface and textural properties.

This dissertation is inserted into a larger context of the research lines conducted at the Laboratory of Functional Materials of the Institute of Chemistry at UNICAMP, in which it can be highlighted efficient techniques to deposit metallic nanoparticles (NP's) over oxide surfaces and studies about non-stoichiometric compounds, such as cerium (IV) oxide NP's with Raman spectroscopy, the porous characteristics of its nanorods and its potential applications as a catalyst for WGS and PROX-CO reactions. These published studies served as reference for this dissertation. [7-8]

1.2 - Recent Advances in Design of H_2 Purification Methods

The increasing demands for high-purity hydrogen to be used in fuel cell systems triggered a renewed interest in the water-gas shift reaction. This notable industrial process provides an attractive approach for hydrogen generation and additional increase of its concentration in the gas mixtures obtained by processes utilizing coal, petroleum, or biomass resources, as seen in Figure 1. An effective step for further elimination of CO traces from the reformate stream after water–gas shift unit is the preferential CO oxidation.

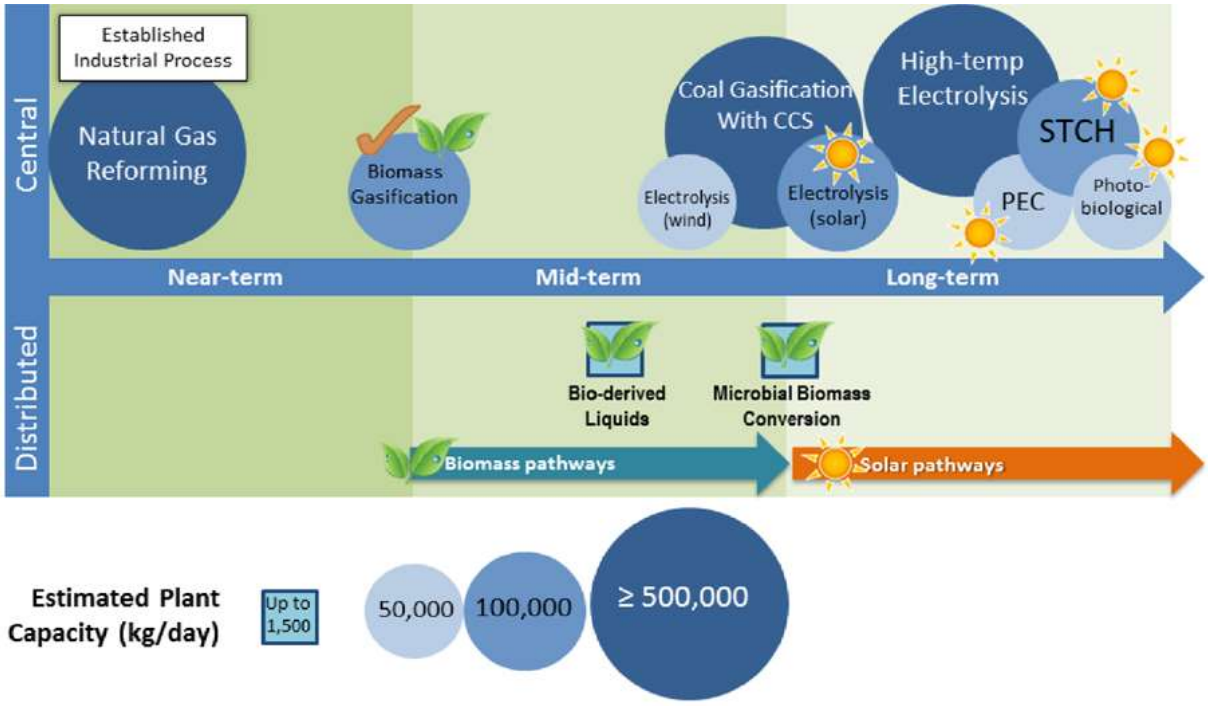

Figure 1. Hydrogen production techniques distributed according to their forecast of being widespread as an economically viable process (near-term, mid-term or long term). Currently, natural gas reforming accounts for more 95% of worldwide production of hydrogen. Image adapted from [9].

Ivanova et al. have described CO clean-up fundamentals in detail highlighting on the current practice in industrial hydrogen production and highlighting the requirements that should be met by processes and catalysts for small-scale applications such as residential fuel cells or on-board hydrogen generators. [9] Because of safety and technical constraints, it was shown that well established commercial Cu/ZnO-based and Fe_2O_3-Cr_2O_3-based catalysts currently used for

large-scale hydrogen production are not suitable for fuel cells. Besides the fact that these catalysts require special activation procedures before usage; they are highly pyrophoric, intolerant to poisons, susceptible to oxidation and condensation. Additionally, some technical issues like small catalyst volume and low weight, reduced start-up time, stability under steady state and transient conditions impose new goals and challenges for design of WGS and PROX-CO catalysts. Developing well-performing, stable, and selective catalysts for WGS and PROX reactions is of primary importance for efficient upgrading of hydrogen purity for fuel cell applications.

CO_2 release into the atmosphere due to fossil fuel burning machines accounts for over 50 % of the enhancement of the greenhouse effect, one of the main causes attributed to the global warming. This has culminated in an ever-increasing demand of efficacious clean-up technologies and search for alternative fuels, their utilization being accompanied by toxic free emissions. Bringing about a zero-waste emission by using clean energy sources and cutting down greenhouse gas emissions would positively affect social and economic development and would contribute greatly into improving current environmental conditions. [10]

Due to the increasing amounts of CO_2 into the atmosphere, hydrogen emerge with many advantages as an energy carrier, specially the fact that its combustion generates only water. Excluded the nuclear fuels, it has the highest energy content per unit mass among all fuels, which is almost three times higher than that of gasoline. [11] Moreover, hydrogen can deliver economically feasible, financially attractive, and socially beneficial solutions of the growing concerns about global warming and increasing world energy demand and to produce it, several methods have already been reported and discussed in the following sections.

This section focuses on providing a bibliographical review of several approaches to synthesize hydrogen described in the literature.

1.2.1 - Fossil fuel based methods

Fossil-based hydrogen production methods are among the most full-fledged technologies available nowadays, as they present higher efficiency and lower production cost ranges than the other methods available. Natural gas is mostly

composed of methane, but it commonly includes varying amounts of other higher alkanes, and sometimes lower fractions of other gases, such as carbon dioxide, nitrogen, hydrogen sulfide, or helium.

Most of the hydrogen produced in a worldwide scale comes from the *steam reforming process* of methane (SRM) derived from natural gas sources with an efficiency range of 65-75%. Higher alkanes can also be reformed to produce it although with lower efficiency and yields. [13]

The SRM reaction is part of the **C1 Chemistry**, which refers to the study of one-carbon molecules reactions. This Chemistry subdivision includes molecules, such as CO, CO_2, CH_4, CH_2O, CH_3OH and HCOOH, and plays a pivotal role in the current supply of energy and chemicals. These C1 molecules, which either are naturally found or can be easily produced from natural carbon resources, are abundant and cheap carbon feedstocks. C1 chemistry will most likely become even more critical because of the worldwide increasing need for the production of liquid fuels and building-block chemicals from alternative carbon resources such as the emerging shale gas in the United States or coal in China to replace crude oil. [14]

The industrial methane steam reforming process usually makes use of a heated tubular furnace and downstream cleaning units. In a simplified process for SRM, the feed is at first hydrodesulfurized and subsequently mixed with superheated steam in a heated furnace, which is named reformer. The reformer contains a series of catalytic reforming tubes in a row packed with a nickel-containing catalysts bed and is commercially operated with a temperature gradient, with the difference of 450-650 °C for inlet and 800-950 °C for outlet. Latest steam reformers units can attain capacities up to 300,000 m^3 of H_2 h^{-1} with average heat fluxes over 100,000 kcal m^{-2} h^{-1} (0.12 MW m^{-2} h^{-1}). [15]

Another procedure to produce hydrogen from natural gas is via the reaction of *partial oxidation (POX) of hydrocarbons*. This reaction takes place when a substoichiometric fuel-air mixture is partially combusted inside a reformer yielding a hydrogen-rich syngas which can further used. Although its efficiency is lower than the one observed for steam reforming, it can be performed under lower temperatures and it might be suitable to be employed for small-scale applications featuring fast catalytic conversion of hydrocarbons. Previous works established that nickel-based catalysts are very active towards partial oxidation reaction, nevertheless, many

potential alternatives have already been probed, including supported Co or Fe, supported noble metal, or transition metal carbide catalysts. [15]

Coal gasification is another alternative to produce hydrogen from a fossil fuel. In this process, coal is blown through with oxygen and steam currents while also being heated under substoichiometric conditions in order to avoid total oxidation to carbon dioxide. During the coal gasification reaction, the coal is heated in the gasifier under a well-controlled oxygen and steam environment. Oxygen and water molecules partially oxidize the coal without resulting in combustion and the primary products are the desired gaseous mixture with by-products like phenols and tar. The procedure was developed as an alternative to hydrogen production in countries that, despite not having large reserves of natural gas, had huge stocks of natural coal deposits, such as the United Kingdom and Germany. [15]

And yet, a fourth alternative is called *drying reforming of methane* (DRM) which was first studied by the German chemists Franz Fischer (1877-1947) and Hans Tropsch (1889-1935) in the Max Planck Institute for Coal Research. As the name suggests, this reaction consists of the combination of CH_4 with CO_2 in anhydrous conditions yielding synthesis gas (CO and H_2) at 700-900°C in a process that operates at a 20% lower cost with respect to other reforming processes. [16]

Even though with the cost advantages, several side reactions that might take place in the reactor, like reverse water-gas shift (RWGS) reaction, methane cracking, CO reduction and Boudouard reaction, which is the disproportionation of CO into CO_2 and elemental carbon, hinder the expansion of the DRM into larger scales. [16]

The most studied metal catalysts for DRM are the highly active and relatively cheap nickel based ones, yet they are vulnerable to coke formation. Therefore, recent research has been oriented into developing catalysts based on noble metals, including Pt, Ru, Rh, Pd, and Ir, which present lower carbon solubility potential and longer times before deactivation. [17]

1.2.2 - Biomass based methods

Hydrogen can also be produced from biomass via pyrolysis/gasification, making use of processes quite like the ones used for coal gasification. Thermal methods are convenient for hydrogen production from biocrude (also known as bio-

oil) and biogas, derivatives of biomass. In developing countries, such as China, India and Brazil, biogas is an attractive energy alternative for regions relying heavily on traditional biomass for their energy needs. [18]

Biomass gasification is a multiple-step process. The first one consists of pyrolyzing the material in an oxygen-lean condition below 600°C to produce a gas mixture of H_2, CO, CO_2, and other hydrocarbon compounds. In the second stage, tars are catalytically reformed to acquire a clean syngas. The syngas is purified to obtain the hydrogen product by conversion of CO into CO_2 via water gas shift reaction and subsequent absorption of CO_2. [19]

Organic matter degradation processes based on photochemical or photoelectrochemical chemical reactions are under development aiming to produce electricity and hydrogen from organic waste materials. [20-21]

1.2.3 - Water based methods

Water has been regarded for a long time as one of the main potential sources for producing hydrogen as it is a cheap and readily available resource. Several methods of hydrogen production from water are available including electrolysis, direct thermal decomposition or thermolysis, thermochemical processes, radiolysis and photolysis.

Electrolysis consists of using electricity to split water molecules atoms into hydrogen and oxygen gases. Whilst steam reforming of natural gas has a thermal efficiency between 70-85%, water electrolysis is 70-80% efficient, with the forecast that its efficiency will reach 82-86% before 2030, if the progress in the research in this area continues at the current pace. [22] The main advantages of using electrolysis are, first, its operational temperature: while steam methane reforming requires temperatures between 700-1100 °C, water electrolysis systems can operate between 50-80 °C. Secondly, the fact that hydrogen produced by electrolysis can be produced on-site, meaning that the costly process of delivery via truck or pipeline is avoided. [23]

Based on life cycle analysis (LCA) studies, it has been shown that electrolysis processes powered by electricity from renewable energy sources have low global warming potential (GWP), less than 5 kg CO_2 eq/kgH_2, wind electrolysis having the

lowest. Whereas for electrolysis using electricity from the current grid, GWP can be as high as 30 kg CO_2 eq/kg H_2. [24]

Water molecules spontaneously dissociate at temperatures above 2000 K (the extent of single-step water dissociation varies directly with temperature from 1% at 2000 K to 34% at 3000 K) in a reaction called *thermolysis*. However, temperatures to perform water thermolysis are too high to be accomplished in usual process piping and equipment and for this reason, catalysts are required to reduce the dissociation temperature. The reaction is also sensitive to pressure variations being favoured if the pressure of the system is lowered.

Hydrogen can be produced at relatively lower temperatures, through *thermochemical cycles*, in which water dissociation into hydrogen and oxygen is achieved through two or more successive reaction steps involving redox materials such as sulphur and some metal oxides. Approximately 2000-3000 thermochemical cycles have been studied, each with different sets of operating conditions, engineering challenges, and hydrogen production opportunities, and only 20-30 of which, with efficiencies up to 40-50% reported in the literature, may be technically feasible for large-scale hydrogen production. Critical issues of these processes are the separation of the hydrogen produced and the corrosion problems associated with the chemicals involved in the cycles.

One promising thermochemical cycle that operates at lower temperatures than most thermochemical cycles is the Cu-Cl thermochemical cycle, which splits water into hydrogen and oxygen through intermediate copper and chlorine compounds. Due to its low temperature requirements, this cycle can be integrated with various nuclear power plants, which generate enough heat in order to make the thermal decomposition reaction sustainable or even concentrated solar power CSP (systems which generate solar power by using mirrors or lenses to concentrate a large area of sunlight onto a small area and can achieve the necessary temperature to promote the thermochemical cycle).

Nuclear radiation can also break water bonds through *radiolysis*. In 2005, in the Mponeng gold mine, South Africa, the deepest mine in the world, it has been discovered a new phylotype of *Desulfotomaculum* bacteria which was able to obtain its primary energy feeding on radiolytically produced hydrogen, due to exposition to radioactive decay of radioisotopes of uranium, thorium and potassium. Since this

discovery has been accomplished, spent nuclear fuel is also being looked at as a potential source of hydrogen. [25]

Hydrogen can also be released from water via *light-driven procedures* involving photobiological, photochemical and photoelectrochemical systems, although they are at early stages of development and have considerably low efficiency levels at the present days. Undergoing research is still on the way to come up with methods to produce hydrogen for longer periods of time and increase the rate of hydrogen production.

Certain algae and cyanobacteria photoproduce hydrogen by *photobiological processes* for short times to get rid of excess energy before starting up the photosynthetic carbon fixation process. Algal photosynthesis and hydrogen production are correlate processes, as both start with the same solar-energy-activated splitting of water to oxygen, electrons, and protons. Then protons and electrons go to a second enzymatic reaction. In one case, carbon dioxide is reduced to produce sugars, which might be used subsequently to provide energy for the algae. In the other case, a chemical reaction reduces H^+ ions to produce H_2. An alternative approach to sustaining algal hydrogen production artificially is to partially inactivate the normal photosynthetic process, promoting instead the hydrogen production. [26]

Moreover, it is also possible to decompose water by *photochemical processes*. Pure water only absorbs few IR frequencies of the solar spectrum light that reaches out Earth's surface, and such IR radiation is not enough to dissociate water molecules. Therefore, a *photocatalyst* is necessary in order to achieve water splitting by solar radiation, i.e., a species that absorbs higher energy photons and prompts the redox elementary steps required to break H_2O into H_2 and O_2. Positive and negative charges must, then, reach the surface of the particles without recombining each other and promote the oxidation of oxygen and the reduction of hydrogen, respectively. Hydrogen reduction is thermodynamically viable if the electric potential associated with electrons in the conduction band is more negative than the redox potential of H^+/H_2, whereas holes in the valence band oxidize the oxygen atom of water if their potential is more positive than that of the pair O_2/H_2O.

Among the many possible photocatalysts, heterogeneous metal oxides are particularly appealing due to their resistance to photo-corrosion and long-term

stability. Metal oxides are often semiconductors that absorb solar photons with energy equal to or higher than their band gaps.

It is also possible to produce hydrogen by *photoelectrochemical processes,* commonly referred as PEC water-splitting. This method consists of two semiconductor photocatalysts, separated by an electric circuit with a suitable electrolyte, which, upon photo-irradiation with enough energy, absorb the energy from the photons and generate charge separation at the valence and conduction bands and a photocurrent. This creates holes in the valence band, triggering the water oxidation at the surface of the photoanode, while photo-excited electrons in the conduction band facilitate the reduction of the H^+ to H_2 at the surface of the photocathode.[27]

1.2.4 - Other inorganic compounds

Hydrogen production can also be accomplished through pyrolysis and hydrolysis of metal hydrides. Lithium hydride (LiH), magnesium hydride (MgH_2), lithium borohydride ($LiBH_4$), sodium borohydride ($NaBH_4$), lithium aluminium hydride ($LiAlH_4$) and sodium aluminium hydride ($NaBH_4$,) are frequently employed compounds chosen in this category. These compounds are often chosen as a more efficient way to storage hydrogen in an indirect way, once gaseous hydrogen has low energy density and presents serious dangers associated with flammability issues. [28]

It is also possible to obtain hydrogen from hydrogen sulphide in twofold goal processes that combines hydrogen recovery with the abatement of a highly toxic pollutant gas, as H_2S represents a serious risk factor in acute and chronic poisoning for workers. Thermal dissociation, catalytic cracking, multistep thermochemical methods photocatalytic splitting and plasmochemical methods at different stages of maturity are still under research for further improvement in converting H_2S into H_2. [29]

1.3 - Application of fuel cells

Presently, the emerging hydrogen economy demonstrates a very high potential of fuel cells to replace the internal combustion engine in vehicles and to supply power in stationary and portable devices due to their high-energy efficiency,

cleanness, and fuel flexibility. Together, hydrogen and fuel cells represent a radically different approach to energy conversion.

As reported in the previous session, despite the numerous methods under development for hydrogen production, SRM is still the main source of hydrogen gas production. Due to the operational limitations of purification, the hydrogen gas obtained by this method has CO contamination in different proportions.

The hydrogen-rich gas stream CO content in volume after WGS reaction ranges close to 0.5-1 % because of thermodynamic limitation of this reversible and moderately exothermic reaction. Due to the high sensitivity of platinum anode electrode in polymer electrolyte membrane fuel cells (PEMFC's) towards very low CO levels, the CO concentration must be lowered to levels below 10 ppm (below 100 ppm for improved tolerance alloy anodes). An effective step for elimination of CO traces from the hydrogen-rich reformate gas stream after WGS unit is the PROX reaction.

The development of new portable electronic devices is involved in the growing interest in FC technology to replace or supplement batteries in portable applications. FC's generate electrical power in an environmentally clean and secure way with very high energy densities (four to six times larger when compared to Li-ion batteries - fuel cells have been shown to provide 530Wh/kg compared to 44 Wh/kg for lithium ion batteries). However, while the weight of fuel cell systems offers a distinct advantage the current costs are not in their favour. While a Li-ion battery system will generally cost around 1.20 USD/Wh, fuel cell systems cost around 5 USD/Wh, putting them still at a significant disadvantage. [30]

However they have limited power capacity and cannot respond to the sudden changes in the load that may occur in some applications. The design of hybrid FC-battery systems as well as the development of strategy for management of the energy may mitigate among others the problem of oversizing of the FC associated with the changes in the load. For these hybrid systems, PEMFC's have been considered to enhance the energy density of batteries. However, some challenges remain relevant, such as H_2 storage and water and thermal management, and are still unresolved for PEMFC's. [31]

In a PEMFC, the fuel, which is purified hydrogen and the oxidant (air or oxygen) are supplied to the FC passing through a series of plates, which have the purpose to diffuse them in the most uniform way to the two membrane sides. A

PEMFC transforms the chemical energy liberated during the electrochemical reaction of hydrogen and oxygen to electrical or thermal energy, as indicated in Figure 2. A stream of hydrogen is delivered to the anode side of the FC and at the anode side, it is catalytically split into protons and electrons, conducting the oxidation reaction. These protons permeate through the polymer electrolyte membrane to the cathode side. The electrons travel along an external load circuit to the cathode side of the FC, thus creating the current output. In the meantime, a flow of oxygen is delivered to the cathode side, where oxygen molecules are reduced and, subsequently, react with the protons permeating through the membrane to form water molecules and to liberate heat.

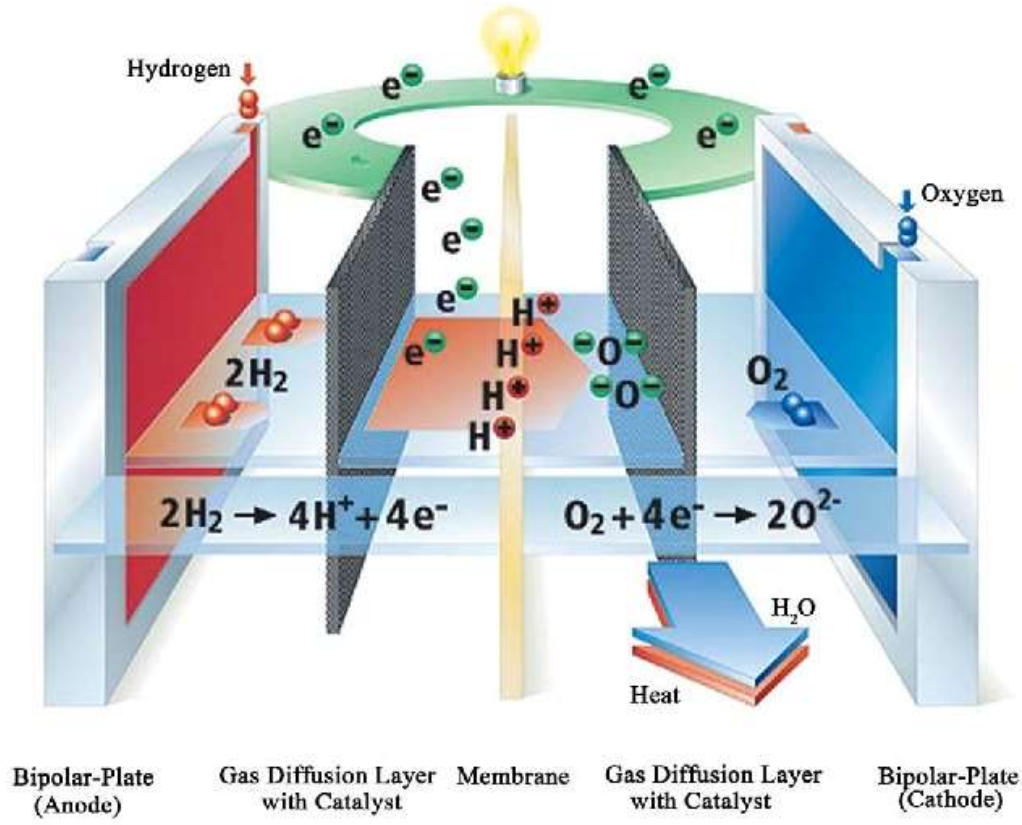

Figure 2. Polymer electrolyte membrane fuel cell diagram showing the H_2 oxidation at the anode and the O_2 reduction at the cathode. Image adapted from [31].

So, as previously stated, most of the hydrogen produced worldwide comes from the SRM reaction, including the one used as fuel in FC's and for this reason, PROX-CO is an important reaction for purification so that hydrogen reaches the required levels of purity. For PROX-CO reaction, whatever the catalyst employed,

the operating temperature optimal range for the maximal CO oxidation is quite narrow. Over this temperature range, the CO conversion decreases as the temperature increases because of oxygen consumption in the reaction of hydrogen oxidation. Moreover, the heat released in these two oxidation reactions favours the slightly endothermic reverse water-gas shift reaction (RWGS).

Under the current perspectives of an upcoming hydrogen economy, fuel cells demonstrate a very high potential to replace, at least partially, internal combustion engines in vehicles and to supply power in stationary and portable devices due to their high-energy efficiency, cleanness, and fuel flexibility, and for this reason, the development of PROX-CO catalysts for this purpose is of utmost importance.

1.4 - Development of PROX-CO catalysts

Taking in account several published works, it is undeniable that searching for novel appropriate supports is of utmost importance to prepare well-performing catalysts for the WGS and PROX-CO reactions. [32-33]

The first patent for the PROX catalyst was awarded to Engelhard in the 1960's, in which supported Pt catalysts were applied to purify the hydrogen for the application of ammonia synthesis. Later, various catalysts were developed, with the aim of selectively removing CO while minimizing H_2 consumption in a wide operation temperature window (e.g., 80-180 °C) for application on PEMFC's. [34]

Usually PROX-CO catalyst are composed of the active metal NP's and the support in which they are anchored to. According to the active metal used, the catalysts can be classified either into **group VIII metal catalysts** (mainly platinum group metal catalysts, denoted as PGM catalysts) or into **group IB metal catalysts** (Cu, Ag, and Au-based catalysts).[35]

On the other hand, the support materials do have a great influence on the catalytic performance of the metals and can be classified into "non-reducible" and "reducible" supports categories, as it will be discussed in the next few sections. When the surface is non-reducible, the metallic NP's are said to be unpromoted, as the atoms from the surface do not produce a synergic effect which might result into an improvement of PROX-CO performance. When the surface is reducible, there is a

synergistic effect that arises from the interaction between the surface atoms and the metallic particles. These class of catalysts materials are summarized in Figure 3.

The support may take part directly in the reaction or govern catalytic performance by affecting shape and gold particle size, gold-support interface interaction, and stabilization of electronic-structural properties of gold. Shekhar et al accomplished kinetic and *operando* FTIR measurements of the WGS reaction over gold nanoparticles of different average size supported on model Al_2O_3 and TiO_2 and sustained further evidence for a direct role of the support in water activation, while adsorption of CO and formation of CO_2 and H_2 took place over gold NP`s. [36]

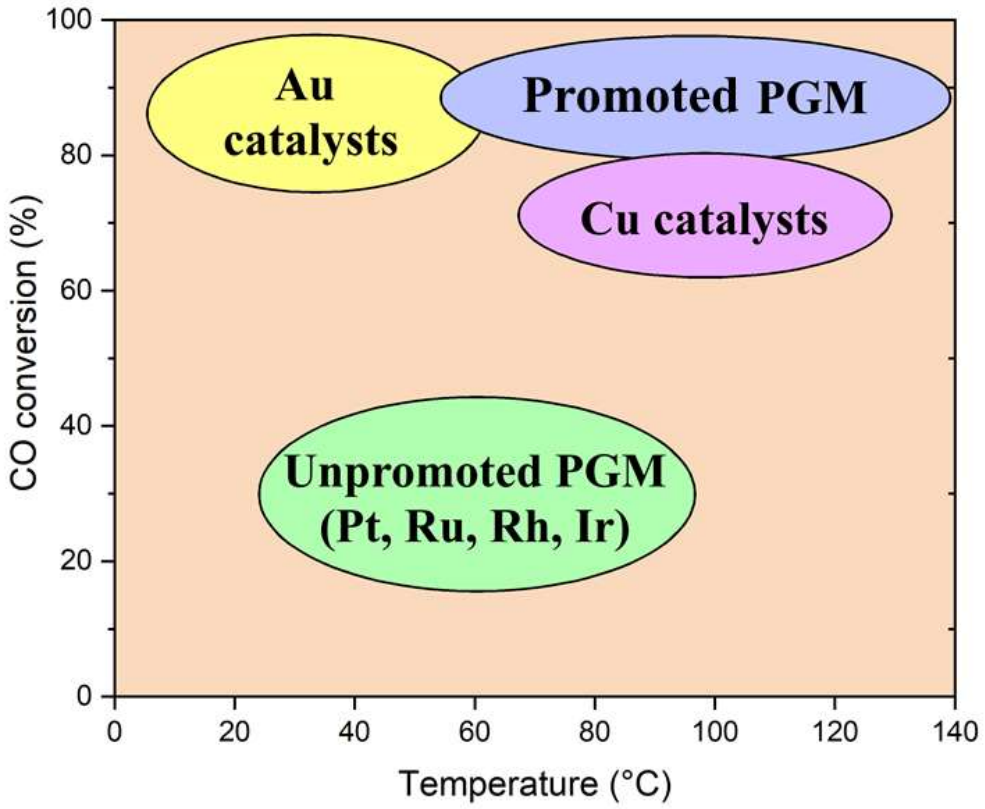

Figure 3. Conceptual illustration of catalytic performances of different classes of catalysts for PROX-CO reaction. For clarity, only the maximum CO conversion and reaction temperature window are shown, while the selectivity is not shown here. Image adapted from [35].

Due to their high CO conversion at lower temperatures when compared to other classes of catalyst, resistance towards deactivation by water or CO, thermal stability preventing sintering at low temperatures, and absence of pyrophoricity, gold based catalysts were the one chosen to be studied in this work. [35] As previously

stated, isolated Au NP's are weakly effective to promote PROX-CO, but when supported on oxide supports, the systems if functional as a catalyst.

Gold on non-reducible supports, such as SiO_2, Al_2O_3, or MgO, exhibited lower activity in contrast to deposited gold on reducible materials, such as CeO_{2-x}, MnO_{1+x}, CuO_{1-x}, CoO_{1+x} or FeO_{1+x}, that exhibited a significantly enhanced CO oxidation. A similar support effect was observed in the case of gold-catalysed WGS reaction. Andreeva et al. were the first to measure and compare WGS activity of gold nanoparticles supported on Fe_2O_3 and Al_2O_3. Despite the similarity of gold particle size on both supports (3.5 nm), a very low activity of Au/Al_2O_3 was observed, indicating a decisive role of support nature. [37]

Sandoval et al. have studied Au/TiO_2, Au/CeO_2, Au/Al_2O_3, and Au/SiO_2 and found out a much higher WGS activity of gold nanoparticles on reducible supports (such as CeO_2) than on Al_2O_3 and SiO_2.[38] Lenite et al. evaluated gold supported on CeO_2 and $(\alpha\text{-}\gamma)/Al_2O_3$ prepared by the method of solution combustion synthesis and observed that the Al_2O_3-supported gold catalysts attained only about 30% CO conversion. [39] In this case, the authors pointed out an indirect role of the support allowing penetration of small gold particles (2-3 nm) into pores of 4 nm average size, thus negatively affecting access of CO and water. In a recently released review, Carter and Hutchings also underscored about the support effects in WGS gold catalysts using reducible and non-reducible materials. [40] Many gold-based catalysts for PROX-CO reaction reported in the literature are summarized in Table 1.

1.4.1 - Non-reducible support

Alumina as support

Alumina is one of the most commonly applied commercial supports in heterogeneous catalysis due to its high surface area, thermal endurance, and mechanical strength. Although alumina is a non-reducible oxide and Au/Al_2O_3 catalysts exhibit a poor CO oxidation activity, Quinet et al. have shown that, at low temperatures, small amounts of hydrogen in the reactant mixture are able to enhance CO oxidation rate, which paves the way for promising applications in PROX-CO. [41] The promotional effect of hydrogen was attributed to the formation of

very active peroxide species, –OOH on the surface of gold particles that can interact efficiently with CO to form CO_2.

Grisel and Nieuwenhuys have also examined the role of surface OH groups on the gold-catalysed PROX. [42] They performed one of the first studies to demonstrate Au/Al_2O_3 performance in PROX. Alumina modified by doping with MgO or MnO_{1+x}, or both metal oxides, altered activity and selectivity in CO oxidation to CO_2 positively. MgO-doped Al_2O_3 allowed the formation of smaller size Au particles, while MnO_{1+x} improved CO oxidation activity by oxygen activation. Modified alumina microspheres by the addiction of MnO_2 favoured CO oxidation over gold catalyst (size distribution from 2.5 to 7.5 nm).

Lakshmanan et al. have studied the effect of various promoters (La_2O_3, CeO_2, and MgO) on Au/Al_2O_3 performance for PROX. [43] In contrast to the aforementioned promotional role of MgO on gold dispersion and PROX activity, $Au/MgO/Al_2O_3$ was at least an active catalyst in this case, probably because of accelerated hydrogen oxidation below 100 °C [42]

The catalytic activity of the best-performing $Au/La_2O_3/Al_2O_3$ catalyst was tested after different reduction pre-treatments, implying that the abundance of negatively charged gold species is beneficial for CO oxidation. A detailed study has been carried out to clarify the reduction treatment effect on $Au/La_2O_3/Al_2O_3$ catalytic behaviour in PROX. Variation of the CO conversion was related to differences in average gold particle size and oxidation state of the gold species due to different reduction methods. [44]

The lanthanum-doped Al_2O_3 support was prepared by incipient wetness impregnation method of γ-Al_2O_3 with a $La(NO_3)_3$ solution followed by calcination at 850 °C for 4 h. The average size of the gold particles varied slightly based on the support (2.18 ± 1.6 nm for Au/ γ-Al_2O_3; 1.8 ± 0.4 nm for $Au/LaAlO_3$) [45] 100 % CO conversion was achieved at 30 °C, and the conversion remained stable in the temperature range 30-70 °C in the case of the Au/γ-Al2O_3 (80 % at 100 °C) catalyst [45]. In comparison, with the $Au/LaAl_2O_3$ catalyst, the CO conversion reached 100 % at 50 °C and remained stable in the temperature range 30-100 °C. However, long-term stability in the presence of CO_2 was not achieved with the latter catalyst [45] The specific rate of H_2 oxidation during CO-PROX decreased because of doping with lanthanum.

Table 1. List of Au-based PROX-CO catalyst summarized by Carter and Hutchings. Data extracted from [40].

Catalyst	D_{Au} (nm)	Feed composition (mol%; bal. He/N_2)					T_{max} (°C)	CO conversion at T_{max} (%)
		CO	O_2	H_2	CO_2	H_2O		
Au/Fe_2O_3	6.7	0.9	0.9	50	22	4.7	80	>99.5
Au/Fe_2O_3	15-25	1.03	1.37	65.4	24	3	80	99.8
Au/Al_2O_3	2.8 ± 1.6	1	1	40	20	10	30-60	100
$Au/La\text{-}Al_2O_3$	1.8 ± 0.4	1	1	40	20	10	50-70	100
Au/TiO_2	5	1	1	50	15	3	40-60	100
$Au/MgO/TiO_2$	2.7	1.3	1.3	65.3	-	-	50-80	100
$Au/FeO_x/TiO_2$	4	1.3	1.3	65.3	-	-	50-80	100
$Au/CuO/TiO_2$	2.5	1.3	1.3	65.3	-	-	50-100	100
$Au/MnO_x/MgO/\ Al_2O_3$	2.7 ± 1	2	1	4	-	-	50	95
Au/MnO_x	2.8	1	1	98	-	-	50	100
Au/FeO_x	3	1	2	40	2	2.6	50	100
Au/ZnO	4.9	1	1	40	-	-	50-70	100
$Au/Fe\text{-}SiO_2$	0.5-6	0.5	1	50	-	-	125	100
Au/Ti-SBA15	4	2.3	10	10	-	-	50	100
Au-Pt/Zeolite	51	1	1	40	10	10	190	99
Au-Cu/SBA15	3.0	1	1	78	18	-	23	100
Au/ZrO_2	5	1	1	60	-	-	45	100
Au-K/C	5	2	1.4	70	-	-	120	100
$Au/MnO_2/TiO_2$	2.5	1.3	1.3	65.3	-	-	80	98
$Au/MgO/Al_2O_3$	<5	1	1.6	60	-	-	90	80
$Au/CoO_x/TiO_2$	2.5	1.3	1.3	65.3	-	-	65	100
$Au/ZnO/TiO_2$	<5	1.3	1.3	65.3	-	-	70	100
Au/CuO	<5	1	2	10	-	2	100	100
Au/CuO/ZnO	5	1	1	40	-	-	80	100
Au/TiO_2-coated SiO_2	6	1	1	40	-	-	140	100
Nanoporous Au	3-10	1	1	50	10	10	80	100

The best performance was demonstrated by a catalyst of 4-nm average gold particle size that was not the smallest size. This finding revealed that decreasing the gold particle size is not the only reason to increase the rate of CO conversion, but also undesirable hydrogen oxidation could be affected, and a proper modification of alumina could solve the problem with selectivity.

Cerium-modified alumina supports for gold nano-particles were synthesized by mixing cerium acetate with aluminium isopropoxide using a typical sol–gel method. Analysis of the resulting catalyst revealed that ceria was either in the form of small crystallites or in a mixed structure with aluminium. The T_{max} value shifted to lower temperature because of modification of alumina with ceria, however, the CO_2 selectivity did not vary significantly at 80 °C. An Au/Ce-10Al catalyst was detrimentally affected by CO_2, whereas the Au/Al_2O_3 catalyst was resistant to CO_2 effects.

1.4.2 - Reducible supports

MnO_2 and Co_3O_4 as support

The Au/MnO_x (Au/Mn = 1/50) catalyst showed quite good performance with full conversion of CO at 50 °C in a feed stream containing 1 % CO and 1 % O_2 in H_2. Increasing the reaction temperature above 50 °C lowered the CO conversion from 100 % to lower values because of competition coming from the reaction of H_2 oxidation by O_2. The reversible transformation between the three forms that the ionic manganese oxides exhibit, MnO, Mn_3O_4, and Mn_2O_3, depends on the O_2 concentration and temperature, which may plausibly account for the stability of Au on Mn oxides in H_2 atmosphere. Au (3 nm)/MnO_2 exhibited full conversion at 25 °C. In another study, Au (14.6 nm)/MnO_2 was found to promote a 90 % CO conversion at 130 °C in H_2O-free and CO_2-free conditions but was struck with activity loss in the presence of CO_2. [46]

The Au (5 nm)/Co_3O_4 (32 nm) catalyst produced a maximum CO conversion of 75 % and CO_2 selectivity of 45 % at 100 °C. Inclusion of ceria into this system lowered the sintering degree of the cobalt oxide support. Transformation of Co_3O_4 into CoO and detrimental effects due to CO_2 during PROX-CO were reported. [47]

Transition metal carbides as supports

It has been reported that transition metal carbides, such as TiC, Mo_2C, WC, VC, etc., present similar properties quite like the platinum group metals, even though their application as a support in catalytical systems still find limitation when compared with metal oxides. Posada-Pérez and co-workers first reported that Pt, Au, Pd, and Ni supported on Mo_2C were about 4-8 times more active per superficial area than the commercial $Cu/ZnO/Al_2O_3$ catalyst at 120 °C.[48] for WGS and PROX-CO systems. Although the system presents the absence of oxygen vacancies as in non-reducible supports, the study of the system shed more light onto the mechanistical characteristics of the system and it was concluded that the active site for the system to be of the same type as that of conventional Au/CeO_2 catalysts, that is, the metal–support interface. Ma and co-workers recently discovered that the phase and structure of the Mo_2C was crucial to high catalytic activity. [49]

In a paper reported from Posada-Pérez and co-workers, β-MoC_x was used as the support, but when they used instead α-MoC, the activity of the supported Au catalyst was dramatically improved for WGS reaction.[48] The origin of the high catalytic activity was concluded to be the facile activation of water molecules, which was observed at temperatures as low as 303 K and attributed to the presence of “carbon vacancies”, making MoC_x a non-stoichiometric compound, such as MoO_3 and CeO_2.

Dong et al. showed that it was possible to synthesize Au/MoC_x after treatment of Au/MoO_3 under a flux of CH_4/H_2 at 700 °C and not only demonstrated that the Au/MoC_x catalyst could undergo reversible aggregation-redistribution cycles upon reversible calcination-carbonization conditions, but also revealed that Au/MoC_x exhibited high activity for the WGS at low temperature.[50] Despite the fact that it lost 20% of its original activity in the first 4 h on-stream at 180 °C in a feed containing 3% CO and 10% H_2O, it was shown that the catalyst could be totally regenerated in a 20% CH_4/H_2 flux at 600 °C, which hinders it for a full-fledged application in fuel cell systems due to the necessary temperature to recover it.

TiO_2 as support

Catalysts of gold supported over titania generally exhibit inferior performance in the CO-PROX reaction than those employing other oxides such as aluminium

oxide, iron oxide, and zinc oxide regarding CO conversion and CO_2 selectivity. Even though full CO conversion has been achieved with Au (5 nm)/TiO_2 catalysts, the selectivity toward CO_2 fell rapidly with temperature. [51]

Aiming to boost PROX-CO performance of catalysts gold supported on TiO_2, many strategies have been approached. The elementary technique involves modification of the titania surface with other metal oxides such as FeO, CuO, CeO_2, Co_3O_4, ZnO, MnO_2, and MgO.

Other possible chemical modifications that might be undertaken include supporting titania on silica or even SBA-15, a variety of mesoporous silicate with a hexagonal array of pores, before loading them with gold. Gold loaded supports generated by loading a vast range of gold amounts on amorphous FeO_x over TiO_2 by an incipient wet impregnation method were evaluated as catalysts for PROX-CO. A limited amount of iron oxide loading (1:9 mol ratio) resulted in full CO conversion at 80 °C (80 % CO conversion for Au/TiO_2) and a slight increase in CO_2 selectivity was also observed (from 40 to 48 %).[52] The complete CO conversion was attributed to the formation of smaller gold particles (2.5 nm) due to the presence of the FeO_x layer over TiO_2.

It has also been demonstrated that the CO conversion was dramatically improved with the use of copper oxide supported on titania as supports for gold catalysts.[53] In contrast with Au/TiO_2, the vast majority of the CuO_x-promoted catalysts exhibited stable and steady CO conversion values after reaching a maximum in the temperature range 50-100 °C. Particularly, the amount of oxygen consumed by H_2 decreased with increasing Cu content, accounting for the full CO conversion achieved over the Au (2.5 nm)/CuO_x-TiO_2 system. One of the systems, the Au/CuO_x-TiO_2 catalyst (4.8 - 95.2 mol ratio) gave rise to full CO conversion with a CO_2 selectivity of 68 % at 80 °C. The performance of the same system, Au/CuO_x–TiO_2 (4.8-95.2 mol ratio) catalyst was also found to be very stable during the stability test (without addition of H_2O and CO_2) and no gold sintering was noticed for the spent sample after the stability test. [54]

Deposition of amorphous ceria on the surface of titania by an incipient wetness impregnation technique (Au/CeO_2-TiO_2, 10:90 mol ratio) improved neither the CO conversion nor the CO_2 selectivity significantly. Further addition of 0.5 mol% CuO resulted in significant enhancement of both the CO conversion (80 → 100 %) and the CO_2 selectivity (40 → 55 %). While the addition of other promoters that were

effective as additives to other PROX-CO supports, such as oxides of Co and La were not effective, MgO-promoted Au/TiO_2 appeared to be beneficial for CO conversion. However, addition of the MgO promoter did not improve CO_2 selectivity. Rather than forming a thin layer on the surface of TiO_2, MgO was present on the TiO_2 surface in the form of thin isolated sparse islands without an explicit shape, which also occurred in the form of $Mg(OH)_2$.[55]

Instead of the traditional deposition-precipitation method commonly used to deposit Au NP's over the oxide surfaces, a photo-deposition method was employed and led to the production of relatively smaller gold particles that covered the surface of titania, even though for both techniques, the gold size distributions were in the range 1-5 nm. The increase in the number of smaller gold particles did not improve the catalytic performance significantly. Chen et al. altered the cobalt loading on the TiO_2 support and obtained the optimal results using Au/Co_3O_4/TiO_2 with a Co/Ti molar ratio of 5/95. Amorphous Co_3O_4 and ZnO supported on TiO_2 stabilized the small gold particles and suppressed H_2 oxidation, while the addition of MnO_2 on TiO_2 improved the CO_2 selectivity without jeopardizing CO conversion values.[56]

CeO_2 as support

The variation of the redox properties of ceria-based oxides with the size, composition, and morphology of the oxides has prompted the preparation of supported gold nanoparticles on pure ceria and various ceria-based mixed oxides.[57]

As a means of improving and controlling the catalytic properties of ceria, instead of utilizing the nanoparticles of pure ceria (A, Figure 4), cerium oxide has been dispersed on other oxide surfaces (such as TiO_2 and SiO_2) for use as a support for gold-based catalysts (B, Figure 4). Further improvements of such gold catalysts supported on dispersed ceria have also been demonstrated in the presence of promoters (D, Figure 4). Doping foreign cations into the ceria lattice has improved the redox properties of ceria because of the structural and electronic changes induced by the dopants (E, Figure 4). The various dopants include Mn, Fe, Co, Cu, Zn, Ti, and Zr. Alternatively, cerium oxide has been used after forming nano-composite oxides with other oxides such as cobalt oxide (C, Figure 4).

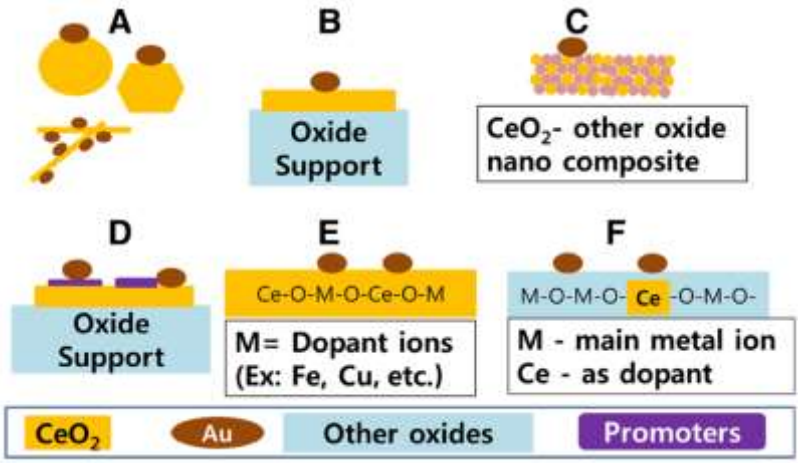

Figure 4. Various approaches for the synthesis of gold supported on ceria-based oxides. Image adapted from [58].

Doping ceria with small amounts of cobalt (II) oxide was shown to improve the PROX oxidation activity in the presence of CO_2 and H_2O in the gas stream of a series of catalysts based on $Au/CeO_2/Al_2O_3$. Alongside with the promotional effect of Co (II) ions, some important questions have been raised that allow clarifying the PROX reaction, in particular, the support and gold nanoparticle function in hydrogen oxidation, and existence of a support-dependent hydrogen effect on CO oxidation. It was suggested that hydrogen oxidation could be used as a criterion for selection of suitable catalytic formulations for H_2 clean-up reactions. [59]

Samarium oxide was also employed as a ceria promoter and compared with alumina as a dopant. It was reported that the nature of the created oxygen vacancies depends on the dopant: Al_2O_3 creates vacancies in the bulk ceria, while the SmO_x sample presented vacancies only located around SmO_x, and the ceria structure seems to be better ordered than the Al_2O_3 doped one. In addition, the concentration of Ce was higher when SmO_x was used as a promoter and the amount of formate species was also superior in a parallel way with the activity in the WGS reaction. They proposed a higher concentration of oxygen vacancies sites on the surface of the SmO_x doped catalyst, which facilitates the dissociation of water and enhances the activity.

An Au-mixed lanthanum/cerium oxide catalyst was proposed by Wang et al. as promising systems for the WGS reaction. The authors' attention was focused on the impact of La addition on the structure and reducibility of CeO_2 and on the reactivity of Au-based $LaCeO_2$ mixed oxides in the WGS reaction. Both structure and reducibility could be tailored by adjusting the LaO_x content and the reducibility of the

Au-free sample was improved by the addition of LaOx, with 25 % of atomic doping being the optimum loading to achieve the highest reducibility and therefore the best performance in the WGS reaction. [60]

The addition of Zr to Ce is one of the most effective modifications to Au/CeO_2 catalytical systems, but there are numerous other elements that have been employed to make a mixed metal oxide as a support for the WGS and PrOX-CO reaction. In this list are included Al, Fe, rare earth metals (La, Sm, Gd, Yb, Y, Ga), and Sn. Reina et al. reported the activity and stability of iron-promoted $Au/CeO_2/Al_2O_3$ for the WGS reaction at low temperature. Although comparisons with similar supported gold catalysts were not made, the catalyst longstanding stability was auspicious, despite the fact it lost *circa* 17% of its initial activity in the first 60 h of operation when exposed to a realistic reformate stream (9% CO, 11% CO_2, 30% H_2O, 50% H_2), it maintained the same value of conversion over the course of the next 80 h on-stream. It should be highlighted that the operation temperature was of 330 °C, which is much higher than typical temperatures reported for similar catalysts. [61]

Recently, there has been a bursting interest for a novel class of heterogeneous catalysts that emerged: atomically-dispersed supported metal catalysts. These have been reported to catalyse a few reactions, including CO oxidation and WGS reaction, and have received some focus, with highlight to their efficient use of precious metal, making use of smaller amounts of metal to achieve higher catalytical activities. Flytzani-Stephanopoulos and co-workers were the first to fully describe the activity of atomically-dispersed Au on several reducible oxide supports. In a recent published overview, Flytzani-Stephanopoulos summarised the evidence for the active site of Au catalysts being atomically-dispersed Au clusters in the LTS reaction. By employing the method of gold cyanidation, in which the element in its metallic form is converted to a water-soluble coordination complex, $Au(CN)_2^-$, the removal of metallic Au nanoparticles was achieved (over 90% of gold loading was removed), leaving only cationic, atomically-dispersed Au on the support. Catalysts synthesized by different techniques (DP and UV-assisted DP) and with different gold weight contents exhibited almost the same activation energy in the Arrhenius plots, which strongly suggests a common active site in all of them, which was thought to be $Au–O_x(OH)$-**S** site, where **S** is the support. [62]

It is even possible to modify the surface of non-reducible oxides, so that they become active for PrOX-CO and WGS. Li and co-workers recently reported that it was possible to create oxygen vacancies on the surface of ZrO_2 by etching oxygen atoms under a hydrogen flux.[63] When gold was supported on this modified version of ZrO_{2-x}, it was active for the LTS reaction. Normally, Au/ZrO_2 exhibits poor WGS activity and does not event stand competition when compared to with catalysts supported on reducible metal oxides, however the Au/ZrO_{2-x} exhibited remarkable activity of the WGS reaction. This etching technique was successfully applied to conventionally prepared TiO_2 and TiO_2 nanoribbons.[63]

Recently, hydrogen-etching technology was applied as a successful approach to stabilize oxygen vacancies on the surface of TiO_2 According to the synthesis procedure, white anatase was synthesized under calcination in an air flux, while thermal treatment at 550 °C for 4 hours under high-purity H_2 atmosphere resulted in its conversion into black TiO_{2-x} support.[64] Gold deposited on this black modified anatase sample exhibited a higher and more stable WGS activity than that of gold supported on traditional white titania, as shown by comparing temperature dependences of CO conversion, TOF's, and CO conversion during a 30-h stability test at 600 °C. Numerous structural analysis techniques (EPR, Raman, H_2-TPR, HRTEM, XRD, XPS) provided details on how this hydrogen-etching method contributed to increase the abundance of stable surface oxygen vacancies, which increased availability of more metallic gold species at the surface, more active catalytical sites for adsorption of CO molecules and, therefore, higher activity for WGS and PROX-CO reactions.

The authors of this paper also applied this hydrogen-etching technology to prepare blue-black TiO_{2-x} nanoribbons and came up to analogous conclusions for the effect of reduction treatment to increase the number of oxygen vacancies on the oxide surface. [63]

1.4.3 - Unsupported gold catalysts

In addition of the catalytical systems based on gold NP's supported on a vast range of inorganic supports previously discussed, there has been the report of

catalytical systems based on unsupported gold nanoparticles successfully applied to PROX-CO reaction.

Haruta et al. applied gold powder prepared from colloidal metal particles with diameters of *circa* 20 nm to CO oxidation as well as to H_2 oxidation and reported that this unsupported gold catalyst was more active for H_2 oxidation than for CO oxidation. [65]

However, subsequentially Schaefer et al. revealed that a sample consisting of nanoporous gold (np-Au) surface can stabilize a large amount of atomic chemisorbed oxygen at a total coverage of ~0.8 monolayer at 120 °C and were able to promote CO conversion at 20 °C within 24 h. Full CO conversion was maintained for 100 min over these catalysts at 80 °C under realistic conditions (1 % CO, 1 % O_2, 50 % H_2, 10 % CO_2, 10 % H_2O, space velocity = 240,000 mL h^{-1} $gcat^{-1}$) with 100 % CO_2 selectivity. [66]

However, coarsening of the nanopores (which has been attributed to the fast diffusion of the gold atoms at the chemically active surface due of the exothermicity of CO oxidation) was the major drawback of these np-Au catalysts. The average particles diameter increased from an original value of 8 nm to *circa* 15 nm after reaction at 20 °C and increased to over 40 nm after reaction at 80 °C.

In a completely novel approach to synthesize a PROX-CO catalytical system, Kim et al. demonstrated that selective oxidation of CO in H_2-rich gas mixtures can be accomplished by making use of a catalyst system composed of aqueous polyoxometalate (POM) solutions, such as [$H_3PMo_{12}O_{40}$], and gold nanoparticles on carbon (0.8 wt% Au, d_{Au} = 10.5 nm), where POM plays the role as an oxidizing agent for reaction of CO with liquid water and as an energy-storage agent for electrons and as an oxygen carrier to curtail the H_2 oxidation. [67]

The authors proposed that at first, water molecules are adsorbed on gold surface and dissociates heterolytically forming a hydroxy group adsorbed on the metal surface and hydrogen atom that is subsequently oxidized by transfer of an electron into the metal and formation of a proton stabilized in liquid water. The electron is then transported through the metal to the reducible POM species present on the metal. Subsequently, CO molecules react with -OH groups adsorbed on the gold surface leading to the formation of a COOH intermediate that subsequently decomposed into CO_2 and a proton.

The gold was neither sintered nor lost in solution by leaching, unlike other metals such as Pt and Ir. As CO molecules are not strongly chemisorbed on the Au surface, this allowed them to desorb easily as CO_2, differently from what happened to other metals, such as Pt and Pd, that got poisoned and rapidly lost their catalytical activity.

At room temperature, CO could be oxidized to CO_2, and in the presence of CO, the oxidation of H_2 was inhibited. The authors observed 10-20 % loss of the initial catalytic activity after the initial use, but stable activity was maintained at levels of at least 50 % of the initial activity after exposure of the catalyst to 0.05 mol L^{-1} POM solution for 3 months.

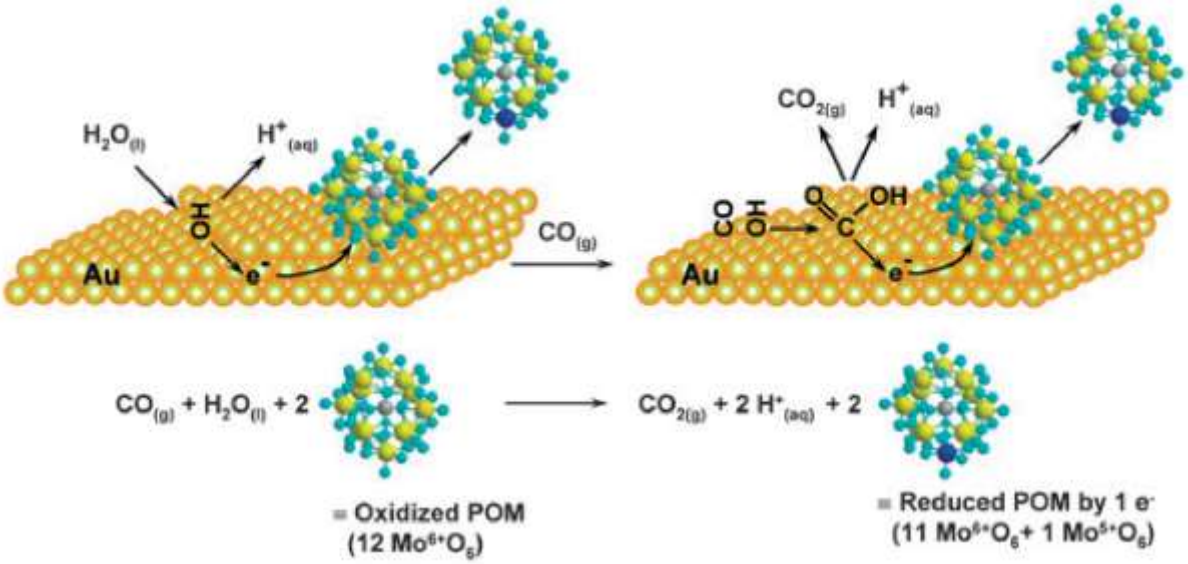

Figure 5. Reaction schematic for CO oxidation using aqueous polyoxometalate ($[H_3PMo_{12}O_{40}]$) solutions over gold catalysts. The POM reduced by 1 electron is represented by showing 1 Mo atom in the distinct blue color of the reduced compound, the other Mo centers are yellow, O turquoise, P gray. Image adapted from [67].

The investigation revealed the sensitivity of the catalyst to different pre-treatments and identified sub-nanometre Au(0) nanoparticles as the active species. The co-ordination number of Au throughout the reaction did not change and while $Au^{\delta+}$ was also stable during the reaction, it was found that Au(III) species were short-lived under the reaction conditions.

1.5 - Deposition methods for deposition of Au NP's over oxide surfaces

Depositing Au NP's over metal oxide nanoparticles by impregnation methods is not as easy as it is for other metals, such as Pd and Pt. Nanometric gold tend to show low melting point and to exhibit lower affinity for metal oxides, which makes the process more difficult. Furthermore, Au NP's are usually obtained from tetrachloroauric acid, $HAuCl_4$, which is the most widely available gold precursor.

During the annealing process in order to eventually obtain the metallic NP's, remaining chloride ions from the precursor are known to form bridge bonds between gold atoms, which might lead to a process of particle sintering and loss of catalytical activity.

As summarized in Table 2, there are in the literature four categories of methodologies to be carried out in order to obtain Au NP's with diameter below 10 nm over a range of different supports, i.e. carbonaceous materials, single crystals, or acidic or basic oxides. They are described in the following sections.

1.5.1 - Preparation of mixed precursors of Au and the metal component of the supports

The first category consists on the synthesis of well-mixed gold precursors (i.e. hydroxide, oxide or the element *per se* in its metallic form) together with the component of the support by different techniques, such as *coprecipitation*, *amorphous alloying* or *co-sputtering*. The mixed samples are annealed in air at temperatures above 550 K, transforming Au precursors into metallic nanoparticles strongly anchored to crystalline metal oxides. This technique can be applied to salts of metals in the first row of the transition series in groups 4–12 and to Al and Mg, which can be precipitated as hydroxides or hydrated oxides. [68]

Among the vast number of techniques available, coprecipitation is the most convenient and simplest of the preparation methods. It consists of mixing up an aqueous solution of $HAuCl_4$ and water-soluble metals salts, in preference nitrates, pouring them together into an alkaline aqueous solution under stirring for a few minutes.

Table 2. Preparation Techniques for Nanoparticulate Gold Catalysts. Adapted from [68].

	Preparation technique	Compatible Support Material
Strong interaction of Au precursors with support materials	deposition-precipitation ($HAuCl_4$ in aqueous solution)	$Mg(OH)_2$, Al_2O_3, TiO_2, Fe_2O_3, Co_3O_4, CeO_2
	liquid-phase grafting (organogold complex in organic solvent)	TiO_2, MnO, Fe_2O_3
	gas-phase grafting (organogold complex in vapour phase)	Most of them, including SiO_2, Al_2O_3
Mixing colloidal Au with support materials	Colloid mixing CM	Activated C, TiO_2
Preparation of mixed precursors of Au and the metal component of the supports	Coprecipitation of hydroxides or carbonates CP	$Be(OH)_2$, SnO_2, Mn_2O_3, Fe_2O_3, Co_3O_4
	Amorphous alloy formation	ZrO_2
	Co-sputtering of oxide in presence of O_2	Co_3O_4
Model catalyst	Vacuum deposition (at low temperature)	Defects are the site for deposition – MgO, SiO_2, TiO_2

Gold hydroxide, which seems to be the intermediate gold species prior to the formation of gold nanoparticles, is an amphoteric compound whose solubility increases at high values of pH due to the tendency of forming $Au(OH)_4^-$, a water-soluble species, which justifies why the most efficient range for the precipitation is 7–10 in this technique. [69]

In order to increase the pH, common inorganic bases, such as NaOH, KOH or NH_4OH, or even basic salts, for example, Na_2CO_3 or Li_2CO_3. When these compounds are used, pH inevitably changes during the process of precipitation

which usually leads to broad NP's size distribution and uneven distribution of metallic particles over the oxide surface. Nevertheless, it has been recently reported that when homogeneous precipitation is performed with slow-decomposing reagents, such as urea or hexamethylenetetramine (urotropine), after ageing for some hours, higher crystallinity, smaller size, higher specific surface area and higher average pore diameter Au NP's might be obtained.

Aqueous solutions for coprecipitation should be warmed to a temperature in the range of 320-360K to promote the exchange of chloride from the $AuCl_4^-$ ion with OH^- ions. Most authors indicate that after co-precipitation the solid is supposed to be washed until no chloride is detected in the washing solution (i.e., detection reaction with silver nitrate).[68]

1.5.2 - Mixing colloidal Au with support materials

In the second category, monodisperse gold nanoparticles colloids are prior synthesized via classical Au NP's synthetical methods, in which $HAuCl_4$ is reduced yielding metallic gold nanoparticles, which are stabilized by the addition of capping agents, in order to prevent them to flock together. Several of these agents have already been reported by literature, such as citrate ion (in the classical Turkevich methodology developed in the 1950's), polyvinylpyrrolidone (PVP), tetrakis(hydroxymethyl)phosphonium chloride (THPC) or cetyltrimethylammonium bromide (CTAB). [68]

These sols made up of these capped Au NP's are subsequently are put together with the target oxide particles aimed to be decorated with gold nanoparticles, however substrates surfaces are usually not fully compatible for Au NP's deposition. For this reason, the oxide surfaces must be previously functionalized with organosilanes linkers, such as MPTMS, APTMS, APTES. One part of these linkers connects to the oxide surface via covalent silicon-oxygen bonds, while at the other extremity of the molecule, a polar moiety, such as an amino or a thiol group, enables the anchoring of the gold nanoparticles.

The main advantage of this technique lies principally in the fact that it is suited regardless of the type of support employed and the feasible control on particle size/distribution, obtaining normally metal catalyst with good dispersion.

1.5.3 - *Deposition or adsorption of Au compounds into the oxide surface*

The third category relies on the deposition or adsorption of Au compounds onto the oxide surface, which is previously synthesized in the desired morphology in the final catalyst composition. This category might be based on the deposition-precipitation of gold (III) hydroxide, liquid-phase grafting or even gas-phase grafting of an organogold complex, such as dimethyl(acetylacetonate) gold (III), onto the desired surface.

The DP method is the easiest to handle and the one used for making Au catalysts in industrial scale. In the DP method, a metal precursor is dissolved into an aqueous suspension of the support and subsequently precipitated as a hydroxide by increasing the solution pH. The support surface plays the role as a nucleating agent and accounts for the key factor of this preparation method that is the prevention of precipitation away from the support surface. Nechayev et al reported that Au adsorption on alumina, a frequently chosen support oxide, is maximized at pH values close to the isoelectric point, $IEP_{alumina}$ = 8, that is, at a pH at which the number of neutral OH is maximized. [70]

Machesky et al has already reported that the deposition extent is not only dependent on the number of hydroxyl groups on the surface, but also on the degree of hydroxylation of the ionic gold species. He and collaborators accounted that the deposition-precipitation efficiency of hydroxochloro complexes on goethite (FeOOH, IEP = 8.1) to form gold metallic NP's increases as pH is increased from 4 to 7, which is the opposite trend behaviour expected for anion adsorption on positively charged oxide surfaces. This backward tendency is attributed to a shift in Au composition distribution as the pH is increased from 4 to 7, decreasing the fraction of gold present as $AuCl_4^-$ and increasing the amount as $AuCl(OH)_3^-$ and $AuCl_2(OH)_2^-$. It seems likely that the more hydroxyl groups are present in the hydroxochloro gold complexes ions in solution, the higher the interaction between the hydroxyl groups on the surface and the gold precursor ions, probably by a mechanism that involves the formation of crossed hydrogen bonds followed by chemisorption. [71]

All this in account leads to the conclusion that DP technique achieves its best performance in the 7-10 pH range, the same as in the coprecipitation technique. Inside this range, several oxide isoelectric points are found, such as for CeO_2, NiO, ZrO_2.

If low values of pH are used, most of the hydroxyl groups are protonated, preventing the approximation of hydroxochloro gold complexes ions and, furthermore, gold will be entirely found as $AuCl_4^-$, which was discovered to be not the best species to interact with the surface hydroxyl groups. Therefore, very-low isoelectric point oxides, such as V_2O_5 (IEP =1.5), SiO_2 (IEP = 2) or MnO_2 (IEP = 2.5) are not suited for this technique. Another support which is totally incompatible for DP is carbon, as there are no hydroxyl groups on the surface of activated carbon supports.

Inside this category, another technique named *liquid-phase grafting* is also inserted. By this method, a freshly precipitated metal hydroxide is impregnated with an organic solution of a gold precursor, such as $Au(PPh_3)(NO_3)$ in acetone. Vacuum drying at room temperature and calcination in air followed leading to the production of the gold catalyst. Differences between similar catalytical systems have been attributed mainly to changes of the Au particle size distribution occurring during calcination. [72]

And the third technique inside this category is the *gas-phase grafting*, which is highly efficient and does not suffer the limitation of DP preparation, i.e., it is suited to any kind of support and not limited to the preparation pH. By this technique, a gold coordination complex compound, such as methyl(acetylacetonate) gold (III), $Me_2Au(acac)$, is vaporized inside a vacuum chamber by heating and subsequently deposited over the support. For this specific case of oxide supports, the process of grafting the gold species on the surface involves ligand exchange processes between $Me_2Au(acac)$ and the surface hydroxyl groups, where the acetylacetonate group interact with the OH groups via hydrogen bonding. After the process of deposition, the samples are then annealed at T > 500 K to burn out the organic ligands attached to gold.

A improved impregnation preparation by gas-phase grafting method reported by Wu *et al.* [73], named *solvated metal atom impregnation* (SMAI), involves the preparation of an air-sensitive and thermally-unstable bis(toluene) gold(0) complex solution at -196 °C under dynamic vacuum. The mean diameter of Au particles

prepared by SMAI, results in generally smaller particles than those prepared by conventional impregnation preparation methods.

Due to the high toxicity and dangers commonly associated with gold organometallic complexes, alternatives which make use of metallic gold have been target to intense research recently. In the first one of these alternatives named *magnetron sputtering*, a high purity gold precursor sample can be attached to a magnetron source that is sputtered at an applied power of 14 W in an argon plasma. The magnetron sputtering process entails deposition of an atomic flux of Au atoms onto the support surface where the atoms nucleate and grow to form clusters nanoparticles due to the low interfacial binding energy between the gold and the support. When an insufficient concentration of deposited material is employed might lead to the undesired creation of a metallic thin-film or coating on the substrate. The sputtering process is said to be a line-of-sight technique, so only surfaces directly exposed to the metal flux will be prone to form metallic particles. Thereupon, catalysts are grown in “egg-shell”-like configurations on the outside of a support material and not within a support material or within the microporous structure. Gold loading and particle size are a function of deposition time, material volume, and the exposed surface area. This is why it is possible to deposit Au NP’s over hydroxyl-free surfaces, such as active carbon or graphite. by gas-phase grafting.

Another alternative to using gas-phase grafting without resorting to gold organometallic compounds is the technique named *solvated metal atoms dispersion* (SMAD).

A bulk metal sample is vaporized under vacuum by resistive heating or electron beam exposition and subsequently deposited on the walls of a reactor cooled with liquid nitrogen at -196 °C in the presence of vapours of an organic solvent. Polar, organic solvents can be employed, such as acetone, ethanol, isopropanol, dimethyl sulfoxide (DMSO) and dimethylformamide (DMF). During the cooling process, the metal atoms get trapped inside the frozen matrix of the solvent and prevented to recombine to form again the bulk metal. After the solidification step is complete, the frozen matrix is warmed until the solvent melts. When this frozen metal/organic mixture is heated up, metallic NP’s nucleate and grow until a point a colloidal dispersion of the metal is then obtained. Colloid stability in this case is apparently achievable due to solvation effects of the solvent combined with

electronic effects of electron scavenging exerted by the solvent molecules to form negatively charged colloidal particles.

This solution is allowed to get in contact with a previously treated catalyst support, whereupon metal atoms nucleate on the support surface. Variables such as the metal concentration, temperature and impregnation time, and also evaporation rate and method, solvent polarity and viscosity can be modulated, all of which influencing the final metal particle size and morphology.

The major drawbacks in employing SMAD for making a supported Au catalyst are the need for metal vapor reactors and skilful experimentalists to operate them as it is not a routine experimental procedure, scarce reproducibility of the method due to the poor control in the evaporation of bulk metal and the fact that scaleup has not been demonstrated. [74]

1.6 - The Mechanism of PROX-CO reaction on Promoted PGM Catalysts

1.6.1 - Nonpromoted PGM catalysts

For the PROX reaction occurring on the nonpromoted PGM catalysts, there is a process of competitive adsorption on the same active sites between the three molecule that compose the flux: O_2, CO, and H_2. At low temperatures, the surface is covered predominantly with adsorbed CO, whereas O_2 and H_2 can be adsorbed on the surface at high temperatures only when the desorption of CO gets more favourable as indicated in Figure 6.

Therefore, the desorption of CO from the surface or the adsorption of O_2 is proposed as the rate-determining step on the nonpromoted PGM catalysts. Taking in account much of the literature that has been published about PROX-CO reaction up to this day, the reaction over Al_2O_3-supported noble metal catalysts can be expressed by a simple power-law rate equation as indicated in Equation 4 [75-77]

$$r = A\ exp(-E_a/RT)\ P_{CO}^{\alpha}\ P_{O_2}^{\beta} \qquad (4)$$

in which, r is the reaction rate; A is the exponential factor; E_a is the activation energy, and α and β are the reaction orders for CO and O_2 pressures, respectively.

The apparent activation energy is found to be in the range of 70−100 kJ/mol at temperatures up to 200 °C, increasing at higher temperatures and CO partial pressures. The reaction orders are found to be negative for the CO partial pressure and positive for the oxygen partial pressure, respectively.

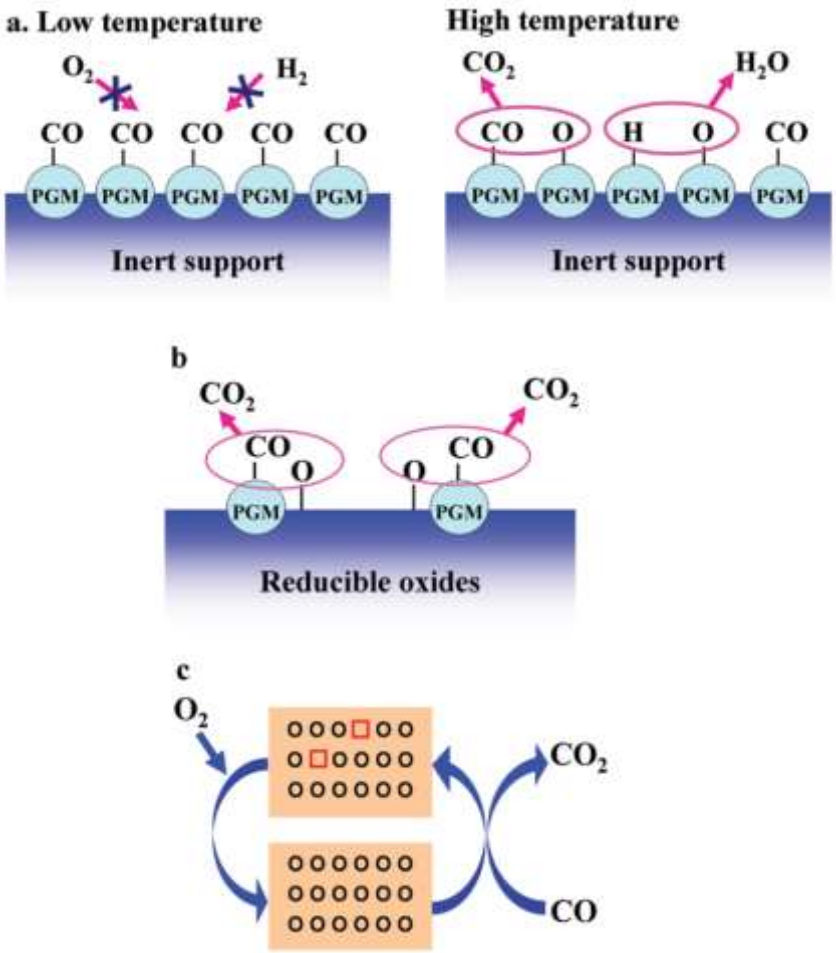

Figure 6. Different reaction pathways of PROX: (a) competitive Langmuir−Hinshelwood mechanism over nonpromoted PGM catalysts, (b) non-competitive Langmuir−Hinshelwood mechanism over promoted PGM catalysts, and (c) Mars−van Krevelen mechanism over promoted PGM catalysts. Image adapted from [81].

The kinetical data obtained for this kind of systems are consistent with a *Langmuir−Hinshelwood reaction mechanism* in the low-rate branch, on a surface predominantly covered with adsorbed CO. Such a competitive

Langmuir−Hinshelwood reaction mechanism predicts quite well the low activity of noble metals at low temperatures owing to the inhibiting effect of CO adlayer preventing the adsorption of O_2 molecules. Increasing temperatures leads to the desorption of CO so that O_2 can be adsorbed and activated on the surface of noble metals.

1.6.2 - Promoted PGM catalysts

For the case of MO_x-promoted PGM catalysts, the widely accepted mechanism is the non-competitive Langmuir−Hinshelwood mechanism in which CO molecules that are adsorbed on the noble metal sites reacts with O atoms provided by MOx at the interface of the noble metal and MO_x, as indicated in Figure 6. According to this mechanism, the adsorption and activation of O_2 is no longer a rate-determining step, as it has already been demonstrated by numerous kinetical studies for this type of system. [78]

The kinetics of the PROX reaction over this kind of catalysts can also be expressed by the same power-law rate equation as shown in the previous section, but for this case β = 0. E_a was found to be smaller when compared to the nonpromoted PGM catalysts, which was in the range of 5-44 kJ/mol. The reaction order was found to be positive for CO partial pressures on IrFe catalyst produced by Kim and collaborators, implying that the poisonous effect of CO is eliminated by introducing promoters. [79]

On the other hand, since MOx's classified in the category of reducible oxides, such as CeO_2 or FeO, are easily reduced at the reaction temperature with the aid of PGM's located on their surface, the *Mars-van Krevelen mechanism* (MvK mechanism also named *redox mechanism*) has also been proposed to describe PROX-CO reaction. By this mechanism, which is depicted in Figure 6, surface lattice oxygen atoms directly take part in the CO oxidation reaction. For example, Huang and collaborators studied a catalyst based on an Ir/CeO_2 system in which iridium nanoparticles particles are embedded in a ceria matrix and they concluded that the strong interaction with the ceria support could get surface Ce-O bonds weaker and facilitate the formation of more reducible oxygen. [80]

In general lines, by the MvK mechanism, CO molecules firstly interact with an oxygen atom on the ceria surface and extract it, creating an oxygen vacancy. The O_2 molecules in the gas-phase, subsequently adsorb on the vacancies via an interaction stablished between their electronic cloud and the electron-deficient sites in the vacancies, being the role of the O_2 molecules to heal these vacancies.

As the O_2 molecules displace their electronic cloud to the vacancies, they become electron-deficient and activated prone to suffer nucleophilic attacks by other molecules. The activated O_2 reacts with CO to form a carbonate ion adsorbed on the surface, which decomposes to release CO_2 and heals the oxygen vacancy; thus, this way closing the catalytic cycle from CO to CO_2, without direct participation of noble metals for providing CO adsorption sites.

Despite the fact that evidences for the MvK mechanism have been provided for Au/MO_x systems, a similar mechanism may be applicable to PGM/MO_x catalysts, taking in account the fact that the chemical behaviour of many PGM NP's resemble that of Au NP's in promoting the reduction of MO_x support at a significantly decreased temperature, which has been confirmed by Liu et al. that did indeed find out that Pt/ FeO_x and Pd/FeO_x catalysts also followed the noble metal-assisted Mars−van Krevelen mechanism in the PROX reaction. [81]

Notwithstanding, it must be kept in mind that various types of mechanisms may work together for some catalyst systems, depending on the reaction temperature. For example, Wootsch suggested that four types of reaction mechanisms would be accouted simultaneously in Pt/$CeZrO_x$ catalysts: (i) a competitive Langmuir−Hinshelwood mechanism on the Pt particles; (ii) a non-competitive Langmuir−Hinshelwood mechanism on the interface of Pt and $CeZrO_x$, which was predominant at 90−130 °C; (iii) a hydrogen oxidation on the $CeZrO_x$ support; and (iv) a WGSR at high temperatures. [81]

The interaction between the MO_x surface and the noble metals NP's not only provides reactive oxygen but also weakens the adsorption of CO on the noble metal sites due to the strong interaction between the noble metals and the MO_x. For PtFe or IrFe catalysts, FTIR, TPR, and TPD data revealed that CO coverage and metal-CO bond strength on Pt or Ir were significantly lowered by the addition of FeO_x. However, it should not be concluded straight away that the weaker the CO adsorption, the higher the activity or selectivity. It was reported that the easier CO desorption from the niobia-promoted Pt catalyst resulted in lowering in the selectivity

for CO oxidation, as the CO molecules ended up desorbing too fast and accelerating instead the H_2 oxidation reaction to H_2O.

For Rh/Nb_2O_5 catalyst, although the chemisorption ability toward CO changed drastically by the strong metal−support interactions induced by the calcination or reduction treatments, no direct correlation between the CO chemisorption ability and the activity and selectivity has been found.

1.7 Size of Au NP's and its impact on the PROX-CO performance

The size of supported gold particles is one of the most pivotal factors in the synthesis of active catalysts for various reactions, including several of relevant industrial importance, such as the oxidation of alcohols, oxidation of carbon monoxide (CO), and various selective hydrogenation reactions (e.g. p-chloronitrobenzene to p-chloroaniline or crotonaldehyde to crotyl alcohol). A general opinion exists that the abundance of small gold particles on the catalyst surface guarantees good performance. However, in the case of CO oxidation, one of the most studied gold-catalyzed reactions, Valden et al have observed an optimum gold particle size over Au/TiO_2 ranging from 2.5 to 3.0 nm due to quantum size effects with respect to gold particle thickness. [82]

Some of the above-commented works focused on stablishing a relationship between the performance for PROX-CO and gold particle size and it was claimed that the presence of very small gold particles contributed not only to increase the rates of CO conversion but also of unwanted hydrogen oxidation. [82]

Very recently, Qiu et al. (2019) studied the relationship between catalytic behaviour in PROX-CO reaction, dispersion and oxidation states of active Au species in a series of Au/CeO_2 catalysts with gold loading ranging within 0.05-1.2 wt.%. Based on previous reports that had already came out to the understanding that the strong interaction between gold and ceria relies on an electron density transfer from Au to Ce, which ultimately leads to the partial oxidation of Au (creating $Au^{\delta+}$ species) and partial reduction of Ce(IV) into Ce(III) and has a strong effect on catalytic activity, they have reported a higher CO oxidation activity registered at a low temperature with an increase in gold amount up to 0.6 wt.%. A further increase in

gold content gave rise to lower CO conversion and selectivity, probably due to the competition with undesired side reactions. [83]

As it was quite difficult to notice any particles in transmission microscopy images in low gold content samples, it was suggested that gold was present as highly dispersed particles. However, larger particles were verified at a higher gold loading, estimated to be about 4 nm in 0.6 wt.% Au/CeO_2 and 10 nm in 1.2 wt.% Au/CeO_2 samples, thus explaining diminished activity. XPS analysis and in situ DRIFTS measurements allowed them to explain the best performance of low loaded Au/CeO_2 (0.3 wt.% Au) with stabilization of $Au^{\delta+}$ species by strong Au–support interaction.

More information about particle size effects on gold-catalysed PROX reaction were gained by preparation of series of gold catalysts by Beck et al with well-defined gold nanocrystals of three different average sizes of about 2.1, 3.8, and 7.3 nm supported on CeO_2, ZnO, and Al_2O_3. Regardless of the employed support type, samples with the smallest gold particles always exhibited the highest reaction rates and the increase in size caused a drop of gold activity over all three supports. Based on the correlation between particle diameter and reaction rate, it was suggested that in the case of Au/CeO_2, the most active species were perimeter corner sites consisting of low coordinated gold in close contact with ceria. [81]

According to previous literature report, corner and edge sites are the centers where hydrogen dissociation also proceeds. [84] In view of this, the finding of Beck et al. for higher selectivity over samples of smaller gold particle size implies that depending on the experimental conditions, the CO oxidation could dominate over dissociative hydrogen adsorption. These very last findings confirm the importance of highly dispersed gold nanoparticles (2–3 nm) for the CO oxidation activity during PROX.

1.8 - The Roles of the OH Group in PROX-CO mechanism

The PROX-CO mechanism is frequently assumed as the competitive reaction of CO and H_2 with O_2. Taking in account this bias, the presence of H_2 will impose only the negative effect of decreasing the selectivity of CO oxidation. This is the actual case at high temperatures. However, the presence of H_2 is observed to have

instead a remarkable improvement for the low-temperature CO oxidation reaction. Moreover, this effect is much more conspicuous when a reducible oxide, such as CeO_2, or an alkali promoter is present. [81]

It is visible that this promotional effect cannot be accounted thoroughly by the competitive reaction mode previously described. In order to provide a deeper understanding of the effect of H_2 or H_2O, both the kinetic and theoretical calculations have been conducted, and various reaction mechanisms have been proposed accordingly.

Tanaka and collaborators investigated the intermediates dynamics for low temperature PROX-CO reaction over FeO_x/Pt/TiO_2 and Pt/carbons with *in situ* DRIFT technique and proposed that hydroxyl groups participate directly in the CO oxidation reaction through the following pathway: [81]

$$CO_{(ads)} + OH^- \rightarrow HCOO + e^-$$
$$O + e^- + H^+ \rightarrow OH$$
$$HCOO + OH \rightarrow CO_2 + H_2O$$

According to this mechanism, the reaction between the formate ion (HCOO) and hydroxyl groups is regarded as the rate-determining step.

Alkali metal cation effect on increasing OH concentration

It is known from the literature that alkali metal doping in oxide supports is usually associated with enhancement of PROX-CO and can bring about up to a 10-fold enhancement in the low temperature PROX activity. It has been suggested that the promotional role of alkali metals is also closely related to the increased concentration of OH groups neighbouring to the noble metals.

According to these observations, the promotional role of alkali metals can be understood in two aspects: one is to stabilize the active Pt atoms, and the other is to provide the reactive OH species neighbouring to the Pt atoms. [81]

Further remarks about OH group reactivity on PROX-CO catalysis

In the above examples, the OH groups are associated with the presence of promoters, either on the reducible oxide support or on the alkali metal-promoted oxides surfaces. Quite different from these examples, Fukuoka's group found that Pt nanoparticles supported on FSM-type mesoporous silica were extremely active and selective for the PROX of CO; both the CO conversion and the CO_2 selectivity were above 95% at 25−150 °C over Pt/FSM-16. By using an isotopic tracer technique in combination with the IR experiments, the authors concluded that the OH groups at the internal surface of mesoporous silica are reactive toward CO to produce CO_2. [81]

Such an unprecedented reactivity of OH groups on the silica surface appears to be closely related with the pore structure and pore size. Since only a very limited number of mesoporous silica possess such highly reactive OH groups, a more rational correlation between the reactivity of OH groups and the silica structure need to be established.

The important roles of OH groups are also demonstrated in the effect of water. It is commonly observed that the addition of water to the reaction stream or the pre-treatment of catalyst with water vapor can lead to a large increase in the activity for a low-temperature PROX reaction. It could be suggested that such enhancement could be attributed to WGS that would promote the depletion of CO, but no evident WGS reaction was detected on most of the noble metal catalyst systems at relatively low reaction temperatures. Then this behaviour was then attributed to the formation of oxidant hydroxyl groups on the catalyst surface.

The mechanism of the reactions then proceeds differently according to the support in which the noble metals NP's have been anchored.

1.9 - Mechanism of PROX-CO in the case of Au catalyst over a non-reducible oxide support

Quinet et al. proposed that the mechanism of PROX-CO for the case of catalyst composed of Au NP's over a non-reducible oxide support, more specifically Au/Al_2O_3, and concluded that the mechanism proceeds by two cycles: *the CO oxidation cycle and the H_2 oxidation cycle*. The reactions continuously shift from H_2 oxidation to CO oxidation as the temperature decreases. [85]

The mechanistic details for the CO oxidation are as follows: molecularly adsorbed O_2 is activated on Au by reaction with H_2 to form OOH* and H* species; this mechanism does not require O_2 dissociation on Au, and CO* reacts with OOH* to produce CO_2 and OH*; OH* then reacts with CO* to produce CO_2 and H*. The cycle is closed when the two H* species recombine into H_2 or react with O_2 molecules to form new OOH* species. The direct oxidation path dominates over the indirect path in the water-promoted CO oxidation, whereas the indirect carboxyl path plays a role of great importance in the WGS and PROX simulations:

$$CO^* + OOH^* \rightarrow CO_2OH^*$$
$$CO_2OH^* \rightarrow CO_2 + OH^*$$
$$CO^* + OH^* \rightarrow COOH^*$$
$$COOH^* \rightarrow CO_2 + H^*$$
$$H^* + H^* \rightarrow H_2$$

By this mechanism, the formate path was suggested to be unimportant for PROX-CO. Clearly, under the conditions that two H* species recombine to form H_2, hydrogen acts as a “catalyst” for CO oxidation.

The *mechanistic details for the H_2 oxidation* are as follows: dissociative adsorption of H_2 and adsorption of molecular O_2 on gold generate OOH* species (for this step, an *Eley-Rideal mechanism* (O_2* + H_2 → OOH* + H*; or O_2 + H* → OOH*) proceeds). [84]

Next, reaction of a gold-carbonyl (Au-CO) species with the gold-hydroperoxide (Au-OOH) may involve the formation of a bicarbonate ion (CO_2OH*) with subsequent decomposition to a gold–hydroxyl (Au-OH) and CO_2* adsorbed at the particle-support interface. After CO_2 release, the second CO* involved in the cycle reacts with OH* on gold to form H* and CO_2 via the hydroxycarbonyl intermediate decomposition. Associative desorption of H_2 or reaction of H* with O_2 and desorption of CO_2 close the catalytic cycle.

1.10 - Mechanism of PROX-CO in the case of Au catalyst over a reducible oxide support

Given that the lattice oxygen of ceria can participate in the reaction (either without gold or enhanced by gold), the Mars-van Krevelen mechanism gains prominence, in addition to the gold perimeter effects. The reaction mechanism involving hydroperoxy intermediates has been proposed for CO-PROX over the Au/CeO_2-Co_3O_4 catalyst, which may proceed via the reaction of Au-CO with hydroperoxy (OOH) intermediates.

Initially, Au undergoes oxidation to form an effective ‘‘Au–oxide’’ ($Au^{\delta+}$) species, and H_2 that is dissociatively adsorbed on gold which then recombines with the atomic oxygen in the Au–oxide to form –OOH and/or –OH species. CO adsorbed on the metallic Au sites then reacts with the highly active –OOH intermediate to form CO_2, and simultaneously leaves behind a hydrogen atom (H*) and an oxygen vacancy in the Au–oxide. [84]

An O_2 molecule is subsequently adsorbed and activated on the oxygen vacancy, which then reacts with the remaining H* to form new –OOH species and initiates the CO oxidation process again. However, the pathway involving conversion and decomposition of carbonate-like species to CO_2, induced by water, cannot be excluded from the reaction mechanism and it is known that might take place simultaneously, as previously discussed.

Evidence substantiating the predominant operation of the gold-assisted Mars–van Krevelen mechanism has been vastly provided in the literature. [85] The low temperature CO-oxidation proceeds via inclusion of adsorbed CO into the Au-OH bond, resulting in formation of a hydroxycarbonyl, which undergoes oxidation to generate a bicarbonate, followed by decarboxylation into CO_2 and Au-OH. Because the oxide support lattice-activated oxygen is available, the mechanism may differ from that of gold supported on inert oxides, where the oxygen supply originates mainly via direct dissociative adsorption on the gold particles.

The rutile TiO_2 (110) support energetically favoured H_2 dissociation on the gold clusters, and the active sites for H_2 dissociation were located at the corners and edges of the gold nanoparticle surface in the vicinity of the support, indicating that the catalytic activity of gold nanoparticles supported on the rutile TiO_2 (110) surface is proportional to the length of the perimeter interface between the nanoparticle and the support.

1.11 - Mechanism of PROX-CO in the case of unpromoted Au catalyst

Evaluation of the effect of molecular hydrogen on CO oxidation over an unsupported gold powder showed that a support-free pathway for the oxidation of CO was operative and is enhanced by the presence of hydrogen. However, this oxidation pathway was less efficient than the oxide-supported counterparts. The adsorbed hydroxyl groups are gradually and simultaneously transformed to gas-phase water in the course of the reaction at increasing temperatures.

The promotional effect of hydrogen is ascribed to highly oxidative H_xO_y intermediates formed from the interaction between H_2 and O_2 on the gold surface [86] Lyalin and Taketsugu demonstrated that the molecular and dissociative adsorption of H2 on Au n clusters containing n = 1, 2, 8, and 20 atoms depended on the cluster size, geometry structure, cluster flexibility, and the interaction with the support material.

In the absence of hydroxyl groups on the support surface, the hydroxyl groups can be produced by the reaction between H_2 and O_2 via the following pathway:

$$O_2 + H \rightarrow HO_2^*$$
$$HO_2^* \rightarrow O^* + OH^*$$

This route is also called *H-assisted O_2 dissociation*, which is with good experimental agreement with the chemical behaviour observed for the promotional effect of H_2 on the CO oxidation over Ru@Pt core−shell NP's systems. For some catalysts, the carboxyl (COOH) intermediates are proposed to play an important role in the PROX-CO reaction. Microkinetic studies of CO oxidation, the WGSR, and the PROX reaction on Pt and Rh catalysts reveal that the CO + O direct reaction in WGS and PROX reactions is slow, and additional CO-H_2 coupling reactions, including the carboxyl and hydroxyl intermediates as well as H_2O, are crucial steps for these processes.[81]

1.12 - Ceria support

Cerium is a well-known light rare earth element. Elemental cerium was first discovered from a mineral named “cerite” by Jöns Jakob Berzelius and Wilhelm Hisinger in Sweden, and independently by Martin Heinrich Klaproth, a German chemist. Berzelius and Hisinger named it after the asteroid Ceres that had just been discovered a few years earlier.

Despite their name, the rare earth elements are moderately abundant elements in the crust of the planet and occur in many minerals. Cerium is the 25th most abundant element on Earth and it is thus almost as abundant as copper in the Earth’s Crust, although it has not found as many applications as the latter.

One of the most important cerium compounds and the most widely employed is cerium (IV) oxide, also known as ceria, a non-natural, ionic solid which crystallizes in a fluorite structure. The popularity has been increasing in recent years in several applications, and in some cases, ceria has been established as an irreplaceable component. It finds uses, such as in: a) automobile three-way catalytic (TWC) converters, where it catalyses redox reactions for gas exhaust pollutant purification promoting CO oxidation process, unburnt hydrocarbon oxidation and reduction of nitrogen oxides, NO_x; b) glasses where CeO_2 is used to decolorize glass by converting green-tinted ferrous impurities colourless compounds; c) polishing products, in which it is the active component due to its special physicochemical properties; d) fluorescent lamps, in which it is used as a photosensitizer e) catalysts for industrially important reactions, e. g. water gas shift, CO and NO_x oxidation. And the ongoing research about ceria mostly orbits in areas, such as heterogeneous catalysis, photocatalysis, fuel cell technology and biological mimetization. [87]

The most unique property of ceria relies on the fact that it is prone to form oxygen vacancies defects, making it suitable for reduction-oxidation processes and catalytic activity systems. Such oxygen vacancy defects improve the oxygen diffusion rate in the ceria lattice, and considerably assist in the high performance of the catalytic reactions. More into details, ceria is a material with high excellent oxygen buffers properties, making it very efficient in terms of reduction-oxidation capability. As mentioned earlier, this situation is attributed to the presence of oxygen vacancies and the concentration of defects m However, this defect may dependent

on reaction parameters such as: *(i)* temperature; (*ii*) oxygen partial pressure; (*iii*) the presence of doping ions; *(iv)* surface stresses; *(v)* electrical field. [88]

Due to the relative easiness of reduction of cerium (IV) ion to cerium (III) ion, when the reduction of ions Ce^{4+} takes place in the lattice, in order to ensure the electroneutrality, there is the generation of oxygen vacancies $V_O^{\cdot\cdot}$, as depicted in Figure 7. This takes place in the proportion of one $V_O^{\cdot\cdot}$ generated for every two Ce^{4+} ions reduced to Ce^{3+}, according to Equation 5 written in Kröger-Vink notation.

$$2Ce_{Ce}^{X} + O_O^X \rightleftharpoons 2Ce'_{Ce} + \frac{1}{2}\,O_2 + V_O^{\cdot\cdot} \quad (5)$$

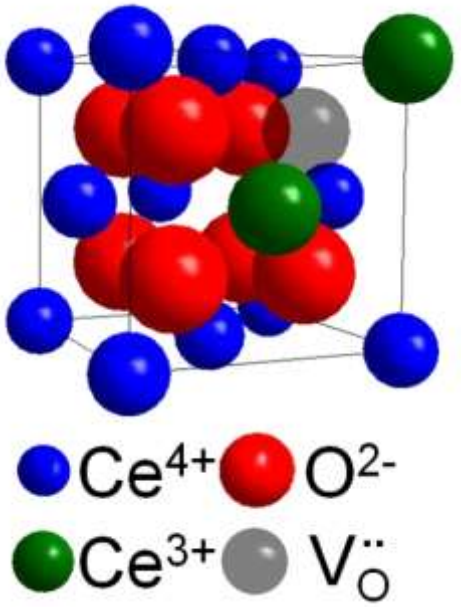

Figure 7. Formation of $V_O^{\cdot\cdot}$ in fluorite-type CeO_2 unit cell. In order to ensure the lattice electrical neutrality, at the time one $V_O^{\cdot\cdot}$ is formed, two Ce^{4+} ions are reduced to Ce^{3+}. Image adapted from Silva [88].

The degree of non-stoichiometry (x) presented by cerium (IV) oxide (CeO_{2-x}) ranges from $0 \leq x \leq 0.5$, i.e. from the extreme case in which all cations are cerium (IV), being represented as CeO_2, to another in which all cations are cerium (III), represented as Ce_2O_3, which would be equivalent to the form $CeO_{1.5}$. Within this range there are several stages of stoichiometry distinguishable from each other, as shown in Table 3, and which are also dependent on the temperature.

The crystalline facets exhibited by CeO_2 crystals in the nanoscale hugely influence its chemical properties. Typically, cube and octahedral morphologies will expose (100) and (111) crystal planes, respectively, while rod morphology expose

mostly (110) and (100) crystal planes while the growing axis of the crystal follows the (110) direction, as highlighted in Figure 8. [89]

It is well known that the *interatomic action force* between cerium and oxygen ions atoms is different for various crystal facets as their interatomic distances are also different from each other. As a result, the energy necessary for extracting oxygen ions and, consequently, the formation energy of the oxygen vacancies is different for each one of the crystal facets. This difference in the nanoscopic level has been exploited in order to develop different nanotechnological applications for CeO_2 and this aspect is known as *shape or morphology-dependent nanocatalysis.*

Table 3. Some of the phases exhibited by CeO_{2-y} at 1 bar pressure. Adapted from Silva [88].

Representation	Oxygen-cerium atoms ratio	Temperature Range (K)	Crystal system/group
F, F', α, α'	2 - x	< 2566	Cubic, $Fm\bar{3}m$
δ	1.818	< 734	Triclinic, $P\bar{1}$
p_1	1.806 – 1.808	< 762	-
ε	1.800	< 856	-
p_2, M19	1.790	< 882	Triclinic
ζ	1.778	< 912	-
T, I	1.714	< 885	Trigonal, $R\bar{3}$
C	(5 ± x)/3	885 - 1676	Trigonal, $R\bar{3}$
A	(3 - x)/2	< 2341	Trigonal, $P\bar{3}m1$

Benzene hydrogenation and CO oxidation reactions are two of many reactions in which CeO_2 can be used as catalyst. When both are compared, the CeO_2 NP's that exhibit the nano-octahedron morphology, in which the (111) facets are predominant, and the nanocube morphology, in which (100) facets are predominant, showed opposite catalytic performance in each type of reaction. [90] The nano-octahedron morphology presented higher conversion rate for the hydrogenation reaction, while the nanocube one showed a higher rate of conversion to oxidation reaction. It has been proposed that the explanation for this behaviour mainly relies on oxygen vacancy formation, which is more thermodynamically

favoured on the (100) facets favouring oxidation, while the vacancies formation is not favoured on (111) facets, favouring hydrogenation.

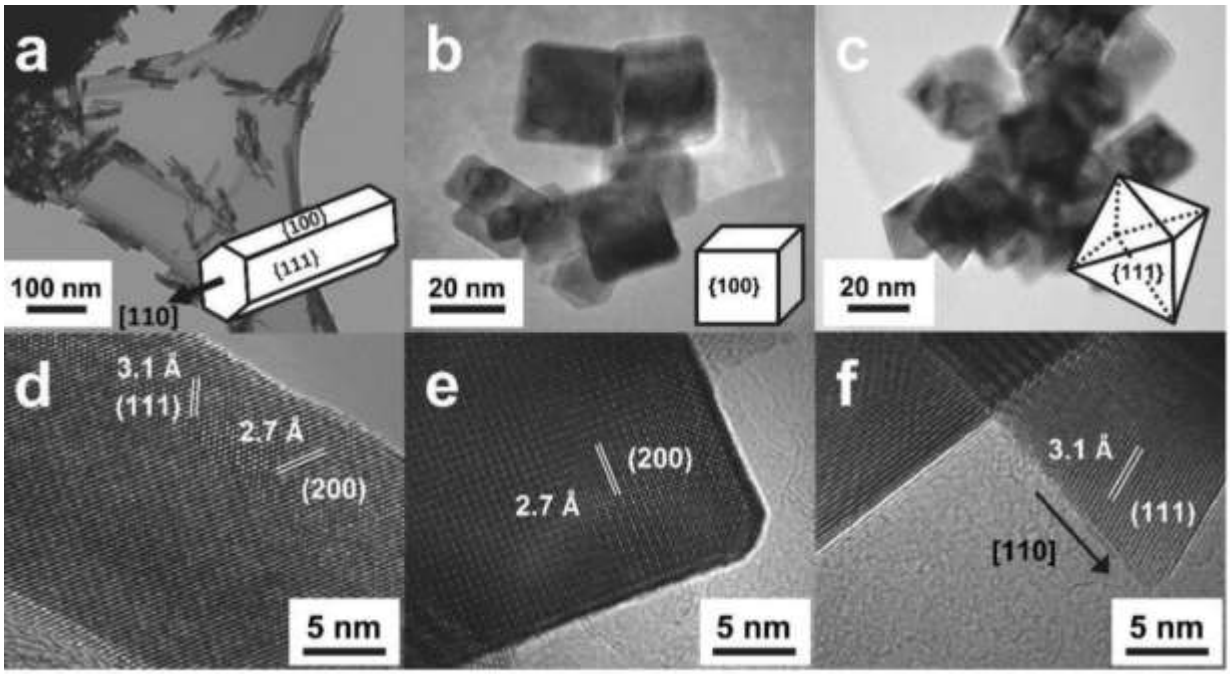

Figure 8. TEM images of ceria nanostructured catalysts: (a) nanorods, (b) nanocubes, and (c) nano-octahedra. (d-f) are the corresponding high-resolution zoom-in images directly below each of the nanostructured ceria. The different exposed facets for each one of the polyhedra are highlighted to each one of them. Image adapted from the [89].

There have been reports of the CeO_2 synthesis in different morphologies, obtained by different synthetic methodologies [91]: rods, wires, flowers, tubes, discs, plates, mesoporous crystals, hollow spheres, cubes and other polyhedra.

Mai et al. [92] synthesized CeO_2 in different morphologies, nanorods, nanocubes and nanopolyhedra, via a hydrothermal synthesis, without the use of surfactants or promoters, and obtained different values of OSC in the following order: nanorods > nanocubes > nano-polyhedra. This difference was attributed to the different crystalline facets exposed in each one of these morphologies.

As there are reports that the easiness of creating an oxygen vacancy at the surface is positively associated with the capacity of the material to be efficient for PROX-CO reaction, this was the reason CeO_2 was chosen as the support material for Au NP's. [92] This will be further discussed in detail in section 4.5. In addition, the hydrothermal procedure developed by Mai was adapted into the methodology conducted in this work and porous nanorods were obtained. A completely novel acid

leaching procedure developed in this work was evaluated to increase the average pore size and positively increase the catalytical capacity of the material. [92]

The Au/CeO_2 system was chosen for the development of this project since the development of robust synthetical procedures for Au NP`s synthesis is one of the main research lines of the Laboratory of Functional Materials and several approaches have already been conducted, including their deposition on metal oxide surfaces. Furthermore, the Au/CeO_2 system exhibits several advantages when compared to similar systems, as previously discussed on section 1.4, such as resistance towards deactivation by water or CO, thermal stability preventing sintering at low temperatures and absence of pyrophoricity.

In addition, another important line of research developed in the laboratory is the conception of experimental procedures for the synthesis of metal oxides in different morphologies, especially cerium (IV) oxide, CeO_2. In addition to syntheses that enable the control of the nanoparticle morphology of this compound, post-synthesis experimental procedures aimed to modify CeO_2 NP`s have also been studied aimed to modify their physicochemical properties with possible applications.

Up to this date, several procedures have been studied aimed to modify textural properties of CeO_2 properties. Esmailpour and collaborators reported that pre-treating CeO_2 with UV light, its catalytical performance in the catalytic ozonation of salicylic acid (SA) can be enhanced three-fold relative to the untreated catalyst as well as outperforming hydrogen-reduced ceria. [93] In an even easier to perform experimental procedure, Silva reported that by grinding CeO_2 nanorods inside a mortar in a process called comminution, it was possible to modify the amount of oxygen vacancies, as confirmed by Raman Spectroscopy, and as a consequence, its catalytical performance in CO oxidation reaction.[88]

In this work, an experimental procedure based on acid solution leaching was performed to expand native pores, which allowed the pores to be expanded and the amount of oxygen vacancies, a structural defect that is intrinsically related to the catalytic capacity exhibited by the material as discussed in the results section.

Furthermore, based on previous works about increasing the catalytical power of ceria, this work is proposed to study the process of doping ceria with zirconia and evaluate the impact on the catalysis of PROX-CO reaction for this ceria-zirconia support.

It has been shown that OSC values reach its highest when zirconia content is close to 40%. Larger ZrO_2 contents lead to a decrease of cerium ions concentration in the lattice, decreasing the capacity of the system to accomplish oxygen atoms exchange as well, which will further discussed in Section 4.5 as an important feature for the mechanism of PROX-CO reaction. It has also been revealed that for ceria-zirconia solutions, the larger the zirconia content the higher the surface area up to 20%. For higher contents of zirconia, there is a decrease in the specific surface of the material. [94]

In order to find a compromise so that the material would present a good specific surface for the deposition of Au nanoparticles and still maintain high values of oxygen storage capacity, the content of 15% of zirconia has been chosen as the one to be studied as the ceria-zirconia solution in this work. The methodology to synthesize it was properly adapted from the one proposed by Suda et al. [94]

2. OBJECTIVES

Main Objective

Develop an efficient catalyst for PROX-CO reaction based on CeO_2 nanorods decorated with gold nanoparticles.

Specific Objectives

- Exploit a method to synthesize porous CeO_2 nanorods with high yield to the desired morphology, and afterwards, employ a novel method to expand the porous structure.

- Evaluate how modification on the porous structure can affect the catalytical performance of the material.

- Study how doping CeO_2 with another transition metal, such as zirconium, can lead to catalytical modifications.

- Probe how different Au NP's deposition methods can lead to different behaviors in PrOx-CO reaction.

3. EXPERIMENTAL PROCEDURES

For all procedures, ultra-pure deionized water milli-Q (18.2 MΩ.cm resistivity at 25 °C) was used. The complete list of reagents can be found in Table 4. All chemicals were of analytical grade and used as received without further purification.

Table 4. List of chemicals used in this work and their specifications.

Chemical	Formula	Manufacturer	Purity / Concentration
Cerium(III) nitrate hexahydrate	$Ce(NO_3)_3 \cdot 6H_2O$	Sigma-Aldrich	99%
Zirconium(IV) oxynitrate hexahydrate	$ZrO(NO_3)_2 \cdot 6H_2O$	Sigma-Aldrich	99%
Sodium hydroxide	NaOH	Sigma-Aldrich	>98 %
Ethanol	C_2H_5OH	Anidrol	99.5%
Sodium chloride	NaCl	Sigma-Aldrich	> 99.5%
Sulphuric acid	H_2SO_4	Synth	96%
Nitric acid	HNO_3	Merck	65%
Hydrochloric acid	HCl	Synth	36.5%
Hydrofluoric acid	HF	Merck	48%
Orthoboric acid	H_3BO_3	Labkem	99.5%
Hydrogen peroxide	H_2O_2	Synth	30%
Tetrachloroauric(III) acid trihydrate	$HAuCl_4 \cdot 3H_2O$	Sigma-Aldrich	99.9%
Urea	$(NH_2)_2CO$	Sigma-Aldrich	99%
Oxygen diluted in nitrogen (synthetic air)	O_2	White Martins	20%
Hydrogen diluted in argon	H_2	White Martins	5%
Carbon monoxide diluted in helium	CO	White Martins	10%

3.1 - CeO_2 nanorods synthesis

This methodology approach was adapted from Mai et al. [92] 35 mL of a 6.85 mol L^{-1} NaOH aqueous solution is mixed slowly and under stirring to 5 mL of a 0.4 mol L^{-1} solution of $Ce(NO_3)_3 \cdot 6H_2O$. The resulting solution is left under stirring for 30 min, while a grey-purplish precipitate is formed. Afterwards, the whole content is transferred to a Teflon cup, which is eventually sealed inside a steel autoclave vessel and set inside an oven at 100°C for 24 h. Afterwards, reaction products, which consist of a fine grey-purplish solid are washed thrice with water and thrice with absolute ethanol and dried in oven at 60 °C during 12 h. Finally, the solid is taken to a crucible to be calcined at 600 °C for 2 h, with heating ramp set at 5°C min^{-1} and synthetic air flux at 150 mL min^{-1}. This sample was designated ***NRCeO₂.***

3.2 - CeO_2 nanorods acid leaching in H_2SO_4

200 mg of NRCeO₂ *were added to 10 mL of a* 0.5 mol L^{-1} aqueous solution of H_2SO_4 and stirred for 15 seconds. Afterwards, samples were washed thrice with water, using centrifugation in each step for removing supernatant solution and dried at 60 °C for 12 h. This sample was designated ***LNRCeO₂.***

3.3 - $Ce_xZr_{1-x}O_2$ nanorods synthesis (x = 0.15; 0.20; 0.40)

As previously described, the content of zirconium doping in ceria influences several characteristics of the resulting material, such as surface area and oxygen storage capacity, which, in consequence, influence the catalytical properties of the material as support. Three concentrations were chosen of ZrO_2 doping: 15, 20 and 40% as they encompass a range where the OSC of the materials should increase the higher the concentration of zirconia doping.

$Ce_xZr_{1-x}O_2$ nanorods are synthesized by the technique of *co-precipitation*. 35 mL of a 6.85 mol L^{-1} NaOH solution is mixed slowly and under stirring to 5 mL of a solution of $Ce(NO_3)_3 \cdot 6H_2O$ and $ZrO(NO_3)_2 \cdot 6H_2O$ in the correct proportion to synthesize $Ce_xZr_{1-x}O_2$ according to x. The sum of the concentration of both salts must equal 0.4 mol L^{-1} as in the previous procedure. The remaining parts of the procedure are the same as for the synthesis of $NRCeO_2$, including the lixiviation step

with sulfuric acid. The samples obtained by this method are named ***NRCe$_x$Zr$_{1-x}$O$_2$***, if non-lixiviated, and ***LNRCe$_x$Zr$_{1-x}$O$_2$,*** if lixiviated.

3.4 - Decoration with Au nanoparticles via synthesis by deposition-precipitation

Two methods to deposit Au nanoparticles were employed.

1) 200 mg of nanorods samples were dispersed* (see note below) in 5 mL of deionized water under strong stirring for 1 h. Meanwhile, in another flask, $8 \cdot 10^{-5}$ mol $HAuCl_4$ were added to 95 mL of deionized water. To this solution, 0.2 mol L^{-1} NaOH was poured dropwise until the pH reached 9. Then, the initial dispersion of ceria nanorods was mixed with this solution. The final solution was left under stirring for 2 hours, while the solution acquires a grey-purplish coloration as the reaction proceeds. Subsequently, the grey solid was washed 6 times with warm water and dried at 80 °C during 12 h. By the end of this step, a purple solid was calcined at 300 °C for 2 h under static air atmosphere with a 5 °C min^{-1} heating ramp.

2) 200 mg of nanorods samples were dispersed in 5 mL of deionized water under strong stirring for 1 h. Meanwhile, in another flask, $8 \cdot 10^{-5}$ mol $HAuCl_4$ and 2.523 g of urea was added to 95 mL of deionized water. Then, the initial dispersion of ceria nanorods was mixed with this solution and the final mixture is heated at 90 °C for 4 hours. The remaining steps are the same as in the other preparation procedure.

Independently of the initial sample of nanorods used for the deposition of the gold nanoparticles, the sample ($NRCeO_2$, $LNRCeO_2$, etc.), an addition of the notation **"/Au" indicates that gold nanoparticles have been anchored to the system.*

3.5 - N_2 Physisorption Isotherm Determination at 77 K

Physisorption isotherms were measured in a Micromeritics Quantachrome ASAP 2020, at the Laboratory of Solid State Chemistry, IQ-UNICAMP, coordinated by Dr. Oswaldo Luiz Alves. Samples were first degassed at 80 °C for 12 h to driven off contaminants. Afterwards, samples were put in a liquid nitrogen bath, while nitrogen gas was used as probe gas and injected into the samples up to the saturation point. Brunauer-Emmet-Teller (BET) and Barret-Joyner-Halenda (BJH)

methods were used for the determination of surface area and diameter of pores respectively.

3.6 - Oxygen Storage Capacity (OSC) Measurements

Analyses for the determination of oxygen storage capacity were performed in a TA Instruments Thermogravimetric Analyser SDT Q600, also located at the Laboratory of Solid State Chemistry, IQ-UNICAMP. The gases which were used in the analyses were hydrogen diluted in argon (2.5 % H_2/ 97.5 % Ar) and oxygen diluted in nitrogen (19% O_2/ 71% N_2), both at a flow rate of 100 mL min^{-1}. The temperature of the oven was increased under a heating ramp of 5 °C min^{-1} and the samples were analysed under isothermal conditions at different plateau temperatures, 200 °C, 300 °C, 400 °C and 500 °C. Once the desired temperature was reached, the sample was left for 5 minutes in order to stabilize the temperature and then, exposed at alternate atmospheres, reducing and oxidizing, with a 15 min long exposure to each one of them. After 3 full cycles of exposure in each one of them, the sample was heated up until reaching out the next plateau temperature. The mass variation was registered throughout the whole experiment.

3.7 - Raman Spectroscopy measurements

A Raman Horiba Jobin Yvon Spectrometer, model T64000, was used with a 532 nm laser (Coherent) at 60% power. The spectral resolution was 0.58 cm^{-1} All samples analysed were in powder form, and four spectrum acquisitions were made at a time of 60s per acquisition, in the range between 200 and 1000 cm^{-1}.

3.8 - (Diffuse reflectance spectroscopy) DRS measurements

The spectra were collected from a Shimadzu UV-2450 equipment equipped with an integration sphere and 1 nm step. Barium sulfate was used as standard to set 100% reflectance. The Kubelka-Munk function, $F(R)$, was applied to reflectance (R) results to analyze the remission of each sample in the UV-Vis region, according to Equation 6. Then, the cerium oxide band gap values in the samples were determined by extrapolating the linear part of the graph of $(F(R) \cdot hv)^2$ as a function of hv in eV.

$$F\,(R) = \frac{(1-R)^2}{2R} \qquad (6)$$

3.9 - Catalytic tests

Catalytic tests were performed on the Laboratory of Catalysis, IQ-Unicamp, coordinated by Dra. Daniela Zanchet. The tests were conducted on a small-scale reactor coupled with a gas chromatograph, using a mixture of 50 mg of the sample and 150 mg of powder silica (catalyst support). Test conditions based on ideal conditions used for PROX-CO were performed using a total gas flow of 100 mL min^{-1} with the following composition: 70% H_2, 15% He, 1% CO and 1% O_2. The remaining composition are inert gases, such as nitrogen and argon, used as carried gases. The catalyst materials were tested in the temperature range from 50 °C to 350 °C, using a 2 °C min^{-1} heating ramp, performing gas chromatography analysis every 8 min. The gaseous products of the reaction were analyzed on an Agilent brand gas chromatograph 7890A equipped with a thermal conductivity detector (TCD), using helium as the carrier gas.

CO and O_2 conversions were calculated with the following expressions respectively:

$$X_{CO} = \frac{CO_{in} - CO_{out}}{CO_{in}} \cdot 100\% \qquad (7)$$

$$X_{O_2} = \frac{O_{2,in} - O_{2,out}}{O_{2,\ in}} \cdot 100\% \qquad (8)$$

3.10 - X-ray Powder Diffraction (XRD)

X-ray analyses were conducted using CuKα1 radiation (λ = 1,5418 Å) using a XRD7000 Shimadzu X-ray diffractometer available at the IQ-UNICAMP. For this equipment, continuous scan mode was employed with a 1° min^{-1} scan speed and 0.02° sampling pitch.

For the analysis of some of the materials used on this project, the instrumental set available at the XRD1 (λ = 1.034 Å) line in the Brazilian Synchrotron Light Laboratory.

3.11 - Transmission Electron Microscopy (TEM)

Samples were analyzed in the Nanotechnology National Laboratory, in a Titan Cubed Themis, on the mode HR STEM-HAADF and in a Jeol JEM-2100F Microscope, 200 kV, STEM mode, dark field with equipped with an Oxford SDD X-Max 80 mm^2 detector for Energy Dispersive X-ray Spectroscopy (EDS). The nanoparticles samples were deposited under ambient conditions on a standard 400 mesh TEM grid.

3.12 - Inductively coupled plasma atomic emission spectroscopy (ICP-OES) determinations

Quantifications were performed on a Thermo Scientific iCAP 6000 Series analysing two emission lines for each one of the target elements. For gold, lines were at λ = 267.595 nm and 242.8 nm. For cerium, λ = 520.0 nm and 418.66 nm. For zirconium, λ = 360.1 nm and 339.198 nm.

In order to quantify cerium and zirconium during the digestion procedure, 200 mg of cerium or cerium-doped samples were mixed with 10 mL of H_2SO_4 0.1 mol L^{-1} under stirring and after determined periods of time, 100 μL of the leachate were collected and diluted to 10 mL in 50 mL Corning® Centristar™ tubes where quantifications were performed. In order to correct dilution effects, after each one of 100 μL extractions, volume was corrected in order to properly evaluate Ce and Zr concentrations.

In order to quantify gold in the catalyst samples, it was necessary to digest them via a MW-assisted decomposition method. In order to do so, 50 mg of each sample were weighted and mixed with 4 mL HNO_3, 2 mL HF, 1 mL HCl and 1 mL H_2O_2 inside microwave Teflon reactors. Samples were heated in an Analítica Provecto DGT 100 Plus MW oven with the following experimental setup: 3 min - 250 W; 5 min – 500 W; 5 min – 600 W; 5 min – 700 W; 2 min – 80 W. Upon cooling down, 300 mg H_3BO_3 were added so that excess hydrofluoric acid would be totally consumed ($4HF + H_3BO_3 \rightarrow HBF_4 + 3\ H_2O$). Heating cycle was repeated on the MW oven under the same conditions. Then, solid remaining was filtered off, while the filtered solution was directly collected on 50 mL Corning® Centristar™ tubes, where dilutions and quantifications were performed.

Analyses were performed in the Group of Spectrometry, Sample Preparation and Mechanization, coordinated by Dr. Marco Aurélio Zezzi Arruda at the Chemistry Institute in Unicamp.

3.13 - Zeta (ζ) potential measurements and determination of isoelectric point (IEP)

A Malvern Instruments® Zetasizer NANO-ZS-ZEN-3600 equipment with a He-Ne laser (633 nm) in retroscattering mode (173°) was used to obtain zeta potential of the particles. 0.1% (m/m) dispersions of nanorods samples were prepared in order to fill 1 mL polycarbonate cuvettes DTS1070 (Malvern Instruments ®) in order to provide reliable data.

In order to study the behavior of the synthesized nanoparticles in function of the medium pH and determine the IEP of the particles, colloidal sols of 0.1% (m/m) of nanorods were prepared in 0.1 mol L^{-1} solutions of NaCl. In order to determine the isoelectric point of the material, a Malvern Instruments® MPT-2 Titrator titration automated module coupled with the Zetasizer equipment. Titrating solutions used in this work was HCl (0,2 mol L-1) and NaOH (0,2 mol L^{-1}), and the automated system was programmed to add titrating solutions so that pH variation would be around 0.5 units per addition for the thorough scanning. For each addition, ζ-potential values were determined. Measurements were made in triplicate for reproducibility purposes.

4. RESULTS AND DISCUSSION

4.1 Synthesis and characterization of CeO_2-NR

Different from many of the procedures commonly found in the literature for the synthesis, the synthesis employed in this work is totally template-free, not making use of surfactants. These characteristics led to the formation of nitrogen or sulfur-based contaminant species such as nitrate or sulfate ions adsorbed on the surface of the nanorods after the calcination steps.[95] This might have had an impact on the catalytic performance of these materials, as these ions frequently act as poison and reduce the catalytic power. [96-98]

Mai et al [92] accomplished a thorough study on the different experimental parameters involved in the synthesis of CeO_2 nanoparticles of different morphologies. They concluded that CeO_2 nanoparticles synthesized via the experimental procedure used in this project is formed via a mechanism that involves multiples steps, as it is depicted in Figure 9. First of all, Ce(III) aqueous ions react with hydroxide ions leading to the formation of cerium (III) hydroxide. This compound, which was characterized to have a hexagonal crystal structure by XRD, is subsequently converted in nanooctahedra NP's. This is the privileged structure formed at first because low-energy crystallographic planes (111) are at evidence in this morphology. Previous DFT studies reveal that the low-index (111) surface has the lowest surface energy and, therefore, is the most stable surface, coming to the (110) surface, and then to high-energy surfaces of (100), (210), and (310), as depicted in Figure 10. [92]

Afterwards, this nanooctahedron structure goes through a process of dissolution/recrystallization, in which OH^- ions react with the ceria at the (111) planes, leading to a modification of the structure of the particle. This modification exposes the (100) and (110) planes and allows the particle to grow anisotropically in the (100) planes direction. This is optimized at the temperature of 100°C and [NaOH] = 6 mol L^{-1}, conditions used in this project. Mai noticed as well, that if the temperature was even further raised, e.g., up to 180°C, the nanorods structure would be destroyed leading entirely to the formation of nanocubes. [92]

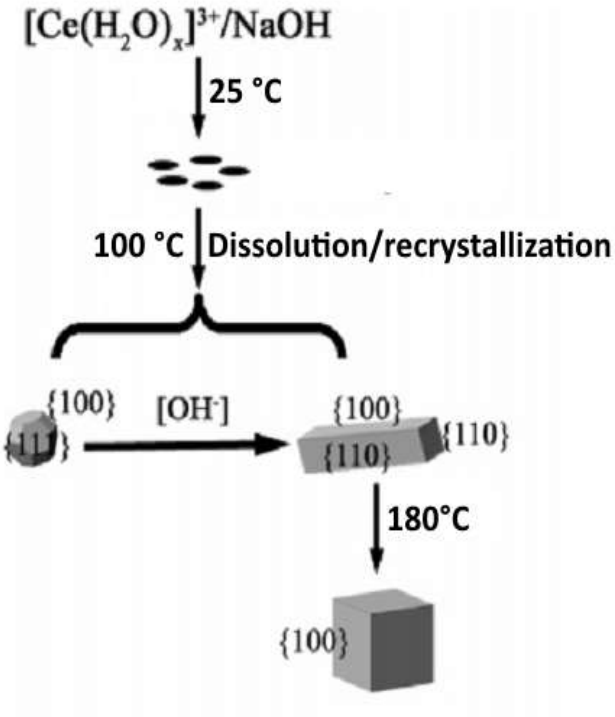

Figure 9. Scheme with mechanism for the shape-selective synthesis of CeO_2 nanorods. Adapted from [92].

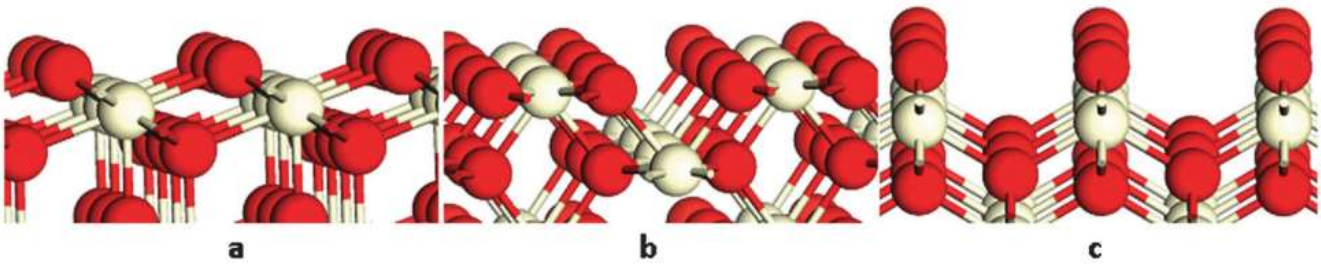

Figure 10. Side view bulk truncated structures of CeO_2 different exposed surface facets (a) (111), (b) (110) and (c) (100). Oxygen ions are assigned as red spheres, while cerium ions as white spheres. Image adapted from [99].

When Mai et al. [92] employed the exact same procedure as the one used in this work, keeping all experimental parameters, but altering cerium precursor to ammonium cerium(IV) sulfate, $(NH_4)_4Ce(SO_4)_4$, nanorods were not obtained, but large chunky aggregated nanoparticles with undefined morphology. This is justified by the fact that cerium starts off the reaction already in (IV) state, not leading to the formation of hexagonal nuclei of $Ce(OH)_3$.[92]

HRTEM images in Figure 11 of CeO_2-NR's synthesized in this work have shown that nuclei of these nanoparticles indeed have the tendency of growing

anisotropically leading to the formation of nanorods with enclosing (110) and (100) facets. [100] It was possible to see diffraction fringes associated with (002) planes and interplane distance was estimated around 0.27 nm.

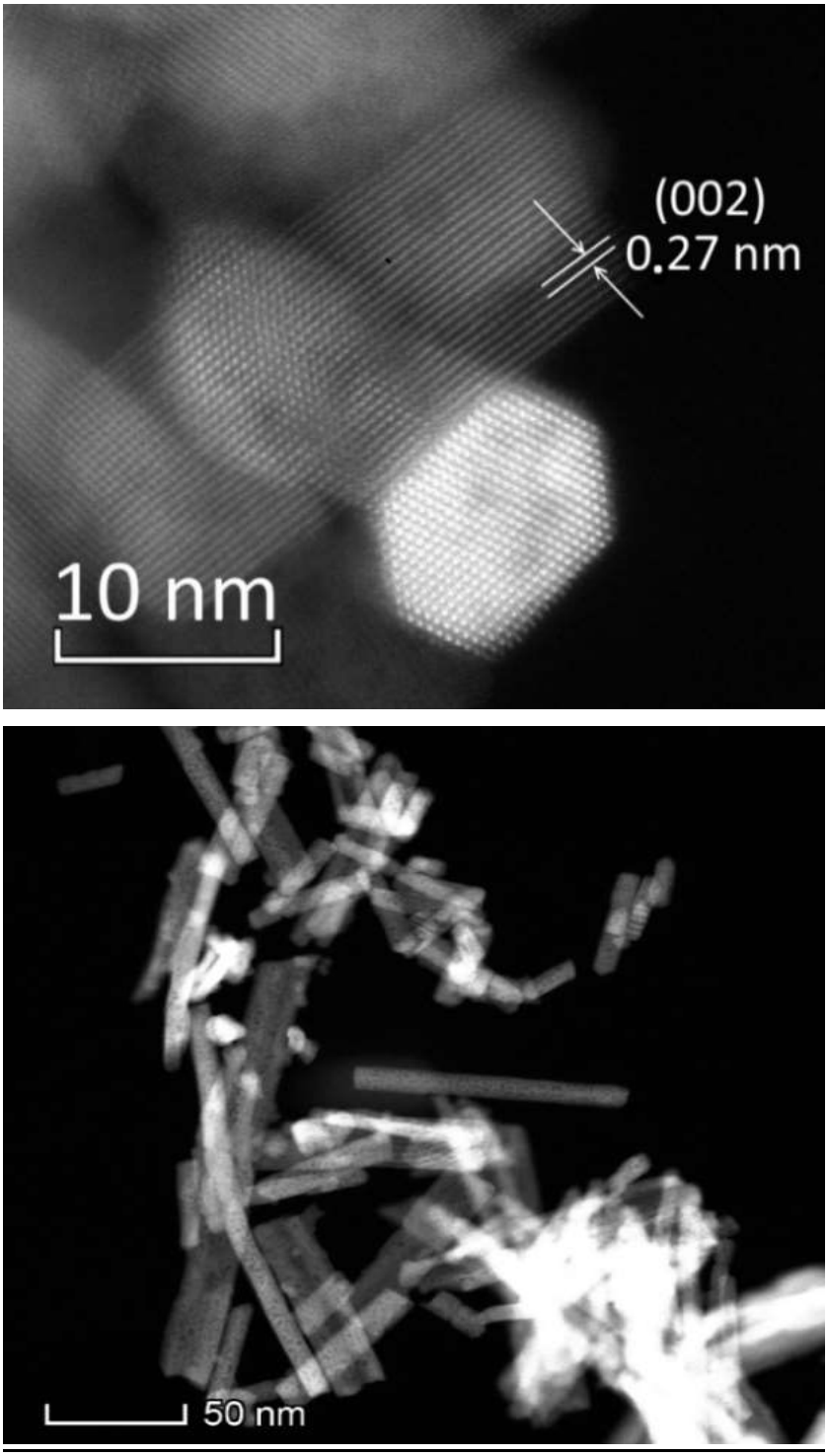

Figure 11. HRTEM images for nanorods before lixiviation for different degrees of magnification.

Additionally, it was possible to see from a cross-sectional image that the habit of CeO_2 crystals was hexagonal, even though its crystalline structure is cubic fluorite-type. This might be a consequence of the formation of hexagonal nuclei of $Ce(OH)_3$. [92]

HRTEM images also reveal that these nanorods present some native pores, which can be seen as lighter parts in the images. The characteristic of formation of these porous structures also seems to be intrinsically intertwined to the formation of precursors composed of CeO_2 and $Ce(OH)_3$ after partial oxidation of $Ce(OH)_3$ nuclei.[101] The dehydration process of cerium (III) hydroxide leads to the formation of cerium (III) oxide and water. Thereupon, cerium (III) oxide is subsequently oxidized to cerium (IV) oxide, not entirely as this compound always keeps a non-stoichiometric character. The chemical reactions that describe these processes are:

$$2\,Ce(OH)_3 \rightarrow Ce_2O_3 + 3\,H_2O \quad (9)$$

$$2\,Ce_2O_3 + O_2 \rightarrow 4\,CeO_2 \quad (10)$$

Wu et al tracked down throughout time by HRTEM-FFT-treated images the modification of crystallinity associated with the formation of mesopores in FeOOH nanorods. [102] Such mesopores seem to be formed from the release of water molecules that remain occluded inside the nanorods during the crystallization process, and upon heating, through an interinfiltration process, they leave some cavities behind and create a nanoarchitecture based on native pores.

For similar synthetical experimental conditions as the ones used in this work, but in which there was excess oxygen, Li et al observed that the formation of $Ce(OH)_3$ was decreased, assisting instead the direct formation of cerium (IV) oxide. [101] In this context, nanorods were also formed, but in lieu of the porous one, massive rods with no pores at all were produced. This is depicted in Figure 12, which schematizes the formation of the porous nanorods structure.

Such non-porous ceria nanorods not only feature a lower surface area than the porous ones, but also lower OSC values and, according to XPS studies, a lower proportion of Ce ions in the +3 oxidation state, which are directly linked to the formation of oxygen vacancies in the crystalline structure of the ceria. While in non-porous samples, the proportion of Ce^{3+} in porous samples is around 15%, this value exceeds 25% in porous samples. [101]

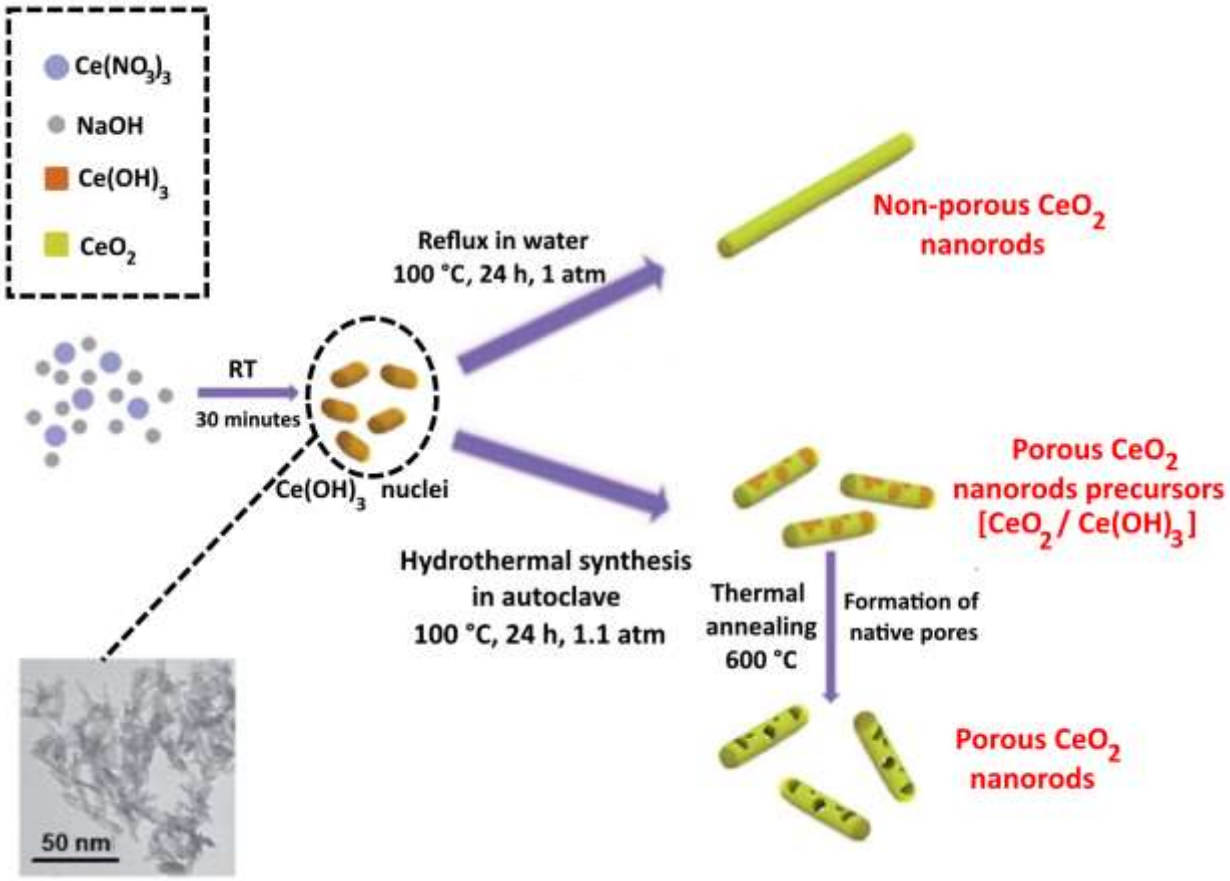

Figure 12. Schematic of the synthesis of porous and non-porous CeO_2 nanorods. Porous CeO_2 nanorods are prepared by the dehydration of $Ce(OH)_3$, liberating occluded water molecules from the inside of the nanorods, followed by oxidation of Ce(III) to Ce (IV). Non-porous nanorods under conditions that oxidizes $Ce(OH)_3$ directly to CeO_2, such as refluxing in excess of atmospheric oxygen. Image adapted from [103].

Altogether, everything seems to point out to the correlation that the intermediate formation of cerium hydroxide (III) in the formation of this native pore structure is intrinsically associated with the amount of $V_O^{\cdot\cdot}$ in ceria structure. Therefore, the subsequent applications of CeO_2 that rely on the presence of these structural defects, such as the catalysis of reactions as WGS and PROX-CO are dependent on how structurally organized these nanorods are. This is why a lot of effort has been devoted into controlling the concentrations of surface Ce^{3+} and oxygen vacancies for different applications. [103-106]

4.2 - Leaching Procedure

In order to evaluate the topological effects in the crystal structure of the ceria nanorods caused by the acid leaching procedure developed in this work, transmission electronic microscopy was used to obtain images of **NR*CeO₂*** and **LNR*CeO₂*** so that they could be compared in order to evaluate changes. Images reveal that there was a mean enlargement of the pores close to 2 nm after counting 150 pores in each one of the samples.

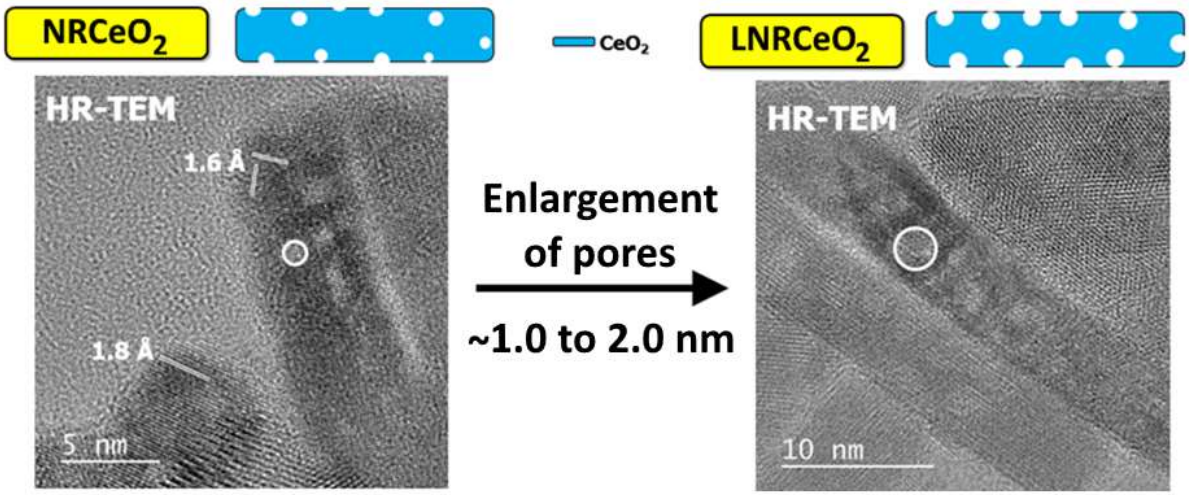

Figure 13. HRTEM images of NRCeO₂-NR and LNRCeO₂-NR, showing in evidence the expansion of native pores of CeO₂-NR after treatment with a solution of 0.5 mol L⁻¹ H₂SO₄.

Um et al performed a study about ceria solubility in different concentrations of sulfuric acid and different temperatures and found out that the dissolution of the material, although slow, can be achieved thoroughly after several minutes of exposition to the acid solution. [107] Beaudoux et al performed studies based on UV-VIS spectroscopy and found out that, although ceria exhibits slow dissolution in solutions of inorganic acids, ceria dissolution rate is dramatically increased in solutions of these acids in the presence of ascorbic acid. [108] Ascorbic acid, a well-known potent antioxidant compound (therefore, a reducing chemical species), was proposed to take part in a prior adsorption on ceria surface leading reduction of Ce (IV) to Ce (III) ions. This would reduce the crystalline lattice stability energy, U,

according to the Born-Landé equation, and allow for cerium ions to be subsequently dissolved by the inorganic acid. [109-110]

It was observed empirically during the nanorods leaching procedure with H_2SO_4 solution that, as soon as the solid material gets in contact with the acid solution, the liquid effervescences. The gas released in this step is confirmed to be O_2 making a simple test: by approaching a lit match of the solution, the glow of the flame becomes more intense, implying it is indeed oxygen gas.

Thus, the process should be implicated at first to the oxidation of water molecules on the surface of CeO_2 nanorods leading to the formation of O_2 and, at the same time, the reduction of Ce (IV) to Ce (III). Afterwards, sulfuric acid molecules take the role into lixiviating *de facto* Ce (III) ions to the solution breaking Ce–O and prompting the formation of cerium (III) sulfate and water. The proposed balanced chemical equation for this process is:

$$4\,CeO_{2\,(s)} + 6\,H_2SO_{4\,(aq)} \rightarrow Ce_2(SO_4)_{3\,(aq)} + 6\,H_2O_{(l)} + O_{2\,(g)} \quad (11)$$

H_2SO_4 was chosen as leaching agent in this project, as HNO_3 and HCl were barely able to dissolve ceria, even on concentrated solutions. Although thermodynamically spontaneous, the reaction between H_2SO_4, and ceria takes place quite slowly. Kinetics curves obtained by ICP measurements depicted in Figure 14 illustrate this behavior.

For $NRCe_{0.8}Zr_{0.2}O_2$, the rate of dissolution was a little bit higher than for $NRCeO_2$ even though its surface area was lower than the one reported for $NRCeO_2$, but despite of this, after 320 minutes of exposition to 0.1 mol L^{-1} H_2SO_4, total amount of cerium dissolved into solution did not surpass 2 %. As it will further be discussed in the next sections, enthalpy of dissociation of an oxygen atom from the surface of $NRCe_{0.8}Zr_{0.2}O_2$ is lower than in $NRCeO_2$, as empirically confirmed by OSC measurements. The more favorable it is to extract oxygen ions, the easier cerium ions are dissolved from the lattice into the solution.

N_2 physisorption isotherms depicted in Figure 15 show that acid leaching treatment increased native pore size in about 45%, increasing from 7.9 nm in $NRCeO_2$ to 11.5 nm in $LNRCeO_2$, which confirms the results from HRTEM images in Figure 16. Data is summarized in Table 5.

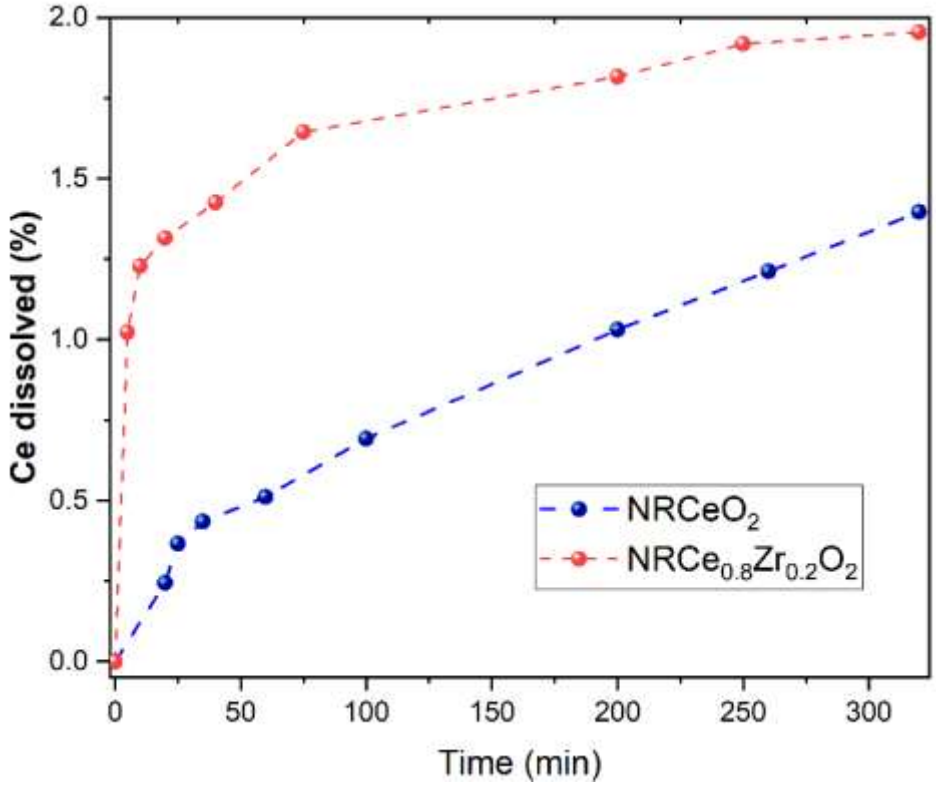

Figure 14. Dissolution kinetic curves related to the dissolution of 200 mg of (1) $NRCeO_2$ (250 m^2 g^{-1}) and (2) $NRCe_{0.8}Zr_{0.2}O_2$ (250 m^2 g^{-1}) in 10 mL H_2SO_4 0.5 mol L^{-1} under magnetic stirring.

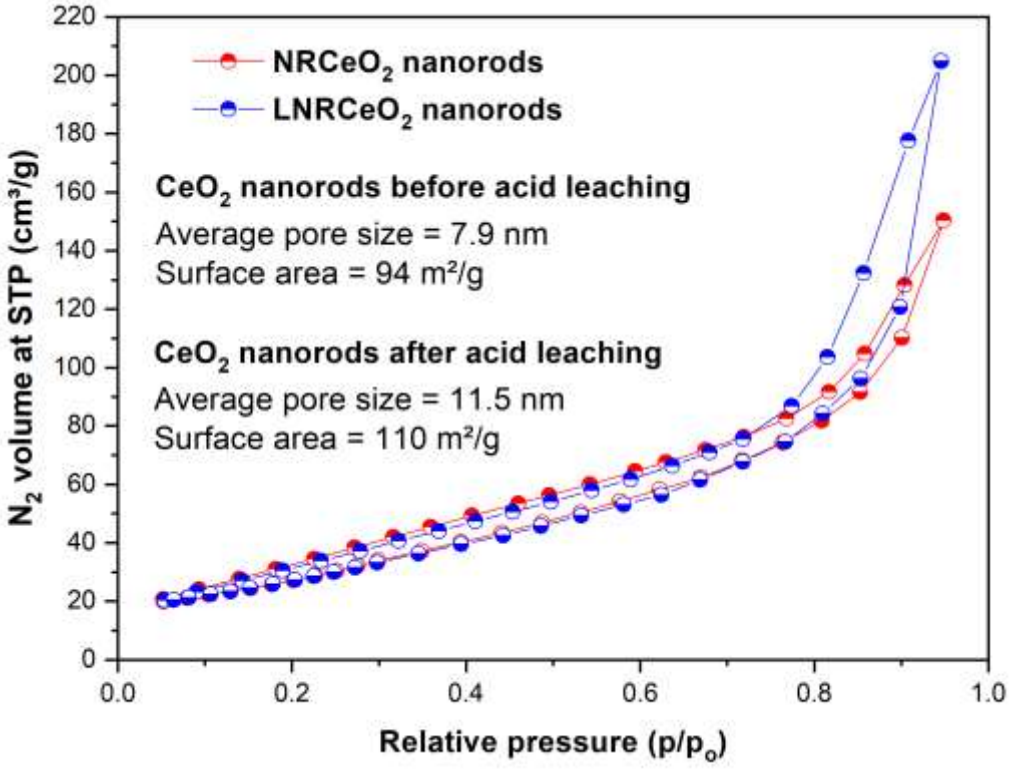

Figure 15. N_2 Physisorption isotherms for $NRCeO_2$ and $LNRCeO_2$ obtained at 77 K.

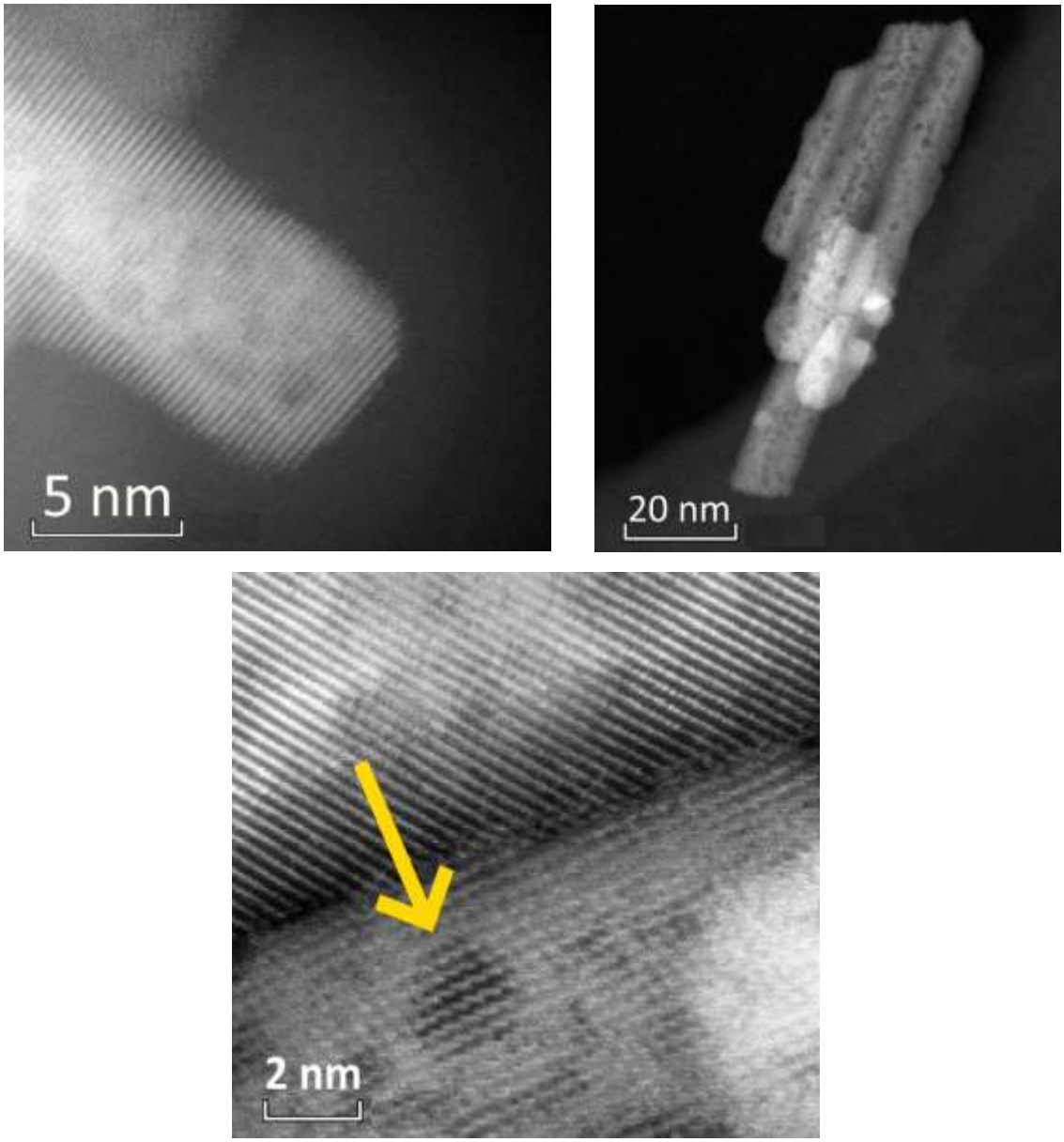

Figure 16. HAADF HRTEM images for: a) $NRCeO_2$, i.e. ceria nanorods prior to H_2SO_4 lixiviating process; b) and c) $LNRCeO_2$, i.e. ceria nanorods after H_2SO_4 lixiviating process. Dark holes highlighted in the middle of the nanorods are ceria native pores.

Table 5. Texture properties for different modified samples based on CeO_2 nanorods: CeO_2-NR; $LNRCeO_2$ and $LNRCeO_2$/Au.

Sample	Surface area BET (S_{BET})($m^2\ g^{-1}$)	Pore mean diameter (D_p)(nm)
$NRCeO_2$	94	7.9
$LNRCeO_2$-NR	110	11.5
$LNRCeO_2$/Au	111	11.3

Surface area has also seen an increment: 94 m^2/g for $NRCeO_2$, while this value increased to 110 m^2/g for $LNRCeO_2$. Isotherms from both samples exhibited behavior of type IV isotherms with H3 hysteresis loops according to the IUPAC classification, typical of mesoporous materials (pore size between 2 and 50 nm). The main features of these types of isotherms are the line referring to the adsorbed quantity of gas on the surface of the nanorods which slowly increases for low values of relative pressure (P/P_o), while it takes a sharp increase for high values of P/P_o. This indicates the formation of mesopores which are built by stacking of the nanorods. There is also a hysteresis loop, which is associated with capillary condensation taking place inside the mesopores. [111]

4.3 - Synthesis and characterization of $Ce_xZr_{1-x}O_2$ nanorods

So far, literature reports that tetravalent ions, such as Zr^{4+}, Hf^{4+}, Tb^{4+}, Ti^{4+}, etc. are the best dopants for ceria, not only because they are able to improve thermal stability, but also improve CeO_2 OSC (which will be further discussed in Section 4.5), due to their ability to form homogeneous solution due to the equality of charges with cerium (IV). **[112-113]** Part of the increase of the catalytic power of the material can be rationalized with the scheme found in Figure 17.

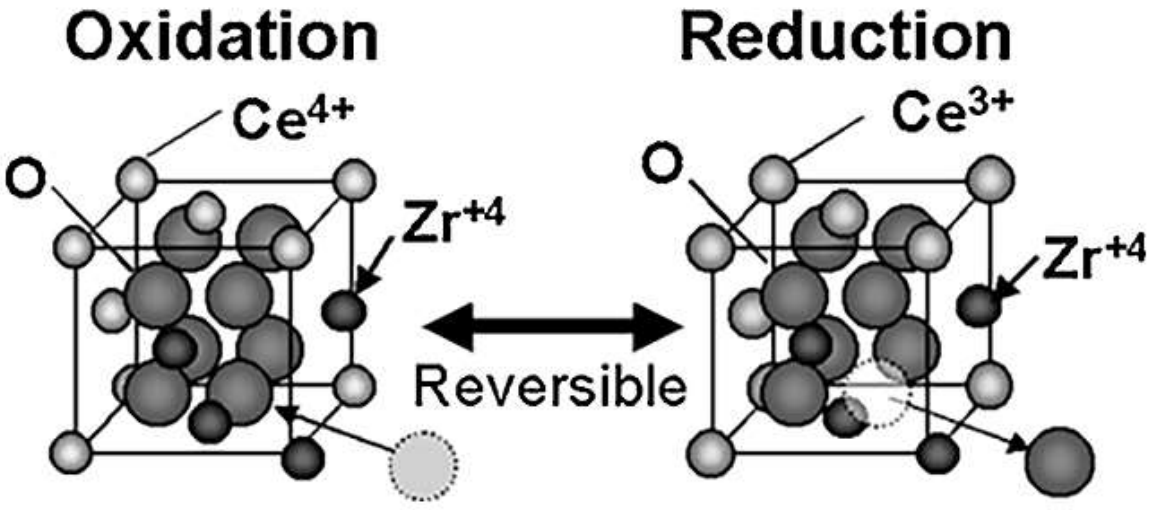

Figure 17. Schematic structures of CeO_2-ZrO_2 solid-solution indicating oxidation and reduction. Image adapted from [112].

During the oxygen release in the doped material, the volume of Ce increases when the Ce oxidation state changes from Ce(IV) to Ce(III). The stress energy

arising from this volume increment would restrict further valence change of Ce. Since the effective ionic radius of Zr(IV) is smaller than that of Ce(IV) and Ce(III), the introduction of Zr into a Ce framework on a homogeneous level would compensate for the volume increase related to Ce(IV) reduction.

This modification of the local oxygen environment around Ce and Zr will generate some active oxygen species that will play a role in OSC improvement. Meanwhile, when smaller Zr cations substitute larger Ce ions, the bond distance between oxygen and metal ion will be enlarged, thereby making oxygen more mobile. As the lattice shrinks down, there is more space for Ce^{4+} to become Ce^{3+}, improving the formation of oxygen vacancies which are of crucial importance for the catalytic properties of the material. **[114]**

Therefore, doping with Zr(IV) should lead to the reduction and a shrinkage of the cell unit volume, and as a direct consequence, cell parameter ***a***. This is confirmed by XRD shown in Figure 18 and Figure 19, specifically the peak centered around 2θ = 19.00° (for pure ceria for λ = 1.034 Å, whose data is summarized in Table 6.

Table 6. 2θ values for peak central position for the different proportions os ceria doped with Zr (IV) – $Ce_xZr_{1-x}O_2$.

Ceria – zirconia composition	(111) 2θ peak position
$NRCeZrO_2$	19.000
$NRCe_{0.85}Zr_{0.15}O_2$	19.092
$NRCe_{0.8}Zr_{0.2}O_2$	19.105
$NRCe_{0.6}Zr_{0.4}O_2$	19.169

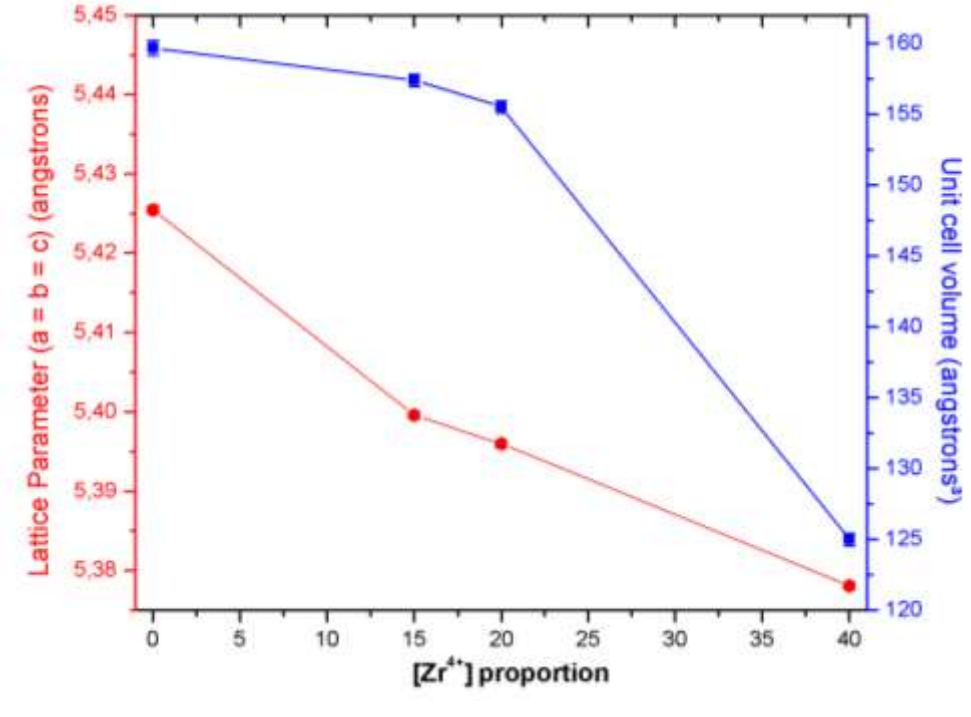

(a)

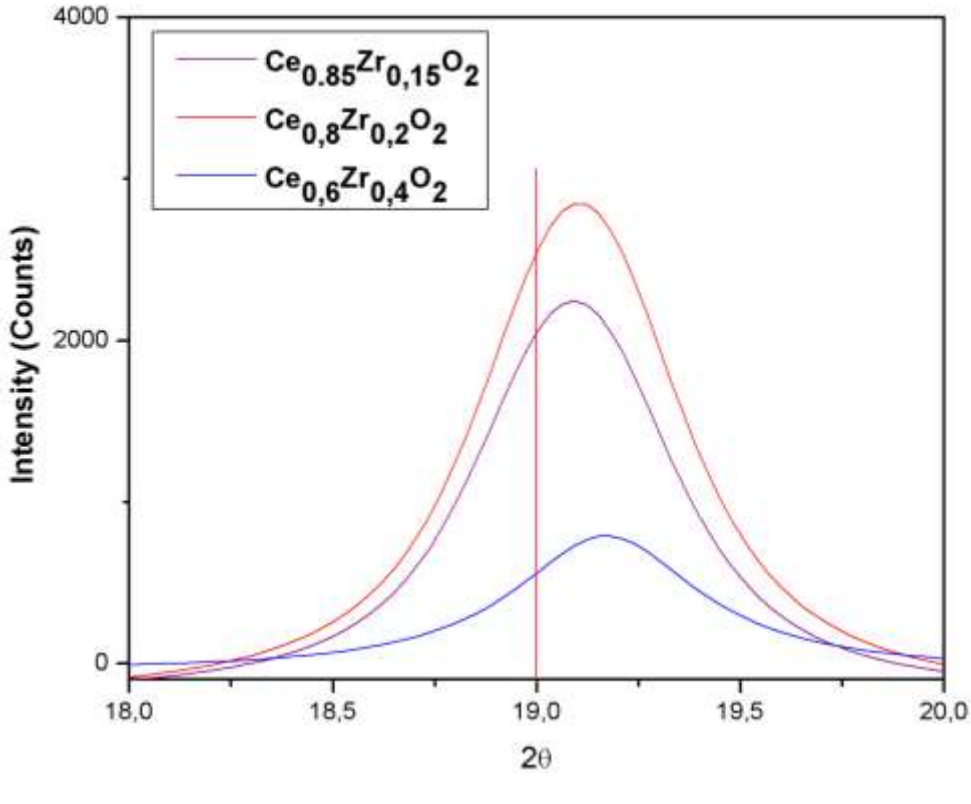

(b)

Figure 18. (a) Variation of lattice parameter a and unit cell volume in function of the Zr (IV) proportion in the doped sample. (b) XRD diffractograms performed at a beam line (λ = 1,034 Å) centered in the peak 2θ = 19.00° for cerium oxide doped with Zr (IV) in different proportions: There is a shift towards larger values of 2θ due to modifications in the crystalline structure of the material.

4.4 - Characterization of $NRCeO_2$/Au and $NRCe_{0.8}Zr_{0.2}O_2$ by XRD and HRTEM

XRD results in Figure 19(a)-(b) have shown that $NRCeO_2$ crystallizes in the CeO_2 cubic crystal structure, which is confirmed by comparison with reference data available in the literature, with slightly broader peaks due to the nanometric size.[115]

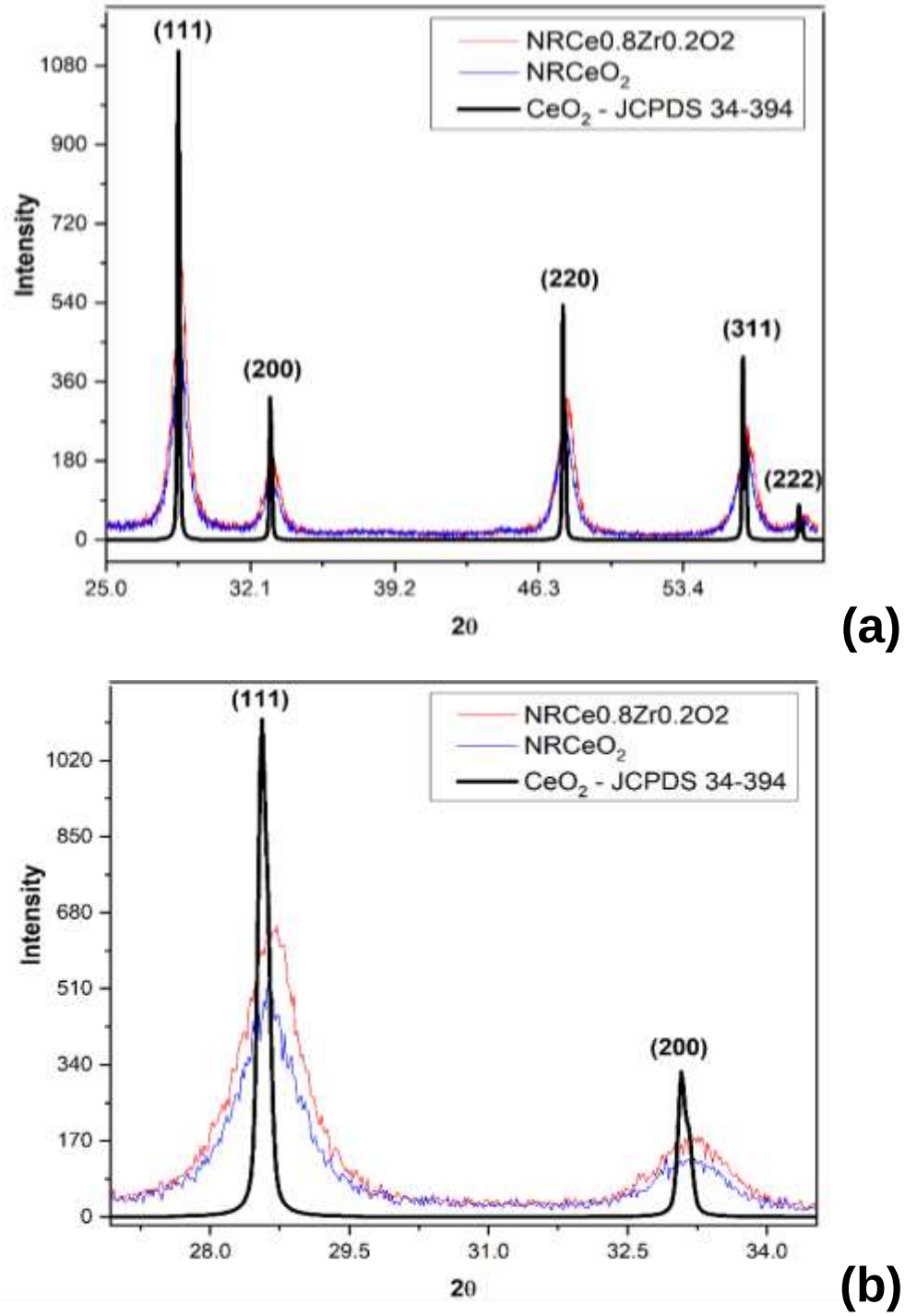

Figure 19. X-ray diffractograms of $NRCeO_2$/Au and $NRCe_{0.8}Zr_{0.2}O_2$ with different 2θ ranges: (a) from 25° to 60°; (b) from 27° to 35°.

For $NRCe_{0.8}Zr_{0.2}O_2$ sample, a small shift to larger number of 2θ is observed for all peaks compared to CeO_2 ones. This observation, together with the fact that no peak for ZrO_2 is observed leads to the conclusion that during the coprecipitation with $ZrONO_3$, Zr(IV) ions might have entered into ceria crystalline structure. As Zr(IV) is smaller than Ce(IV), (0.84 Å for Zr^{4+} and 0.97 Å for Ce^{4+}) **[116]** this results in a contraction in the lattice and a shift to larger 2θ values.

HRTEM images shown in Figure 20 reveal that the doping in the synthesis preserved the nanorod morphology, as EDS mappings showed that Zr is homogeneously dispersed throughout the rods, providing further evidence evidences that zirconium ions have been homogeneously incorporated in ceria crystal lattice, which corroborates data obtained by XRD.

Crystallite size is calculated by Scherrer Equation, presented in Equation 9, which is possible using X-ray radiation wavelength (λ), diffraction angle (θ), half-width height of one of the peaks of the sample (B_T) and of a reference (B), in radians, and a dimensionless constant K, called shape factor which depends on the actual shape of the crystallite. Used standard data for the value of B was attributed to polycrystalline silicon, for which $B = 2.1\times10^{-3}$ and K was set as equal to 0.9, which is the value for spherical-shaped crystallites. Data is summarized in Table 7.

$$\tau = \frac{K\lambda}{\sqrt{B_T^2 - B^2}\, cos\theta} \quad (12)$$

Table 7. Crystallite size for $NRCeO_2$, $LNRCeO_2$ and $NRCe_{0.8}Zr_{0.2}O_2$ calculated by Scherrer Equation

Sample	Crystallite size (nm)
$NRCeO_2$	13.7
$LNRCeO_2$	13.7
$NRCe_{0.8}Zr_{0.2}O_2$	11.5

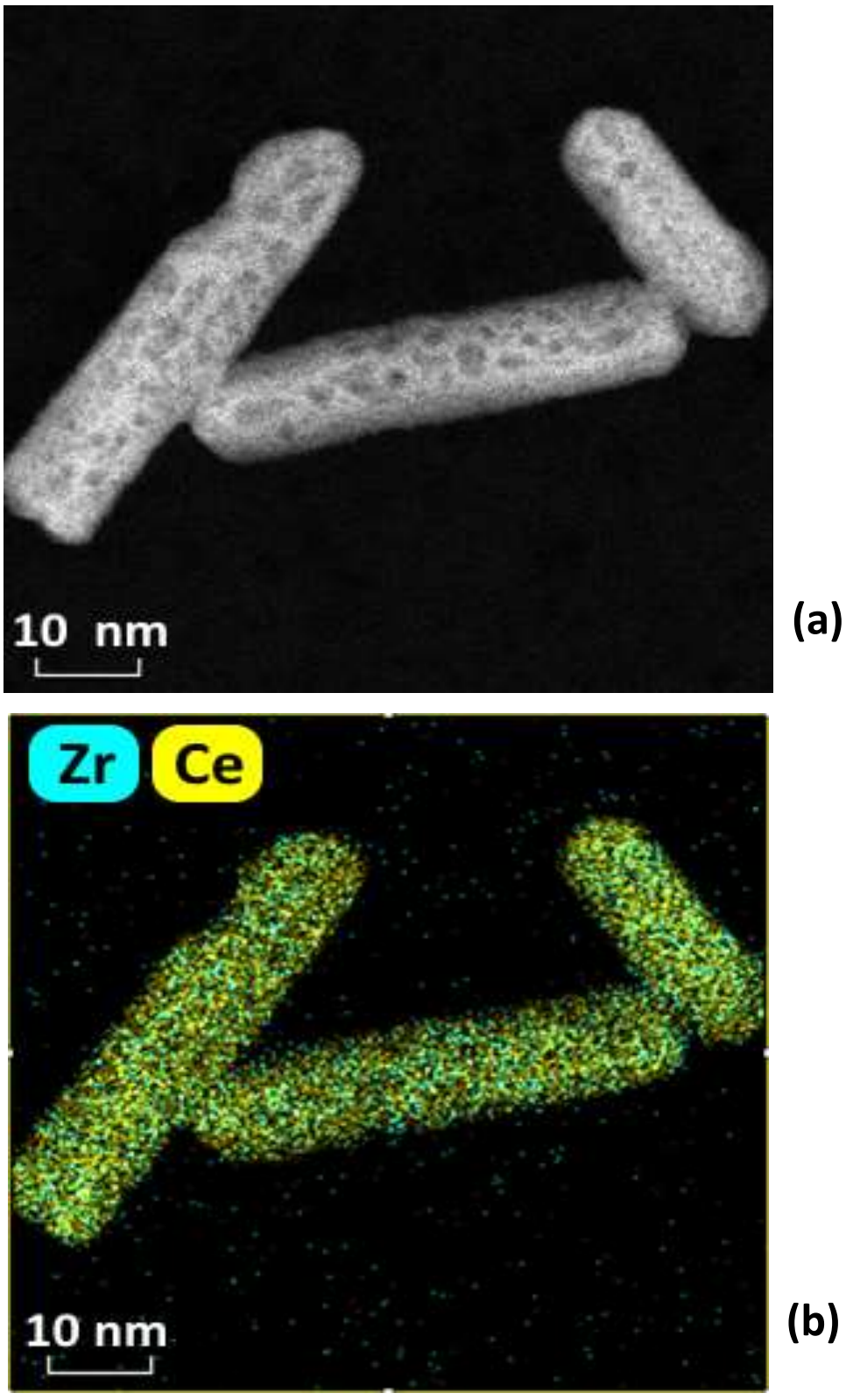

Figure 20. (a) HRTEM image for cerium oxide nanorods $Ce_{0.8}Zr_{0.2}O_2$. (b) Energy Dispersive Spectroscopy (EDS) mapping for zirconium (blue dots) and cerium (yellow dots). Mapping shows that zirconium (IV) ions are homogeneously dispersed in the whole composition of the ceria nanorod.

It is observed that the leaching procedure did not alter the crystallite size of ceria nanorods. This is probably because, although there might have been some lixiviation of the peripheral zone of the rods, most of the lixiviation took place in the native pores that were expanded not altering significantly the crystallite sizes.

However, when the nanorods synthesis was performed with zirconium doping, the crystallite size decreased from 13.7 to 11.5 nm. This might also be associated with the contraction of the fluorite-cell unit with the inclusion of smaller Zr^{4+} ions. Doping with zirconium also increases the amount of formation of Ce^{3+}, which leads to more formation of vacancies and displacements of oxygen atoms, driving to a nanorods with smaller crystallites.

Cerium-zirconium oxide with other composition, such as $Ce_{0.85}Zr_{0.15}O_2$ and $Ce_{0.60}Zr_{0.40}O_2$ have also been synthesized although they have not been used as supports due to the limitation of time of the project. Even though, HRTEM images were taken (Figure 21) and have revealed that the nanorod morphology was also produced, even keeping the structure of the native pores. This suggests that the addition of Zr ions up to 40 % in the hydrothermal conditions as proposed by Mai et al [92] still leads to hexagonal intermediates, which are subsequently converted to the nanorods. Zirconium probably precipitates together with cerium forming a mixture of cerium (III) hydroxide and zirconium (IV) hydroxide.

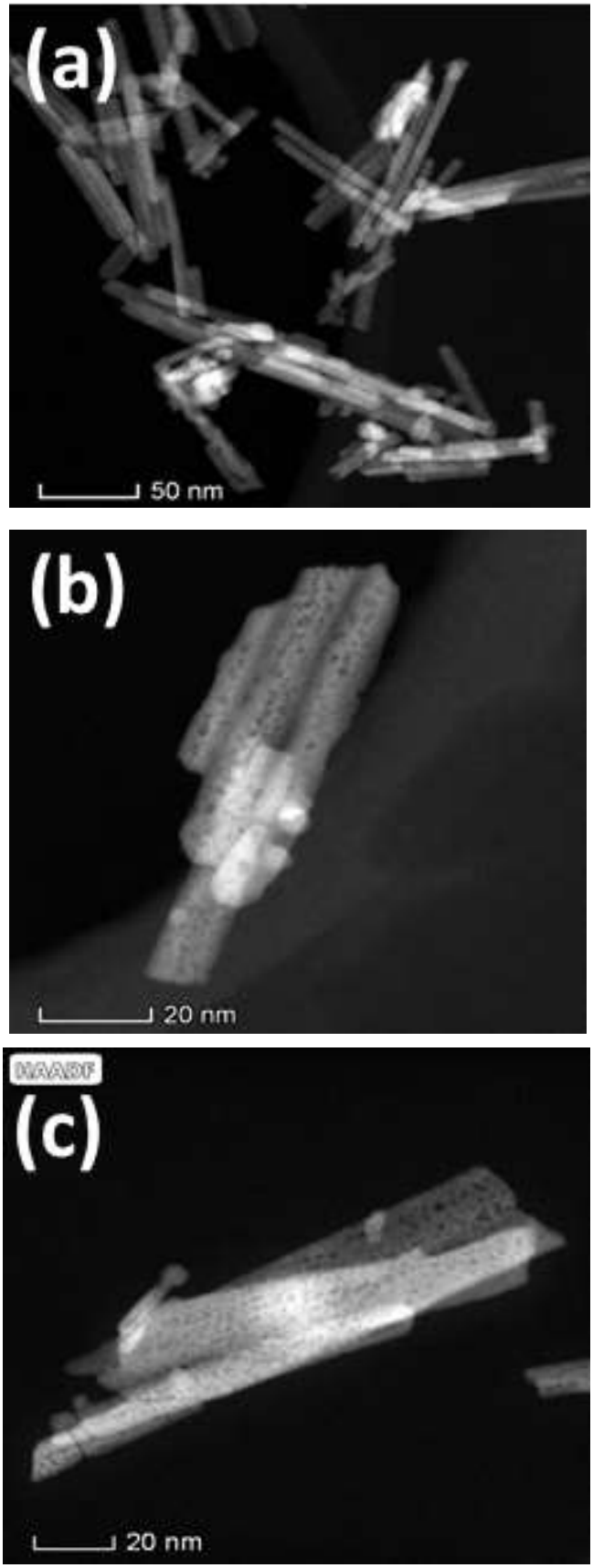

Figure 21. HRTEM images for cerium oxide nanorods doped with Zr (IV) in different proportions: (a) $Ce_{0.85}Zr_{0.15}O_2$; (b) $Ce_{0.8}Zr_{0.20}O_2$ and (c) $Ce_{0.60}Zr_{0.40}O_2$.

4.5 - Raman measurements

Raman spectroscopy is a powerful technique to analyze nanoceria structural properties at a local level, owing to the strong sensitivity of the phonon characteristics to the crystalline nature of the material, being useful to directly probe the defect sites in doped and undoped ceria particles. The samples were also analyzed by Raman spectroscopy to study how the leaching procedure altered their structural features and thus their catalytic activity. [88]

Four features can be identified in the room temperature spectra: the main Ce-O_8 crystal unit vibration around 464 cm^{-1}, which is the characteristic F_{2g} mode of the fluorite lattice, and three weaker Raman peaks at 261 cm^{-1}, 598 cm^{-1}, and 1165 cm^{-1}. The first and the third ones can be assigned to the higher order modes of ceria, namely to the second order transverse acoustic mode (2TA) and to the second overtone of the longitudinal optical band (2LO). The Raman peak at 598 cm^{-1}, named D band or Defect band, as it is instead a disorder induced mode arising from oxygen vacancies defects The relative intensity ratio of the Defect band (I_D) and the F_{2g} band (I_{F2g}) of the CeO_2 fluorite phase (i.e., I_D/I_{F2g}) can be used as an indicator of the oxygen defects density. [117]

Esmailpour and collaborators made use of Raman spectroscopy and noticed that I_D/I_{F2g} increased by 32% when ceria samples were exposed to a H_2 reducing treatment and increased even more when the sample was submitted to exposition under UV light illumination revealing that the light pre-treatment increased the oxygen vacancy concentration by 46%. [93]

A group in Japan led by Taniguchi also used Raman spectroscopy and the I_D/I_{F2g} ratio to analyze Gd-doped samples of ceria where the D band intensity became more pronounced with the increase in the dopant concentration in the range between 0 and 20%. As the oxygen vacancy concentration is correlated with the concentration of Ce(III) ions, the group regarded Raman Spectroscopy as a robust alternative to XPS and EDS measurements to estimate [Ce(III)]/[Ce(IV)] ratio. [118]

The Raman spectra for ceria nanorods prior and after lixiviation are presented in Figure 22. The spectra were normalized having set the maximum intensity of the F_{2g} band mode as 1.0 for both.

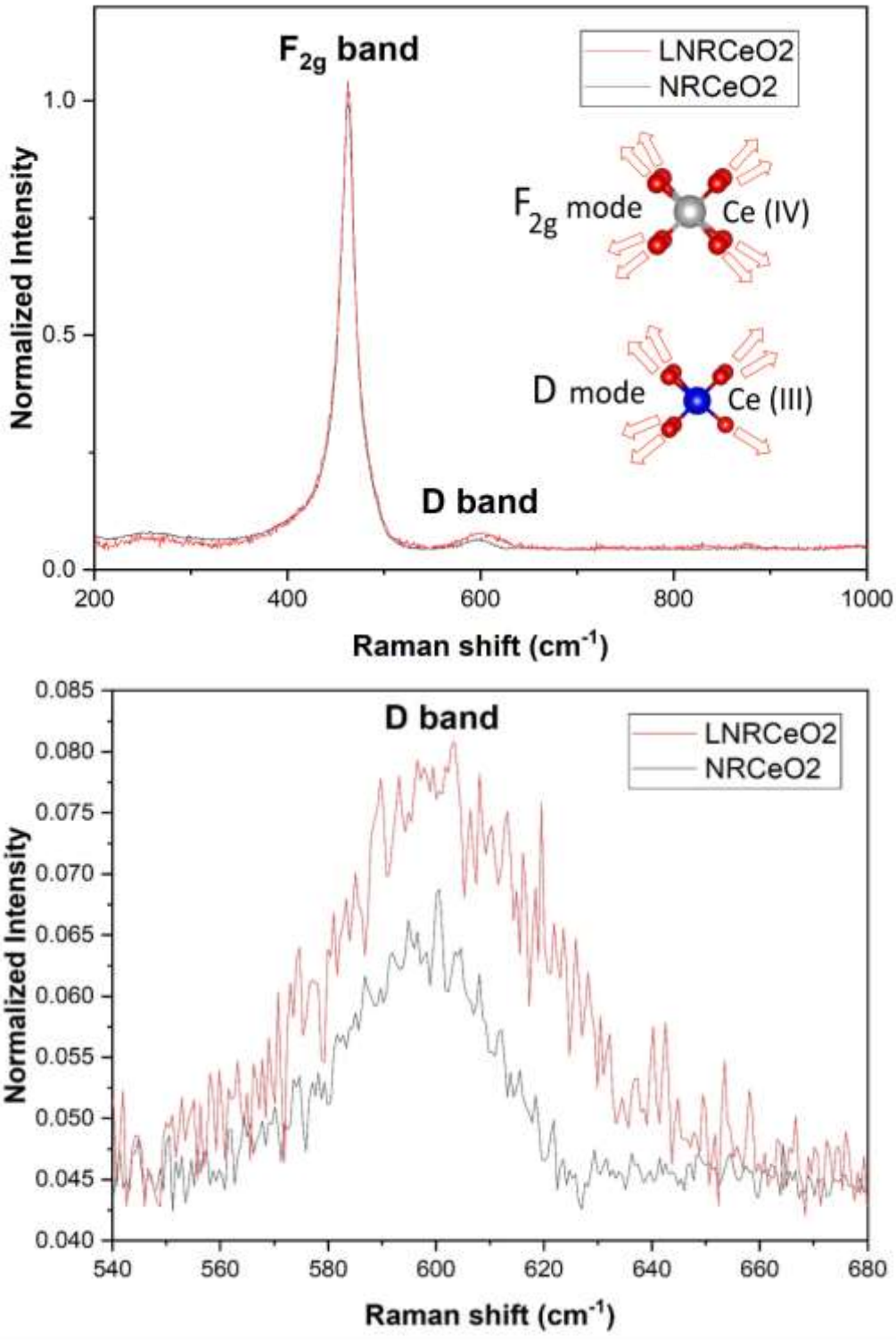

Figure 22. (a) Normalized Raman spectra for non-lixiviated ($NRCeO_2$) and lixiviated ceria nanorods ($LNRCeO_2$) highlighting the F_{2g} band mode centered at 464 $cm^{-1}$and the D mode centered at. 598 cm^{-1}. (b) Magnification of the region between the Raman shift range between 540 cm^{-1} and 680 cm^{-1} highlighting the difference in intensity for the D mode band peaks between the two samples, associated with the difference in oxygen vacancy defects.

As it is seen in Table 8 data, I_D/I_{F2g} ratio increased close to 50% when ceria nanorods were submitted to acid leaching treatment indicating that not only the pore size was expanded, but also there was in increase in the number of oxygen vacancies, which was corroborated by the catalytical tests results.

Table 8. I_D/I_{F2g} ratio for $NRCeO_2$ and $LNRCeO_2$ calculated with their Raman spectra.

Sample	I_D/I_{F2g}
$NRCeO_2$	0.24
$LNRCeO_2$	0.36

4.6 - OSC measurements

As described in the experimental section, samples were exposed to alternate atmospheres (oxidizing/reducing). The behavior is depicted on Figure 23. When the sample is heated, there is a natural weight decrease due to a shift on the equilibrium to the right:

$$CeO_2 \rightleftharpoons CeO_{2-x} + \frac{x}{2}O_2 \quad (13)$$

As the reaction is endothermic in the direct way, it is favored upon heating leading to a decrease of weight due to the loss of oxygen by the lattice, until a thermodynamical equilibrium is reached. After the equilibrium is reached, the sample is set to reach temperature plateaus. When the temperature is stabilized, alternate injections of H_2 and air (80% of N_2 and 20% of O_2) are performed. The profile on how the weight behaves is depicted on Figure 23. Injection of oxygen leads to a fast incorporation of oxygen ions into the lattice until the weight variations ceases.

Then, when hydrogen is added to the system, the mass of ceria decreases again, as $V_O^{\cdot\cdot}$ are formed again. The difference in mass between the minimum mass after the exposition to hydrogen and the threshold mass after exposition to oxygen can be used to calculate the OSC of the samples in μmol O_2 g^{-1} CeO_2 unit.

OSC measurements were performed for all the samples synthesized in this work and the results are summarized in Tables 9 and 10 and Figure 24. It is observed that OSC values for $LNRCeO_2$ samples are 3.2 times higher than the ones

for $NRCeO_2$ for each one of the four temperatures used experiments for the determination of OSC.

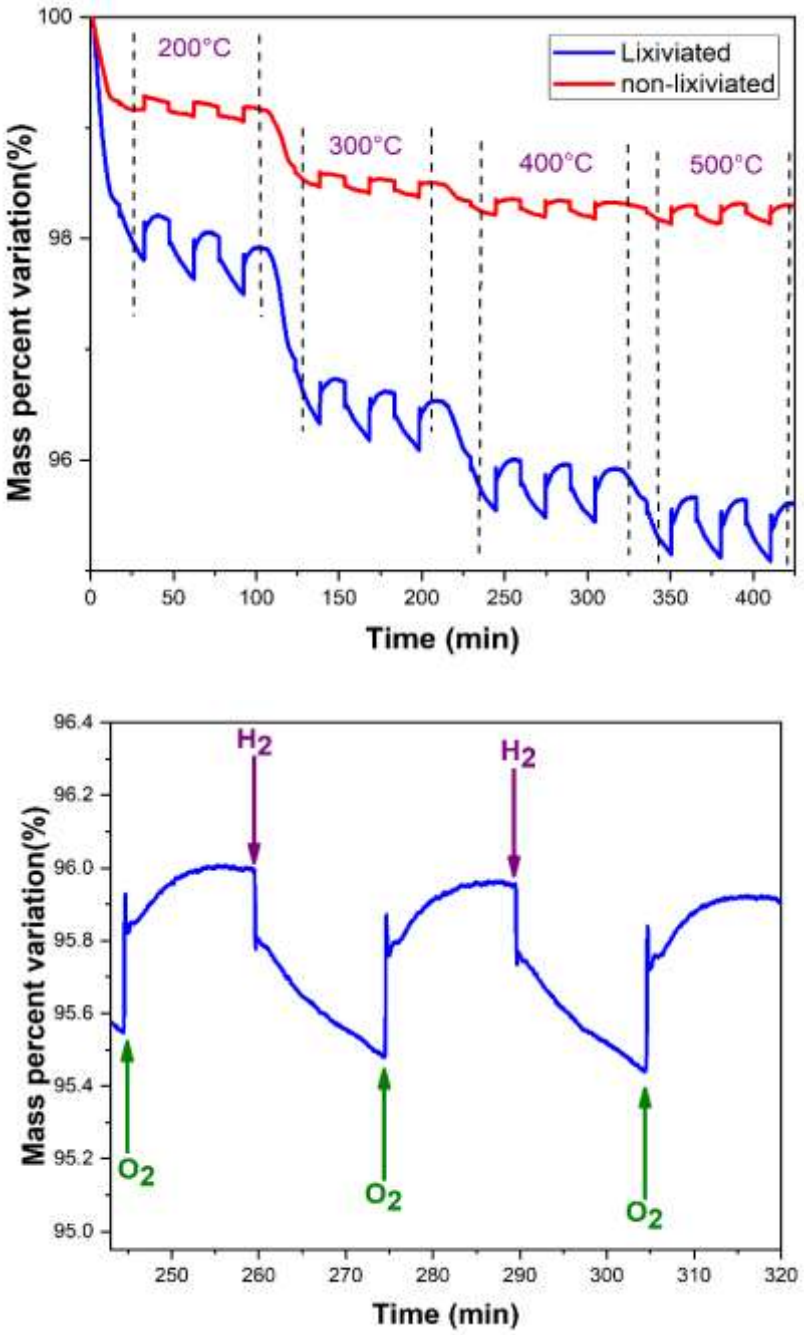

Figure 23. (a) percentual mass variation for $NRCeO_2$ and $LNRCeO_2$ highlighting the alternate exposition to oxidizing and reducing atmosphere for different temperature plateaus. (b) zoom of the cyclic mass variation for $LNRCeO_2$ at the temperature of 300 °C with emphasis at the points in which the atmosphere inlet into the system was changed.

This points out that the acid lixiviation procedures indeed increased the OSC by increasing the native pores surface area where the Ce^{3+}/Ce^{4+} ratio is higher compared to the nanorod bulk and the formation of oxygen vacancies is more energetically favourable.

Table 9. OSC values in µmol O_2 g^{-1} CeO_2 for $NRCeO_2$, $LNRCeO_2$ and $LNRCe_{0.8}Zr_{0.2}O_2$ samples at different temperatures.

	$NRCeO_2$	$LNRCeO_2$	$LNRCe_{0.8}Zr_{0.2}O_2$
200°C	162.6	534.3	598.1
300°C	163.4	547.9	514.1
400°C	188.7	604.6	492.7
500°C	206.9	666.6	487.8

Table 10. OSC values in µmol O_2 g^{-1} CeO_2 for $NRCeO_2$, $LNRCeO_2$ and $LNRCe_{0.8}Zr_{0.2}O_2$ samples at different temperatures.

	$NRCeO_2$/Au	$LNRCeO_2$/Au
200°C	342.8	1173.7
300°C	393.2	1209.3
400°C	521.2	1430.5
500°C	629.6	1796.1

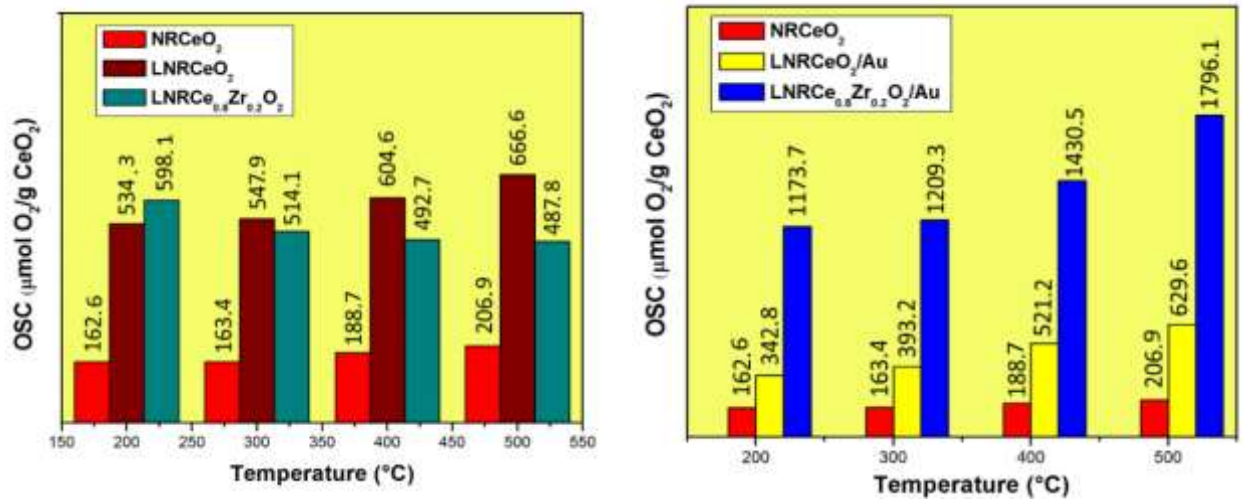

Figure 24. Oxygen storage capacity values in µmol – O_2/g CeO_2 for ceria samples used in this work at the temperatures of 200, 300, 400 and 500 °C.

4.7 - Gold deposition-precipitation reaction

$[AuCl_4]^-$ is a gold square planar ion commonly used as a precursor for the synthesis of gold nanoparticles. According to Corma, when dissolved in water, this species stablishes an equilibrium with several other gold chlorohydroxyl coordination ions as depicted: [119]

$$[AuCl_4]^-_{(aq)} + OH^-_{(aq)} \rightleftarrows [AuCl_3OH]^-_{(aq)} + Cl^-_{(aq)} \quad (14)$$

$$[AuCl_3OH]^-_{(aq)} + OH^-_{(aq)} \rightleftarrows [AuCl_2(OH)_2]^-_{(aq)} + Cl^-_{(aq)} \quad (15)$$

$$[AuCl_2(OH)_2]^-_{(aq)} + OH^-_{(aq)} \rightleftarrows [AuCl(OH)_3]^-_{(aq)} + Cl^-_{(aq)} \quad (16)$$

$$[AuCl(OH)_3]^-_{(aq)} + OH^-_{(aq)} \rightleftarrows [Au(OH)_4]^-_{(aq)} + Cl^-_{(aq)} \quad (17)$$

The percentual distribution of each one of these species is indeed pH-dependent and it was properly calculated by Hönes et al who summarized all the information in the graph shown in the Figure 25. [120-121]

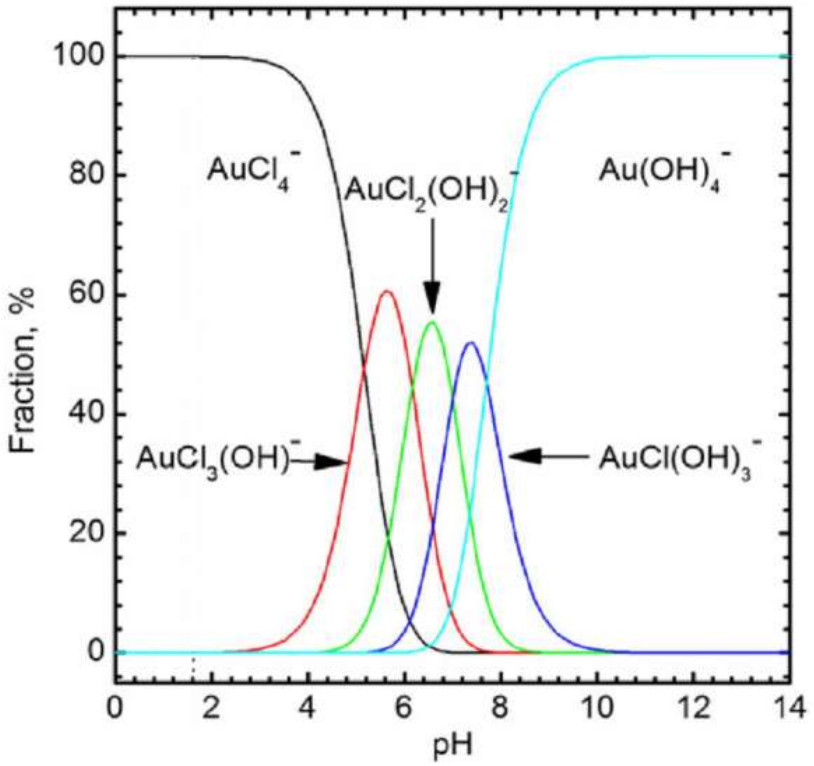

Figure 25. pH-dependent distribution of gold(III) species in aqueous solution. Image adapted from [119].

The dominating species in solution at the preparation pH (pH 9) and temperature (80 °C) is $[Au(OH)_4]^-$ which is the chemical species involved in the mechanism of chemisorption, crucial to the anchoring of Au NP's on the surface of the ceria nanorods, as seen in Figure 26.

$$Ce - OH_{(surface)} + [Au(OH)_4]^-_{(aq)} \rightarrow Ce - O - Au(OH)_{3(surface)} + H_2O \quad (18)$$

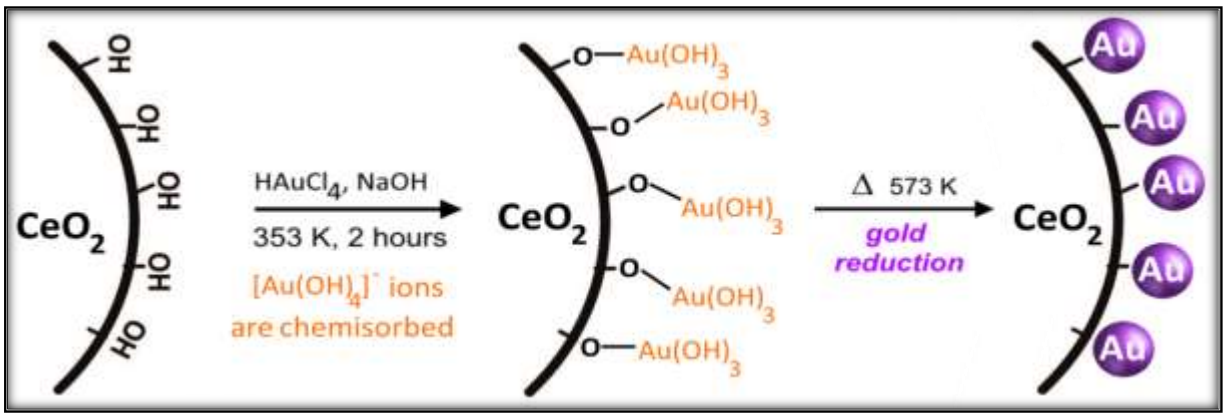

Figure 26. Mechanism of chemisorption of $[Au(OH)_4]^-$. Hydroxyl groups accomplish a nucleophilic attack to form gold-hydroxyl species anchored to the ceria nanorods, which are subsequently heated leading to the formation of small Au NP's.

In order to study the surface properties of the nanorods, zeta (ζ) potential values were analyzed over a range pH values between 3 and 10 to determine the point in which the net charge over the surface of the NP's would be neutral, i.e. the isoelectric point. As it can been seen in Figure 27, at low pH values, nanorods exhibit positive ζ-potential values, which are accounted for protonated hydroxyl groups present at the surface of NRCeO2 that are under the form $Ce - OH_2^+$. For high pH values, nanorods exhibit negative values of ζ-potential value, explained for the formation of deprotonated forms of hydroxyl groups, $Ce - O^-$. At an intermediate value, exactly at **9.11**, ζ-potential equals zero, which means hydroxyl groups are at their neutral form, $Ce - OH$.

For very positive ζ-potential values, the protonated hydroxyl groups are not nucleophilic enough to perform nucleophilic substitutions on the gold complexes. For very negative ζ-potential values, the negative charge may lead to electrostatic repulsion between ceria surface and gold complexes (all of them are negatively charged regardless the pH of the solution). Thereafter, the best compromise is to

perform the reaction close to the isoelectric point. The determination of the isoelectric point of the material used in this work at 9.11 corroborates that the pH proposed by experimental procedure (pH = 9) found on the literature is the optimal for the performance of the deposition-precipitation method. [122]

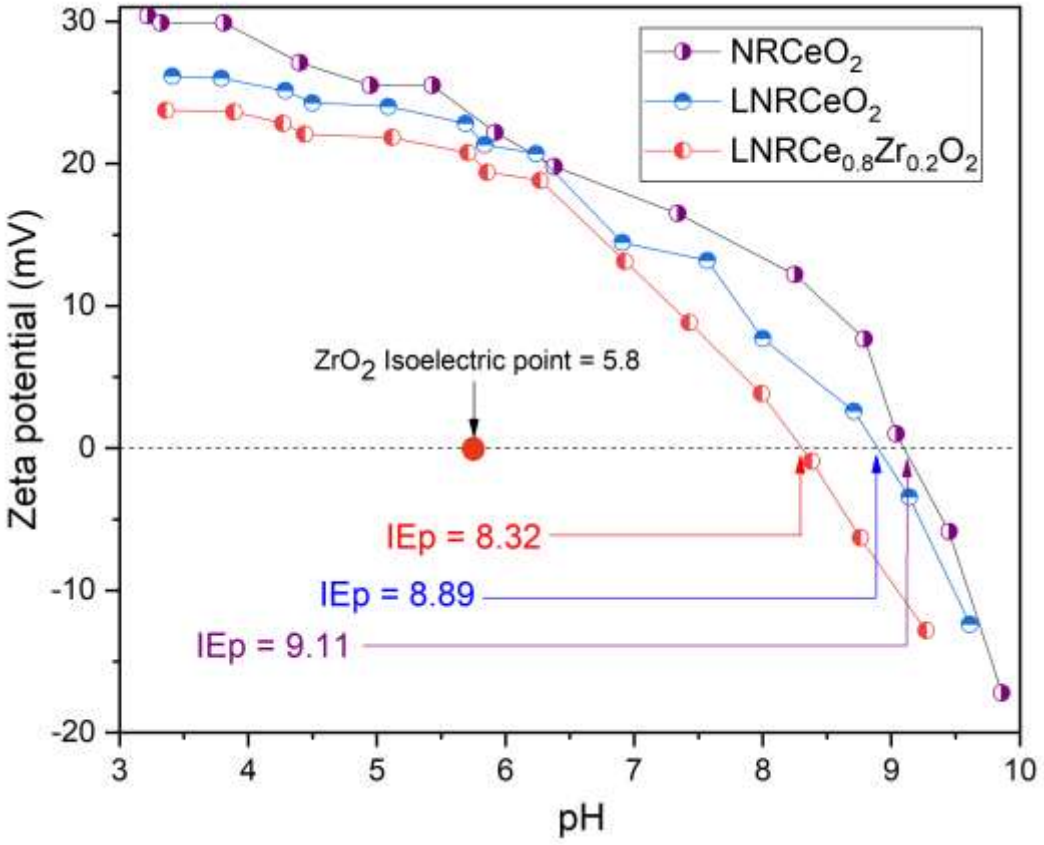

Figure 27. ζ-potential determination for a dispersion of CeO_2-NR in deionized water over a range of different pH's values ranging from 3 to 10.

$LNRCeO_2$ and $LNRCe_{0.8}Zr_{0.2}O_2$ exhibited lower, although not quite different, values of IEP's (8.89 and 8.32 respectively). Zirconia is known to be a more acidic oxide when compared to ceria. Although many features might interfere in a transition metal oxide acidity, such as crystal structure (tetragonal zirconia, for example, is more acidic than monoclinic), surface orientation, surface area, etc., higher acidity attributed to zirconia and, as a consequence, its lower isoelectric point might be attributed to the higher effective nuclear charge of Zr^{4+} when compared to $Ce^{4/3+}$. Parks [123] have reported that ceria-zirconia solid solutions present an intermediate

IEP, not necessarily proportional to the metal ratio. This seems to be the case here where LNR$Ce_{0.8}Zr_{0.2}O_2$ presented an IEP = 8.32.

Urea was used in this work as an alternative to sodium hydroxide in order to accomplish a slower and more homogeneous DP reaction over the surface of CeO_2, as urea slowly undergoes hydrolysis in water upon heating:

$$CO(NH_2)_{2(aq)} + H_2O_{(l)} \rightarrow CO_{2(aq)} + 2\,NH_{3(aq)} \quad (19)$$

Zanella and coworkers has already successfully employed this method for depositing Au NP's over the surface of titania, choosing an appropriate amount of ammonia so that the solution final pH would be around IEP of titania. [124] For this work, a procedure was adapted so that the final pH would be around the IEP of the nanorods determined previously by DLS. The pH of solution was monitored over time during the 4 hours the reaction took place and the results are displayed in Figure 28. It evolved from 4.24 at the start of the reaction, as $HAuCl_4$ was used as the gold precursor species for the NP's and ended at around 9.51, not quite far from the pH desired for the DP synthesis.

Urea decomposition reaction is endothermic, which implies that an increase in the temperature not only favors the reaction kinetically, but also thermodynamically. Even though urea hydrolysis leads to the formation of either CO_2, an acidic oxide, and ammonia, a basic compound, the net effect is that the solution pH increases over time as the reaction proceeds. The reasons for this are that ammonia is not only produced as twice as carbon dioxide, but it is also way more soluble in water at 80 °C (9.01 mol L^{-1} for ammonia and 7.89×10^{-3} mol L^{-1} for carbon dioxide, i.e. NH_3 is more than 1000 times more soluble than ammonia at the set temperature used for the reaction). This might arise from the fact that while ammonia is composed of quite polar molecules which establishes strong hydrogen bonds with water, carbon dioxide, even though it reacts in a small extent to form carbonated species in water (H_2CO_3, HCO_3^-, etc.), is a non-polar molecule with restricted solubility in water. [125]

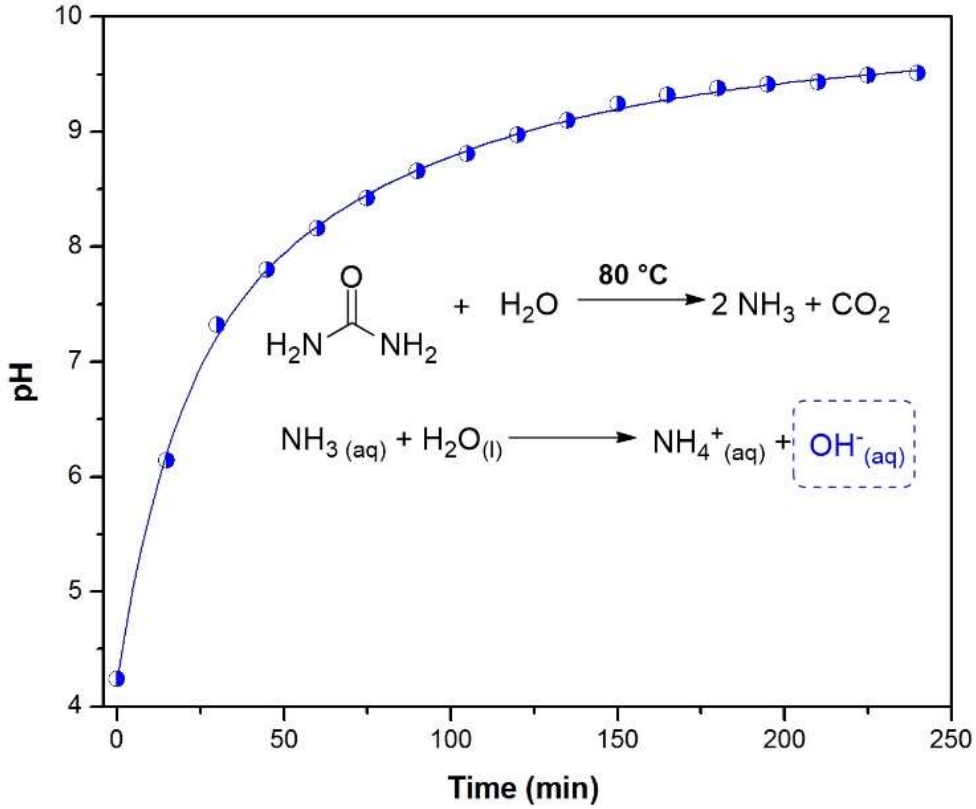

Figure 28. Evolution of solution pH during the aqueous decomposition of urea measured by a pH meter for the reaction of DP of Au NP's over the ceria nanorods at 80 °C.

With the growth of Au NP's over the nanorods, which is seen in Au diffraction peaks are possible to be seen, although with a specific zoom as in the Figure 29, as they are considerably broad and of low intensity due to the small size of the nanoparticles obtained by DP synthesis (< 5 nm). Au NP's crystallize in a cubic crystal structure (a = 4.079 Å), which is confirmed by comparison with reference data [126] and in quite good concordance for both peaks at 2θ = 38.2° and 44.4° for 111 and 200, respectively.

HRTEM images were obtained from CeO_2/Au samples and showed that gold nanoparticles exhibited excellent crystallinity and size determined at (2.4 ± 0.9) nm, as depicted in Figure 30. It is even possible to see diffraction fringes associated with some of the crystallographic planes associated with gold, as seen in Figure 31.

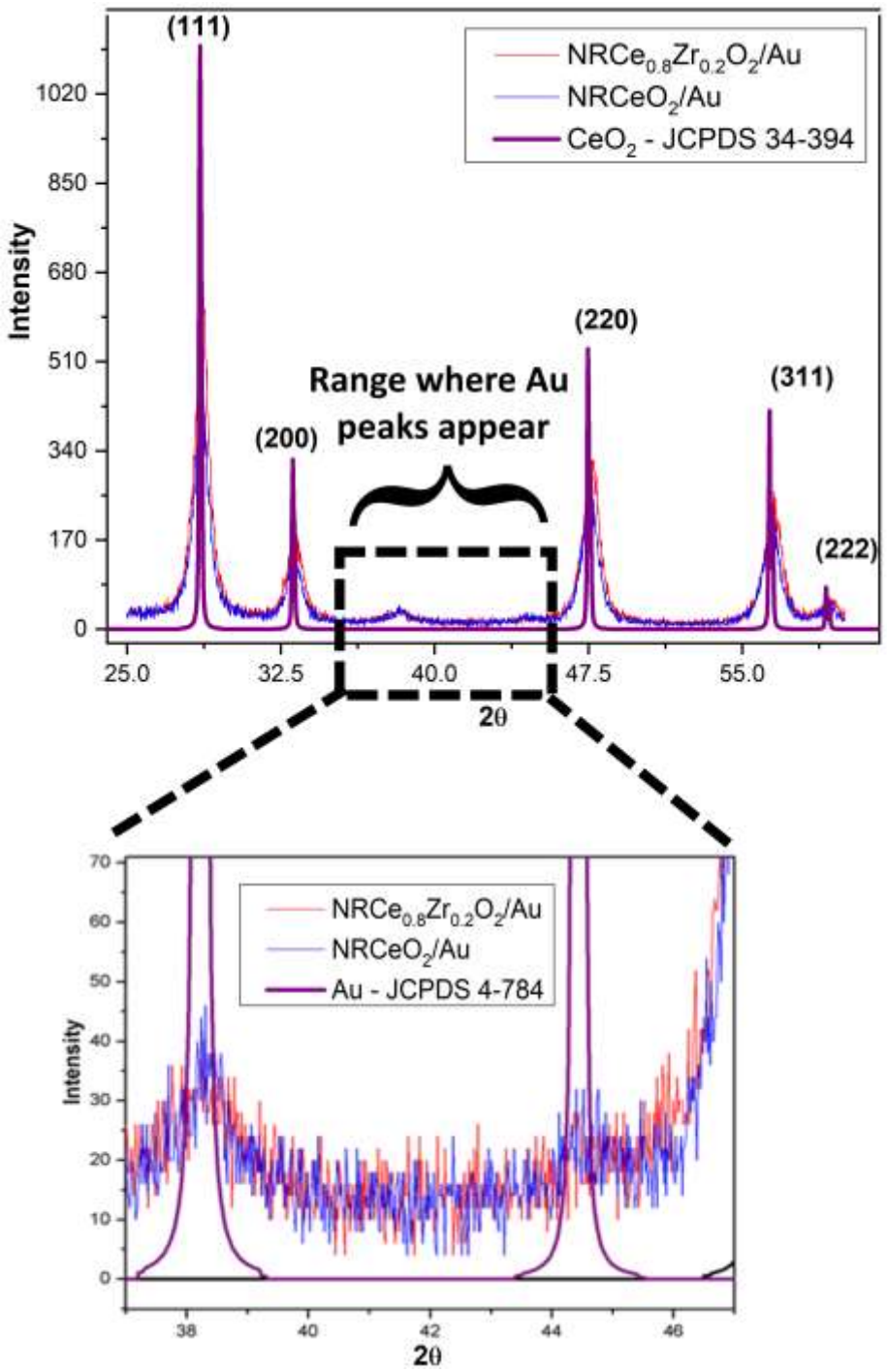

Figure 29. X-ray diffractograms of $NRCeO_2$ NR/Au and $NRCe_{0.8}Zr_{0.2}O_2$/Au with focus on two different 2θ ranges: (a) from 25° to 60°; (b) from 37° to 48Reference diffraction patterns used were: for cubic CeO_2 JCPDS 34-394 and for Au JCPDS 4-784.

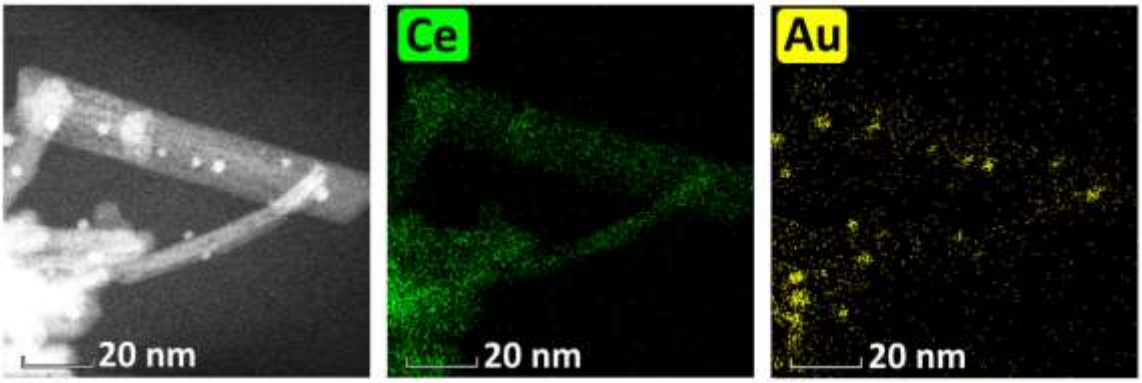

Figure 30. HRTEM image for CeO_2/Au. EDS mapping for cerium and gold were also performed in order to confirm the position of the nanorods and the metallic nanoparticles over the surface.

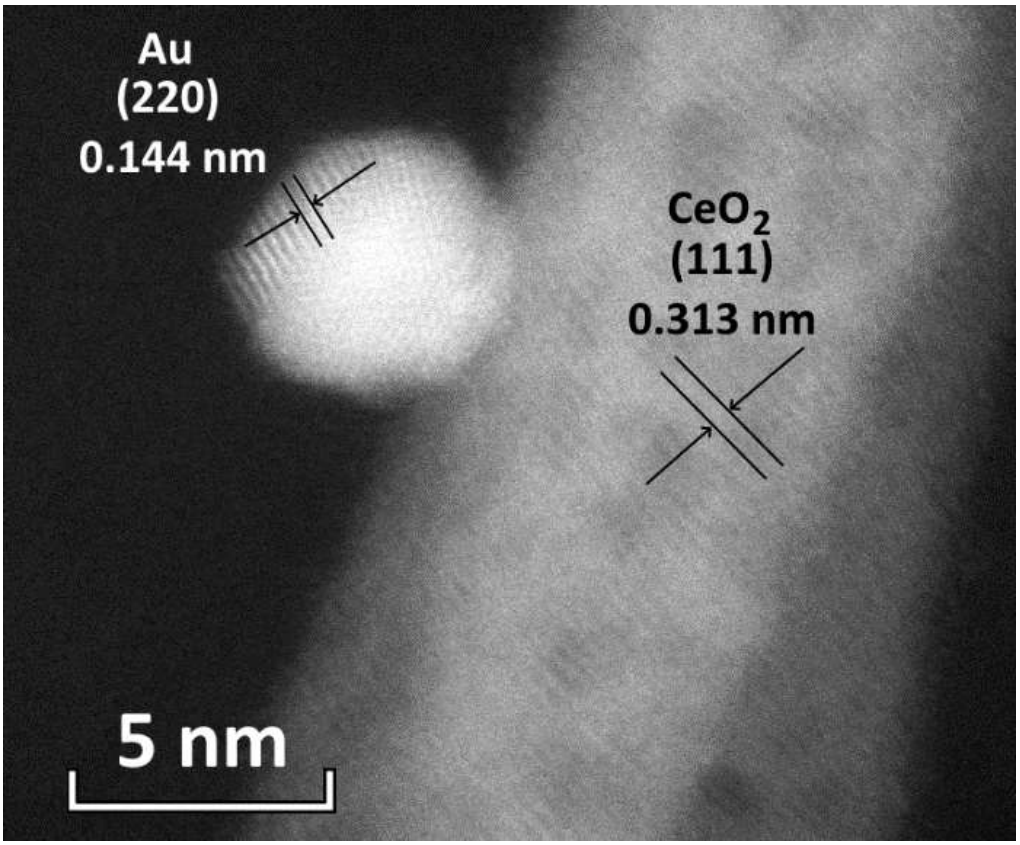

Figure 31. HRTEM image for CeO_2/Au. Diffraction fringes for some of the crystallographic planes of gold and ceria can be seen in evidence in the picture.

4.8 - DRS results

Diffuse reflectance spectroscopy was used to analyze and compare $LNRCeO_2$ and $Au/LNRCeO_2$ in order to understand their optical properties and estimate band gap values.

The Kubelka-Munk function, $F(R)$, was applied to reflectance data (R) to analyze the remission of each sample in the UV-Vis region.

$$F\,(R) = \alpha = \frac{(1-R)^2}{2R} \qquad (6)$$

When $F\,(R)$ is plotted against λ values, absorbance results are obtained for a wavelength range.

The Kubelka-Munk function plot for catalyst samples is depicted in Figure 32. As it is shown in Figure 32, there is a strong absorption band below 400 nm in the spectra for both samples, which is due to the charge transfer from O^{2-} 2p orbitals to Ce^{4+} 4f orbitals in CeO_2. [127] According to the rule-of-thumb colour wheel disk, when a sample absorbs radiation close to upper energy limit of visible range, i.e., the violet colour, the sample will exhibit the complementary colour, which is yellow, which is in good agreement to the pale-yellow colour shown by ceria nanorods.

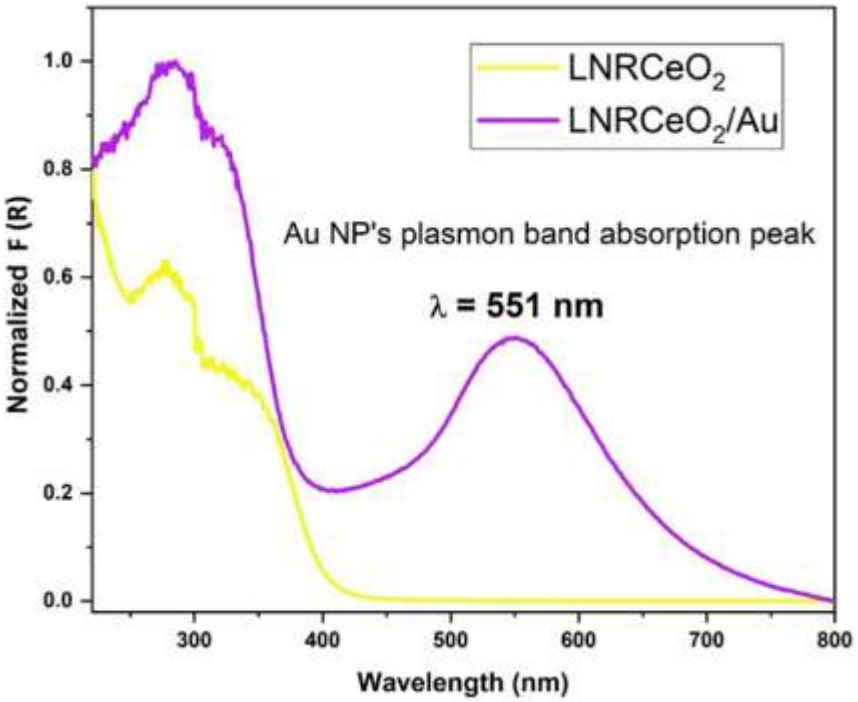

Figure 32. Absorbance plot for $LNRCeO_2$ and $LNRCeO_2$ obtained by Kubelka-Munk plot applied to reflectance data obtained for $LNRCeO_2$ and $LNRCeO_2/Au$.

However, when gold NP's are deposited over the surface of ceria nanorods, there are optical modifications in the sample, which is seen by the appearance of a band centred at 551 nm which is accounted to the Au NP`s absorption plasmon band.

In a few words, a plasma is a macroscopically neutral substance containing interacting free charged particles such as electrons and ionized atoms or molecules. In metals, such as gold, the free electron gas around metal atoms is treated as a solid-state plasma and plasmons can be regarded as the quantization of the plasma oscillations. [127]

When light strikes a metallic NP whose size is much smaller than its own wavelength, the radiation oscillating electric field interacts with the conduction electrons of the metal. The electron cloud is disturbed and shifted with respect to the positive ionic core. Due to this charge displacement, a dipole is established, and a coulombic force arises in order to restore the equilibrium position of the electron cloud. Therefore, the dipole oscillates in coherence with respect to the incident light, as shown in Figure 33. These collective electron oscillations occur at the metal surface and are called surface plasmons and are the responsible for the absorption of some specific wavelengths such as in the Au/CeO_2 catalyst system.

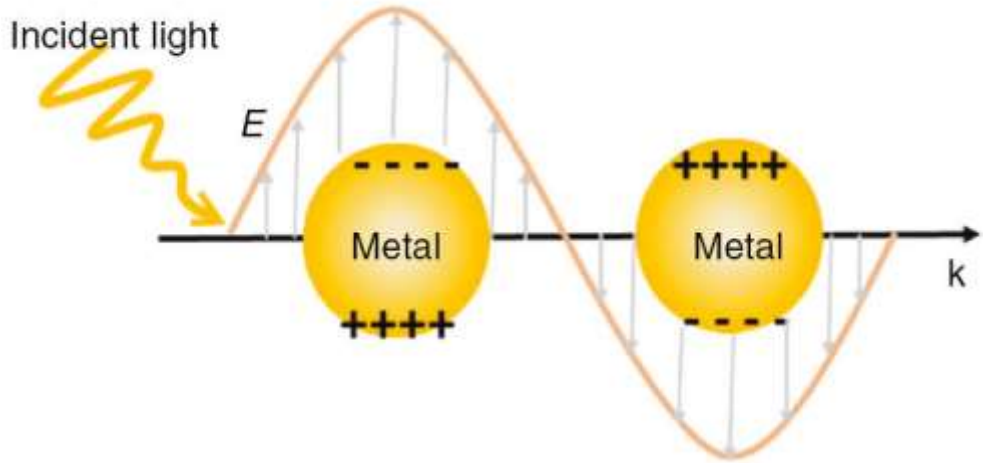

Figure 33: Plasmon oscillation on a metallic sphere with respect to the electric field of the incident light. Consequently, the conduction electron density is displaced relative to the nuclei to the negative side of the particles as indicated in the figure. Image adapted from [128].

The optical band gap values for the samples can be estimated from the transmittance spectra following Tauc's rule. The Tauc plot formula for determining optical band gap is:

$$F(R)h\nu = F(R)(h\nu - E_g)^{1/n} \quad (20)$$

where $F\ (R)$ is the Kubelka-Munk function, $h\nu$ is the photon energy, E_g is the band gap energy, n is a constant which can take values of 2, 2/3, 1/2, and 3 for the direct allowed, direct forbidden, indirect allowed and indirect forbidden, respectively. The band gap corresponding to the direct transition was obtained by extrapolating the linear portions of $(F(R)h\nu)^2$ versus the $h\nu$ curves up to the point $(F(R)h\nu)^2$ equals zero in a plot of $(F(R)h\nu)^2$ as a function of photon energy $h\nu$ for the sample, as shown in Figure 34.

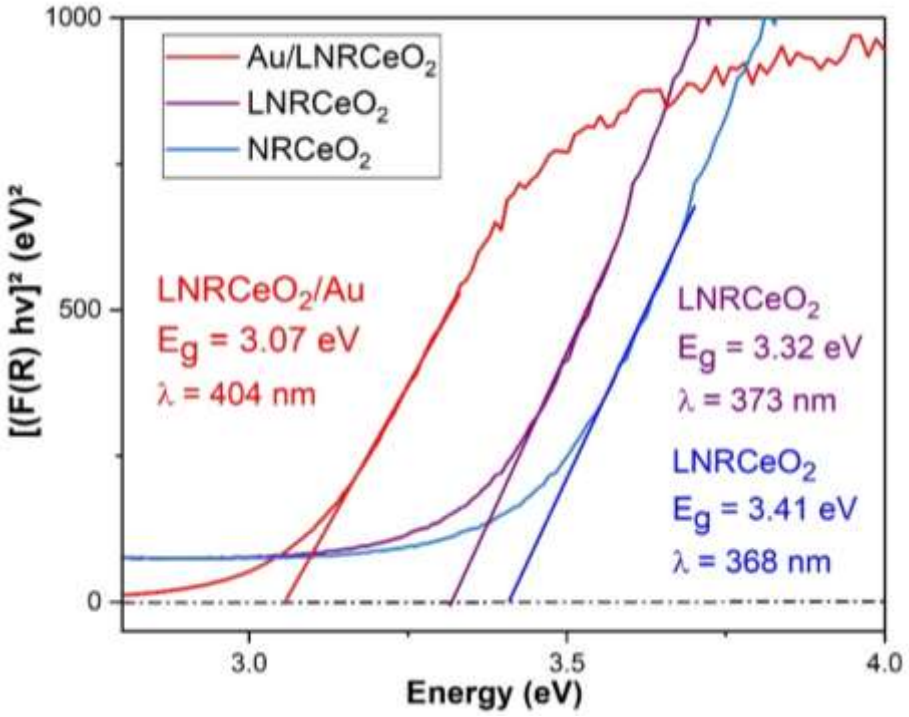

Figure 34. Tauc's plot of $(F(R)h\nu)^2$ versus the energy in electrons-volts for the samples of ceria nanorods prior and after lixiviation and $LNRCeO_2$. Band gap values corresponding to the direct transition were obtained by extrapolation of linear portions of the graph up to the point where $(F(R)h\nu)^2$ equals zero.

According to literature, the band gap (E_g) energy of bulk CeO_2 is 3.19 eV. [129] When a semiconductor is in nanometric size, the energy split between the valence

band and the conduction band increase due to the quantum confinement effect, so that the smaller the nanoparticles are, the larger the energy of band gap.

Ceria nanorods either before or after acid lixiviation exhibit 3.32 eV and 3.41 eV values of band gap, respectively, which are indeed larger the value for bulk ceria. This is expected once ceria nanoparticles are indeed under quantum confinement effect. There is also a decrease of the band gap value, which might be attributed to the fact that once lixiviated ceria nanorods exhibit a larger density of oxygen vacancies defects, this is also associated with a larger density of Ce (III) ions, as it was confirmed by Raman spectroscopy.

When the oxide is totally stoichiometric, all the constituent cerium atoms exist in the Ce(IV) oxidation state, but in the partially reduced form for each missing lattice oxygen atom, it is implied the existence of two Ce(III) ions in sites close, although not necessarily adjacent, to the vacancy. The stoichiometric oxide is therefore characterised by a completely empty f-band (located in an energy gap between the occupied O 2p states and the unoccupied Ce 5d states with electronic configuration [Xe] $4f^0$) whilst the partially reduced oxide features Ce(III) (electronic configuration [Xe] $4f^1$), and as consequence, in the diagram of states highly-localised partially-occupied f orbitals split-off below the unoccupied f states [130], as seen in Figure 35.

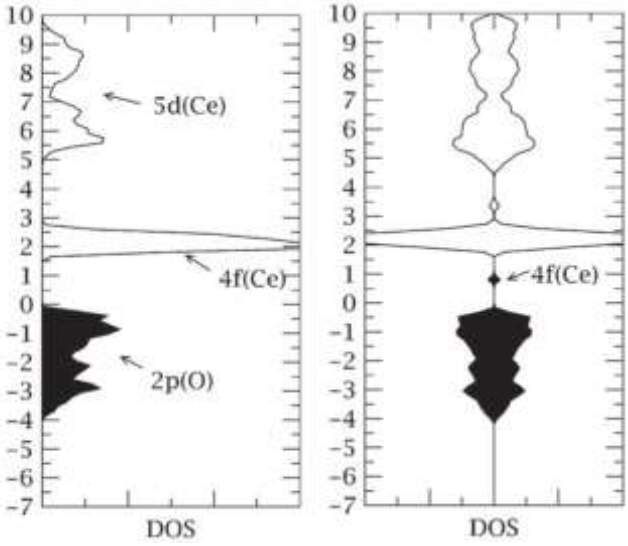

Figure 35. Diagram of density of states (DOS) depicting electronic structure of the stoichiometric CeO_2 surface (left) and the oxygen-vacancy-containing reduced surface (right) with occupied states shaded and unoccupied states unshaded. The density of the Fermi levels is set at zero and the units of the energy (y) axis are in eV. Image adapted from Zhang [130].

The presence of electrons in this 4f level accounts for the decrease in band gap when the ceria nanorods were lixiviated which corroborated the increase in number of oxygen vacancy defects.

It is known that the deposition of metallic NP's over the surface of semiconductors results in a decrease of the band gap values. This is essentially because the Fermi level energy of metals, i.e. the upper limit energy of electrons band, is usually right inside the semiconductor band gap, i.e. the energetic division between the occupied and unoccupied electronic states, as it is the case for ceria and summarized in Figure 36. The Fermi level energy of gold is situated right in the middle of the band gap of ceria and as the two components establish a chemical interaction, it is possible that electrons from gold might be promoted to the semiconductor conduction band and may account for the fact that the band gap of the metal/semiconductor system ($E_g(2)$) is smaller than for the semiconductor isolated. ($E_g(1)$).

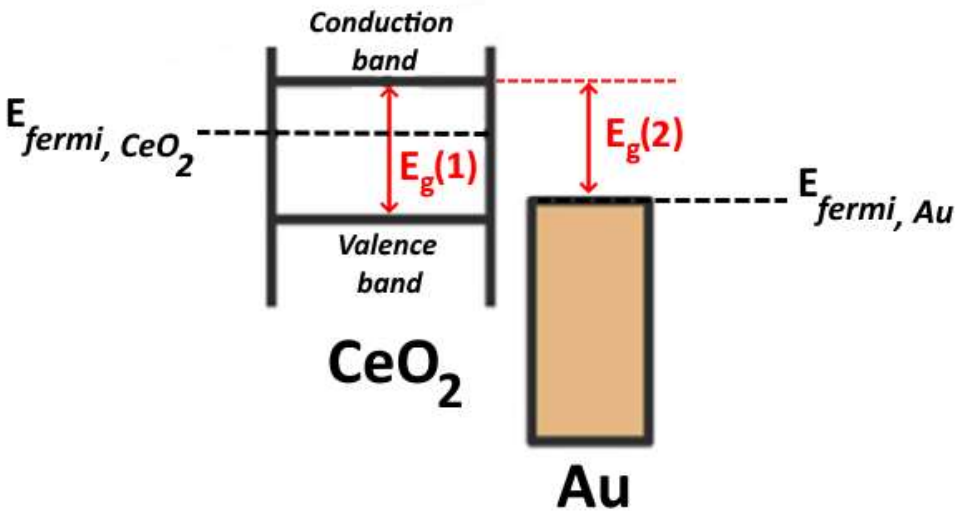

Figure 36. Representation of band energy for a system composed of metallic nanoparticles, in this specific case, gold, deposited over the surface of semiconductor nanoparticles, in this case, ceria.

This was seen for the Au/CeO_2 where the band gap value found (3.07 eV) is smaller than the values found for the nanorods and even smaller than for bulk ceria. These results might be rationalized via the interaction previously described in which the gold band structure is intertwined with the ceria band structure and it is responsible for the decrease in the band gap.

4.9 - XPS results

XPS (X-ray photoelectron spectroscopy) analysis is a surface-probing technique obtained by exposing a solid surface to an X-rays beam while simultaneously measuring the kinetic energy and electrons that are ejected from the surface layer, i.e., the 10 nm-deep upper layer over the material.

When an atom or molecule absorbs an X-ray photon, a core electron can be ejected. The kinetic energy (KE) of the electron is dependent on the incident photon energy ($h\nu$) and the binding energy (BE) of the electron (i.e., the energy required to remove the electron from the surface).

Peaks appear in the spectrum from atoms emitting electrons of a characteristic energy correspondent to a specific BE. The binding energies and intensities of the photoelectron peaks enable element analysis and identification.

For the lixiviated ceria nanorods, the analysis revealed that no peaks which could be attributed to the presence of sulfur S(2p) peaks, which indicates that there was no remaining of sulfate ions adsorbed on ceria surface after the acid leaching treatment and successive water washings. It is known that sulfur-based compounds are potent contaminants that might hinder the catalytical performance of the material for PROX-CO reaction. [131]

The spectra for fully oxidized vacancy-free CeO_2 and fully reduced CeO_2, i.e. Ce_2O_3, contain six and four peaks, respectively. The actual sample which is made up of CeO_{2-x} are composed up to ten peaks, originated from a hybrid of both forms. XPS spectra for lixiviated ceria nanorods is exhibited in Figures 38 e 39.

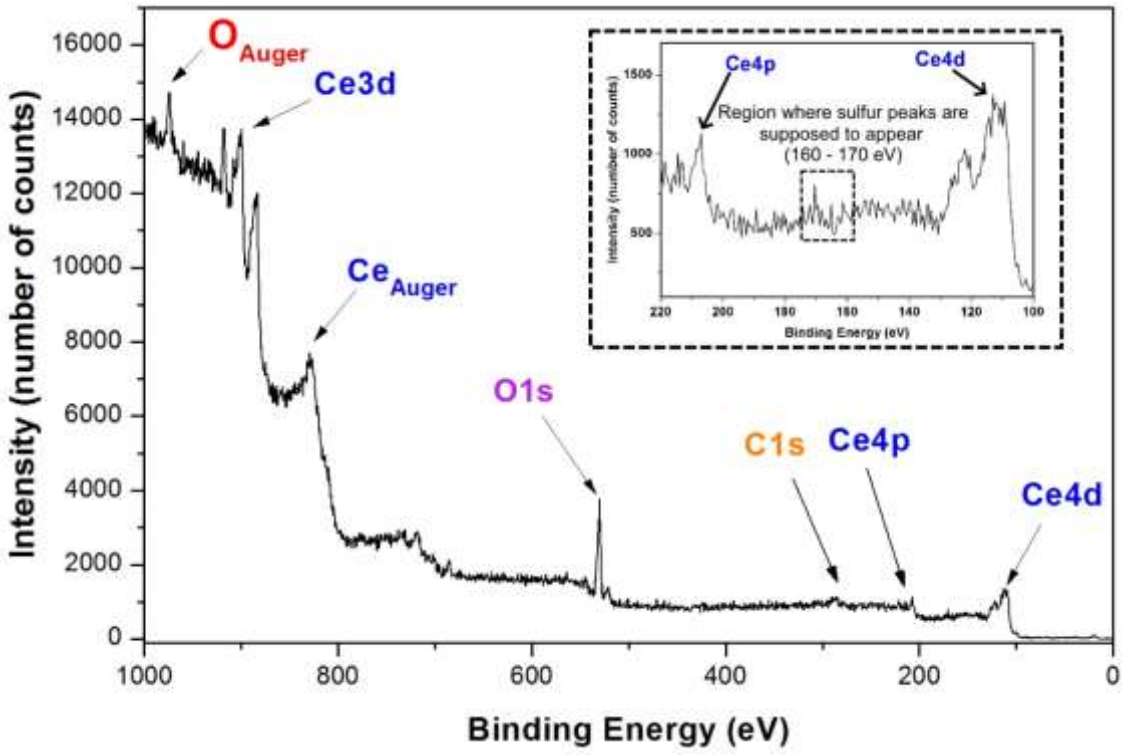

Figure 37. XPS spectrum for lixiviated ceria nanorods ($LNRCeO_2$).

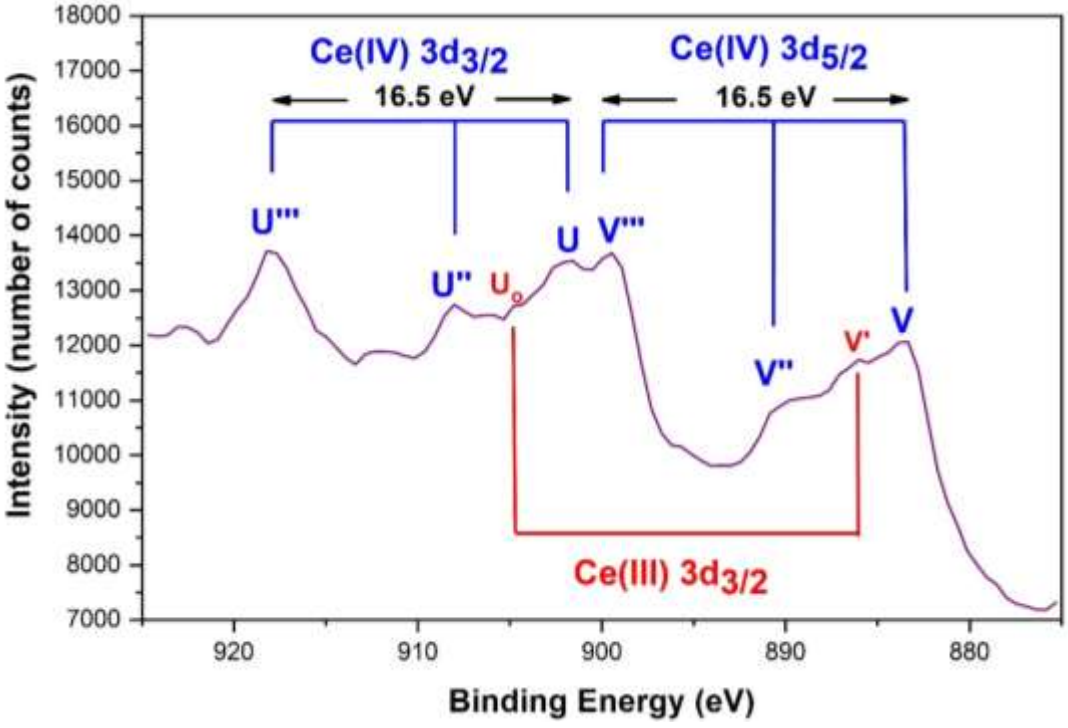

Figure 38. XPS spectrum for lixiviated ceria nanorods ($LNRCeO_2$) zoomed in the region of binding energies between 925 and 875 eV.

The peaks labeled V''' and U''' are associated with the Ce $3d^9$ O $2p^6$ Ce $4f^0$ final state with a spin-orbit splitting of 16.5 eV. The spin-orbit coupling effect is a result of an interaction between the electron's spin and its orbital motion around the nucleus. When an electron moves in the electric field of the nucleus, the spin–orbit coupling causes a shift in the electron's atomic energy levels due to the electromagnetic interaction between the spin of the electron and the electric field.

The additional peaks result from so-called "shake-down" states where electrons are transferred from the O 2p level to the Ce 4f level in the excited state.

4.10 - CO oxidation catalytic results

The catalytic performance of five relevant samples is exhibited in Figure 39. It is known that ceria nanorods by themselves do not present expressive catalytic activity for the oxidation of CO below 300 °C. The catalytic activity of these samples arises from the interaction of the Au NP's and the oxide support. Major information about each one of the samples is summarized in Table 10. The code used for each one of the samples is [***Type of ceria nanorods employed, either lixiviated or not***]_[***Method of deposition employed for the sample***])_[***Annealing temperature for the preparation of the catalyst***] and they have been name Cat1 to Cat5 for short reference onward in this work.

Table 11. Information about Au weight content and mean Au NP`s radius size in each one of the catalyst.

Sample	Au content (%)	Mean Au radius size (nm)
Cat1 **(NRCeO2_NaOH_300)**	0.94	2.5 ± 0.4
Cat2 **(LNRCeO2 _NaOH_300)**	0.97	2.6 ± 0.5
Cat3 **(NRCe0.8Zr0.2O2_NaOH_300)**	1.09	2.4 ± 0.6
Cat4 **(LNRCeO2_urea_300)**	0.94	1.8 ± 0.3
Cat5 **(LNRCeO2_NaOH_400)**	0.92	3.6 ± 0.2

High selectivity to the formation of CO_2 at lower temperatures have been constantly associated to the presence of H_2O molecules, formed by the oxidation of H_2, which remain chemisorbed to the surface of ceria. These chemisorbed H_2O molecules tend to react with CO molecules also adsorbed on the surface, on a WGS reaction leading to the production of CO_2 and H_2.[132] As the temperature increases, water

molecules desorb more easily from the oxide surface. Consequently, the aforementioned WGS reaction on the surface is inhibited and, therefore, CO_2 selectivity decreases.

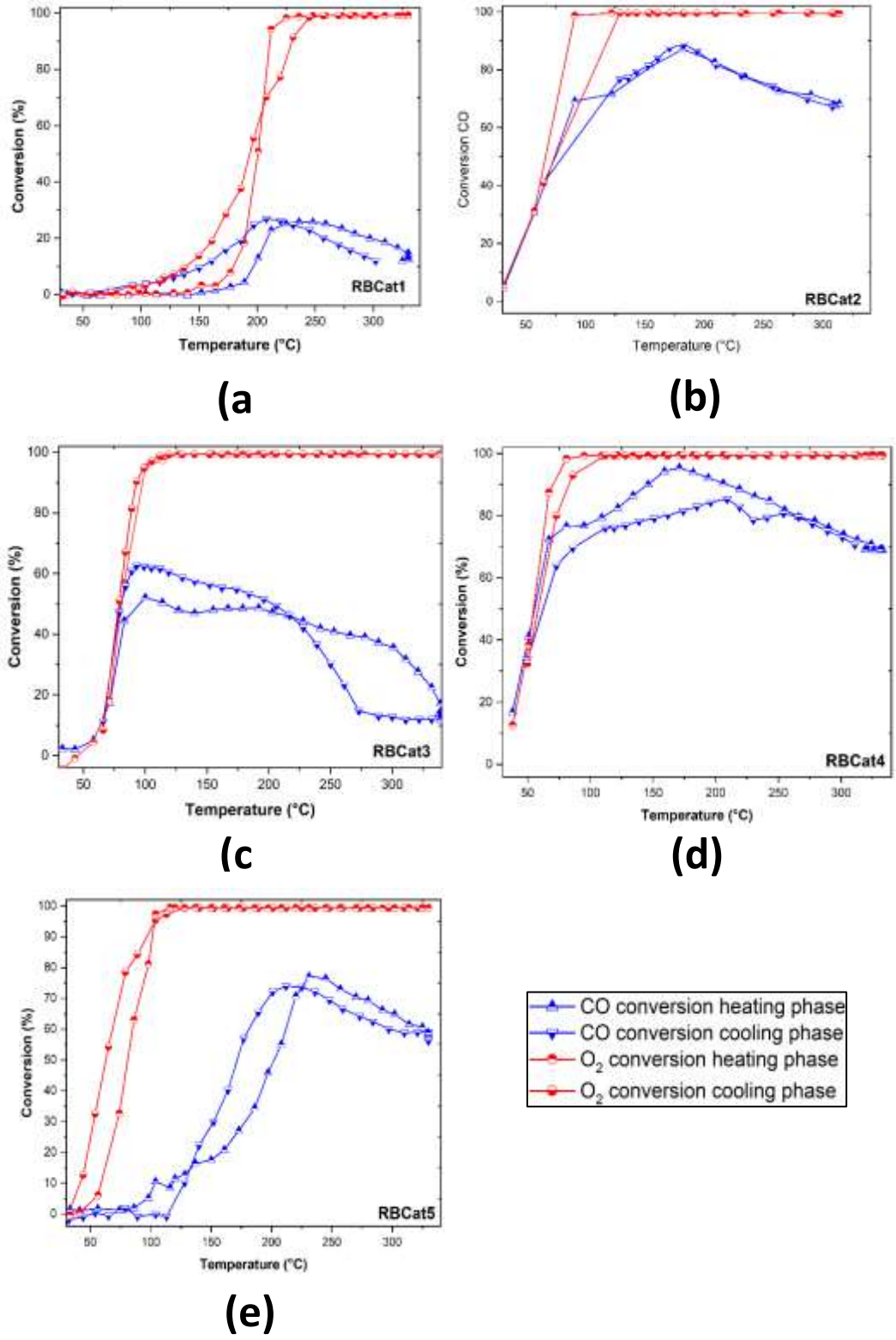

Figure 39. CO and O_2 conversions for the samples Cat1 through Cat5 in the 50 °C – 350 °C range temperature.

Koo et al [132] highlight that, despite the activation energy for the oxidation of CO is smaller than the one observed for the oxidation of H_2, the latter is in vast excess in the used experimental conditions that its oxidation prevails over CO's.

4.10.1 - Mechanism of the reaction

Widmann et al and collaborators argue that two mechanisms are possible.[134] The first one is the **Mars-Van-Krevelen** (MvK) type. By the description of this mechanism, the oxidation of CO is carried out at the peripherical zone between the Au NP's and the ceria support with some of the oxygen ions from the ceria lattice taking part of the reaction together the oxygen atoms provided by the O_2 molecules. The other mechanism is the **Langmuir-Hinshelwood**. According to this one, the reaction is carried out only between adsorbed molecules on the surface of Au NP's without participation of atoms from the CeO_2 support.

The results of the catalytic tests however, for example, for Cat2, Cat4 and Cat5, reveal that the maximum of conversion of CO takes place when the oxygen supplied to the system has been totally consumed allowing us to infer that the oxygen accounted for the oxidation of CO is coming not from the O_2 molecules, but from the ceria lattice. This suggests that although these two mechanisms might be taking place simultaneously, MvK might be the favoured one. A general schema for this mechanism is provided in Figure 40.

Song et al accomplished DFT studies about the MvK mechanism for the oxidation of CO on CeO_2/Au systems like the ones in this work. [99] According to the authors, at first, gold nanoparticle would strongly bind to a CO molecule by -1.13 eV and, then, the CO molecules interacts with the ceria support forming a transition state (TS) in which the geometry around the carbon atom is trigonal. This step is highly exothermic with an energy barrier of only 0.01 eV. Kim et al also modelled for the system in which ceria would be totally stochiometric with no vacancy at all, and the barrier energy for this step would be 0.47 eV, confirming the importance on the formation of vacancies. [135] The next step then is the CO_2 desorption that, by far, shows the highest energy barrier of +2.17 eV. Although the formation of a C=O bond in CO_2 is highly exergonic, this does not compensate in the transition state to the

energy necessary for ripping out an oxygen from the ceria lattice and that justifies why the E_a is so high.[99]

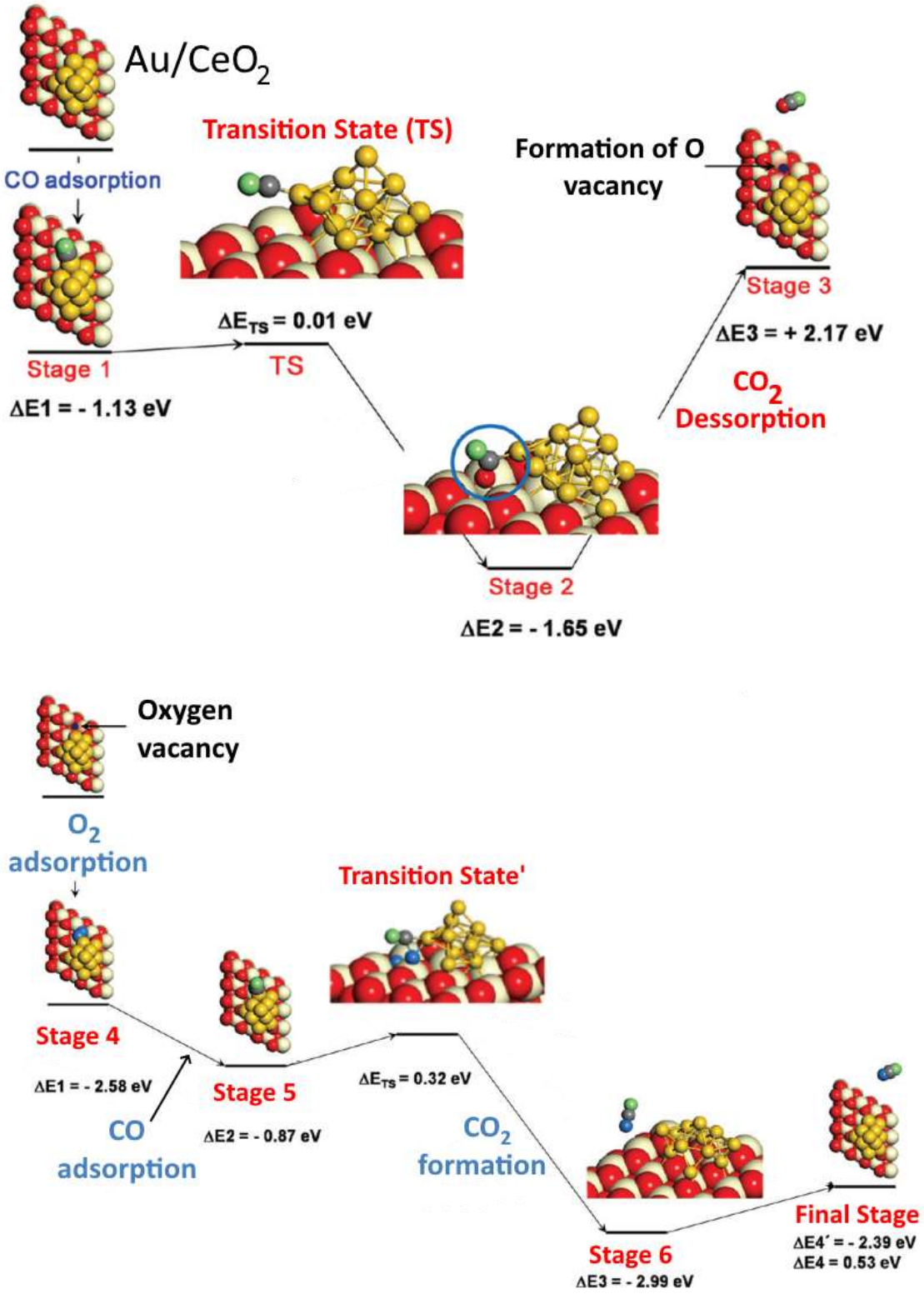

Figure 40. Mars-Van-Krevelen mechanism for the oxidation on the surface of Au/CeO₂ catalysts. Image adapted from [97].

Then, a surface oxygen vacancy on CeO_2 establishes a strong bond by with a gas-phase molecule -2.58 eV and heals a vacancy left behind by the elimination of a CO_2 molecule. Then, another CO molecule is adsorbed on the surface of Au NP's, which is subsequently followed by the formation of a transition with barrier energy = 0.32 eV in which a trigonal-shaped carbon atom is bonded to one of the oxygen atoms previously attached to the vacancy. The final steps are then, the formation of a CO_2 molecule, which is quite exothermic (ΔE = -2.99 eV) and its endothermic desorption (ΔE = +0.53 eV) leaving an oxygen-replenished ceria behind.

This might be associated not only to the mean size of Au NP's , which is, in Cat4, (1.8 $\pm$ 0.4) nm, while in Cat2 is 2.6 $\pm$ 0.5. Furthermore, in a qualitative, there seems to be a better distribution of particles in Cat4, as seen in Figure 45 in the appendix. As the pH increases slowly for the urea-based DP, this leads to the formation of more deposition sites for the formation of. The better distribution of gold particles over the surface might also interfere to rationalize why the sample synthesize by the urea-based DP was better than the NaOH-based.

4.10.2 - Effect of annealing temperature used in catalyst synthesis

When samples Cat2 and Cat5 are compared, the effect of the annealing temperature is studied. It is observed than when higher annealing temperature is used, a lower catalytical conversion is observed. While for Cat2, it attains a maximum conversion of 89 % and at 181 °C, for Cat5 it only reaches a maximum of 73% at 210 °C. HRTEM images as seen in Figure 46 in the appendix reveal that higher annealing temperature lead to the production of larger and more rounded gold nanoparticles.

4.10.3 - Comparison of lixiviated and non-lixiviated nanorods for catalysis

It has been already reported that when ceria nanorods with native pore structure are compared to similar in which the pores have been expanded, the temperature for maximum conversion for PROX-CO reaction dropped.[101] For this case, OSC measurements allowed us to see that OSC values for $LNRCeO_2$ are more than three times higher than the one observed for pristine nanorods for the

range of temperatures used for the catalysis in this work. Song has studied by DFT the mechanism of CO oxidation in Au/CeO_2 and proposed that it proceeds preferentially via a gold-assisted Mars-Van-Krevelen mechanism, as depicted in Figure 40. By the mechanism, the atoms exchange processes happen in the peripheral zone between the Au NP's and the ceria surface. The rate limiting step is the transition from (v), where oxygen atoms are linked to the surface of ceria to a TS where one oxygen establishes a bond with an Au atom.

When the catalytic activity of Cat1 and Cat2 are compared, it is observed that the lixiviation of ceria nanorods prior to the deposition of Au NP's have a profound impact on the catalytic performance. As the weight fraction and dispersibility of Au NP's are practically the same, as seen in Figures 42 and 43 in the appendix, the difference might be due changes in the O vacancies in each one of them. Li et al has shown that ceria nanorods whose native pores have been expanded exhibit larger Ce^{3+}/Ce^{4+} ratio. This also seems to be the case for the lixiviated nanorods developed in this work. They showed higher values of OSC when compared to pristine nanorods, which can be correlated with the fact that these samples have larger Ce^{3+}/Ce^{4+}, higher number of $V_O^{\cdot\cdot}$. Therefore, it should exhibit a smaller enthalpy of abstraction of an O atom on the surface, which is directly intertwined with the reduction on the activation energy of the aforementioned rate-determining step (RDS). As this step, the easier thermodynamically it is to break the ceria surface – oxygen bond, the lower the RDS activation energy gets.

4.10.4 - Effect of zirconium doping

When the catalytic activity of Cat1 and Cat3 are compared, it is noticed that the latter tops up a maximum conversion of 63% at 95 °C, while the former is not quite effective for the catalysis as it only reaches 26% of conversion at 209 °C. This might be associated with the fact that NR$Ce_{0.8}Zr_{0.2}O_2$ OSC values are 30% higher than non-doped ceria nanorods. As previously discussed, as the effective ionic radius of Zr (IV) is smaller than that of Ce(IV) and Ce(III), the introduction of zirconium increases the concentration of $V_O^{\cdot\cdot}$, and as a consequence, OSC values verified are larger. As discussed for the MvK mechanism, the RDS is the desorption of the CO_2 molecule, whose energy which is intrinsically associated with the

thermodynamic trend of the support to form vacancies, which is favored in the case of $LNRCe_{0.8}Zr_{0.2}O_2$/Au. HRTEM images for this catalyst are seen in Figure 44 of the appendix.

4.10.5 - Effect of deposition-precipitation procedure

Haruta et al were the first to report that the reactivity of Au NP's sharply rises when the diameter decreases below 4 nm. [122] Afterwards, Valden and Goodman complemented Haruta's studies and pointed out that there would be an optimum diameter around 3 nm for which the activity of these particles would be at the very best. [135] Laoufi performed operando studies for Au/TiO_2 systems by *operando* GISAXS and reported that with a shifted sigmoidal behavior as depicted in Figure 27.[136] Minor variations from the optimum diameter led to a sharp decrease in the catalytic activity. This might be the case also for the systems studies in this work.

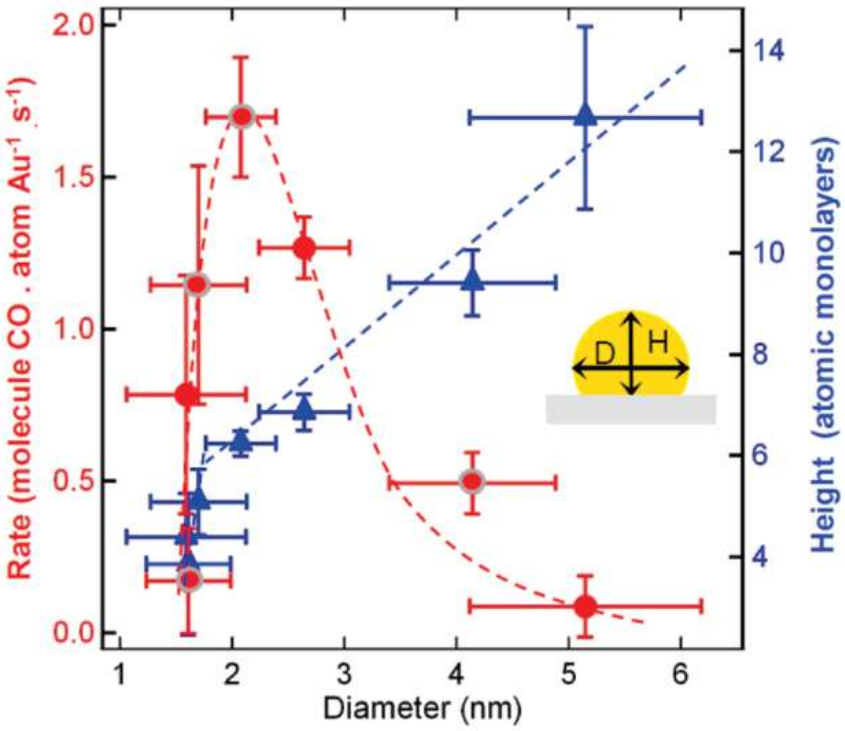

Figure 41. Reaction rate for PROX-CO as a function of the Au mean particle diameter over the surface of TiO_2 determined by* operando-*GISAXS. Adapted from [136].

When the catalytic activity of Cat2 and Cat4 are compared, it is noticed that the method by which the DP is performed induces differences for catalytic

applications. While Cat2 while attains a maximum conversion of 89 % and at 181 °C, for Cat4, the catalyst tops up 95 % conversion at 170 °C.

Zanella et al performed similar studies for systems composed of Au NP's deposited over the surface of titania by DP via decomposition of urea et and concluded by EXAFS and XANES results that the composition of the colloidal gold compound over the oxide surface be $AuN_{2.2}O_{1.2}C_{0.9}H_{4.2}Cl_{0.1}$.[48] This leads to the reasonable conclusion that gold might have reacted with some of the species formed in the decomposition of urea in the aqueous solution forming n nitrogen-containing compounds. Zanella [137] proposed that these species could be coordination complexes, such as $[Au(NH_3)Cl_3]$, or even mixed precipitates, e.g. $(AuHNNH_2).3H_2O$ or $NH(AuNH_2Cl)_2$.

After thermal annealing, these compounds would be converted into the Au NP`s, which could still be containing nitrogen in their composition, which could interfere in the catalytical performance of the material.

5. CONCLUSION AND PERSPECTIVES

In this work, the synthetic procedure chosen to synthesize CeO_2 nanorods was proven to be effective for the synthesis of the desired morphology in a controlled manner. When the strategy was adapted to produce Zr-doped ceria nanorods, the morphology control was still maintained, even for higher levels of the doping agent (up to levels as high as 40%), maintaining the porous structure included

The novel method that has been developed to lixiviate the native pore structure of ceria nanorods have been proven successful by HRTEM images which showed the expansion of the porous structure. OSC measurements of the materials proved that the lixiviated porous CeO_2 nanorods exhibited OSC values more than 3 times larger, while Raman measurements proved that the Ce^{3+}/Ce^{4+} was also modified after the lixiviation process. The crystalline structure though was not compromised or modified as shown by XRD results after the acid exposure and the mass loss was minimal and smaller than 0.5%, as it was shown by ICP results.

Isoelectric point of the materials was determined to be close to pH 9, and based on this, a procedure based on the DP technique was successfully applied for the synthesis of quite small Au NP's on the surface of nanorods, smaller than 4 nm.

DRS results showed that the deposition of Au NP's over the surface of CeO_2 changed the band structure of the semiconductor and the band gap was significantly altered, an indication of a strong interaction between the Au NP's and CeO_2 nanorods in the catalyst.

Finally, it turned out that the leaching treatment indeed increased the catalytic power of the material as a support. In addition, the zirconium doping process for the synthesis of $Ce_{0.8}Zr_{0.2}O_2$ nanorods also increased the ability of this system regarding the PROX-CO reaction, showing that maximum conversion for the reaction has increased, while the maximum conversion temperature has decreased, which is the sought characteristic for a catalyst with potential application for purifying hydrogen gas to be used PROX-CO catalytical systems.

The flash lixiviation process employed in this project may also be applied to other porous oxide nanoparticles synthesized in the research group in order to evaluate what might be the impact on topological, optical and catalytical properties as well. Au/CeO_2 is a potential catalyst class for the studied reaction with recent

bursting interest. This work adds more information into this class of catalyst for PROX-CO and paves the way to more studies about metal NP's deposited non-stoichiometric oxide NP's to be studied in the future.

6. BIBLIOGRAPHIC REFERENCES

1. US Department of Energy Hydrogen and Fuel Cells Program, 2017 *Annual Merit Review and Peer Evaluation Report*. **2017**.

2. Sharma, S., Ghoshal, S.K. *Renewable and Sustainable Energy Reviews.* **2015**, 43, 1151-1158.

3. Ullah, S. et al, *J. Chin. Chem. Society Taipei*, **2014**, 62(2), 182-190.

4. Stafell, I, *Energy Environ. Sci.,* **2019**,12, 463-491.

5. Sharma, S.; Ghoshal, S.K; *Renewable and Sustainable Energy Reviews*, **2015**, 43, 1151-1158.

6. Smart L.; Moore, E.. *Solid State Chemistry*. **1995**, Springer US: Boston, MA.

7. Silva, I. C.; Sigoli, F. A.; Mazali, I. O.; *Journal of Phys. Chem.*, **2017**, 121, 12928-12935.

8. Souza e Silva, J. M. S, Strauss, M.; Maroneza, C. M.; Souza, E. R.; Gushikem, Y.; Sigoli, F. A.; Mazali, I. O.***; J. Mater. Chem.***, **2011**, 21, 15678-15685.

9. Ivanova, S., in *Renewable Hydrogen Technologies. Production, Purification, Storage, Applications and Safety*, eds L. M. Gandia, G. Arzamendi, and P. M. Dieguez (Amsterdam: Elsevier B. V), 225-243.

10. Holladay, J., D., Hu, J., King. D., L., Wang, Y., *Catalysis Today*, **2009**, 139, 4, 244-260.

11. Andreeva, D., *Gold Bull.,* **2002**, 35, 81-88.

12. Barakat,T., et al., *Energy Environ. Sci.,* **2013**, 6, 371–391.

13. Muradov N.Z., Veziroglu, T. N., *Int. J. Hydrogen Energy,* **2005**, 30, 225.

14. Dincer I., *Int. J. Hydrogen Energy*, **2012**,37, 1954-1971.

15. Acar C, Dincer I., *Int. J. Hydrogen Energy*, **2014**, 39, 1-12.

16. Parmuzina A. V., Kravchenko, O. V., *Int. J. Hydrogen Energy*, **2008**, 33, 3073.

17. Wang, H. Z., et al, Renew. Sust. Energ. Rev., **2009**, 13, 845.

18. Levin, D. B., Chahine, R., *Int. J. Hydrogen Energy*, **2010**, 35, 4962-4969.

19. Yilanci, A., Dincer, I., Ozturk, H.K., *Prog. Energy Combust Sci.*, **2009**, 35, 231-244.

20. Miltner, A., Wukovitz, W., Proll, T., Friedl, A., *J Clean Prod.*, **2010**, 18, 51-62.

21. Cruden, A., Mcdonald, J. R., *Int. J. Hydrogen Energy*, **2019**, 32(6), 705-709.

22. Bhandari, R., Trudewind, C.A., Zapp, P., *J Clean Prod.*, **2014**, 85, 151-163.

23. Rabbani, M., Dincer, I., Naterer, G.F., *Int. J. Hydrogen Energy*, **2014**, 39, 1941-1956.

24. Acar, C,, Dincer, I,, Zamfirescu, C., *Int J Energy Res.,* **2014**, 38, 1903-1920.

25. Dzaugis, M. E., Spivack, A. J., Radiation Physics and Chemistry, **2015**, 115, 127-134.

26. Shailendra, A. S., Arya, K., Biotechnology Report, **2017**, 15, 63-69.

27. Wang, Y., et al., *Nature Energy*, **2019**, **4**, 746–760.

28. Holladaym, J., D., Hu, J., King, D., L., Wang, Y., *Catal Today*, **2009**, 139, 244-260.

29. De Crisci, A. G., Moniri, A., Xu, Y., *Int. J. Hydrogen Energy*, **2019**, 44(3), 1299–1327.

30. Wang,Y., et al, *Int. J. Hydrogen Energy*, **2019**, 44, 12, 29680-29691.

31. Rand, D. A. J., Dell, R.,M., *Encycl Electrochem Power Sources*, **2009**, 276-292.

32. Si, R.; Flytzani-Stephanopoulos, M., *Angew. Chem*., **2008**, 120, 2926-2929.

33. Kipnis, M.; Volnina, E., *Appl. Catal. B*, **2010**, 98, 193-203.

34. Cohn, J. G. E., U.S. Patent 3216782, **1965**.

35. Li, B. D.; et al, *Catal. Today*, **2011**, 164, 74-79.

36. Shekhar, M., et al., *J. Am. Chem. Soc*., **2012**, 134,4700-4708.

37. Andreeva, D., et al, *Gold Bull.*, **2002**, 35, 81-88.

38. Sandoval, A., Gomez-Cortes, A., Zanella, R., Diaz, G., Saniger, J. M., *J. Mol. Catal. A*, **2007**,.278, 200–208.

39. Lenite, B. A., Galletti, C., Specchia, S., *Int. J. Hydrogen Energy*, **2011**, 36, 7750–7758.

40. Carter, J. H., and Hutchings, G. J., *Catalysts*, **2018**, 8, 627.

41. Quinet, E., Morfin, F., Diehl, F., Avenier, P., Caps, V., Rousset, J.-L., *Appl. Catal. B*, **2008,** 80, 195–201.

42. Grisel, R. J. H., Weststrate, C. J., Goossens, A., Craje, M. W. J., Van der Kraan, A. M., Nieuwenhuys, B. E., *Catal. Today*, **2002**, 72, 123–132.

43. Lakshmanan, P., Park, J. E., Kim, B., Park, E. D., *Catal. Today*, **2016.** 265, 19.

44. Lakshmanan, P., and Park, E. D., *Catalysts*, **2018**, 8, 183.

45. Lin, Q, et al, *Chem. Commun.*, **2014**, 50, 2721.

46. Torres Sanchez R.M., Ueda, A., Tanaka, K., Haruta, M., *J. Catal.*, **1997**, 168, 125.

47. Luengnaruemitchai A, Kim, D.T., Osuwan. S., Gulari, E., *Int. J. Hydrog. Energy*, **2005**, 30, 981.

48. Posada-Pérez, S., et al, *Catal. Sci*. *Technol*., **2017**, 7, 5332–5342.

49. Ma, Z., Tao, F., and Gu, X., Heterogeneous Catalysis at Nanoscale for Energy Applications, eds F. Tao, W. F. Schneider, and P. V. Kamat (Hoboken, NJ: John Wiley & Sons, Inc.), **2015**, 217–238.

50. Dong, J., Fu, Q., Jiang, Z., Mei, B., and Bao, X., *J. Am. Chem. Soc.*, **2018**, 140, 13808–13816.

51. Imai, H., Date, M., Tsubota, S., *Catal. Lett.*, **2008**, 124, 68.

52. Yang, Y.F., Sangeetha, P., Chen, Y.W., *Ind. Eng. Chem. Res.*, **2009**, 48,10402.

53. Sangeetha, P., Zhao, B., Chen, Y.W., *Ind. Eng. Chem. Res.*, **2010**, 49, 2096.

54. Beck, A., Horvath, A., Stefler, G., Scurrell, M., S., Guczi, L., *Top Catal.*, **2009**, 52, 912.

55. Chang, L., H., Chen, Y., W., Sasirekha, N., *Ind. Eng. Chem. Res.*, **2008**, 47, 4098.

56. Chen, Y., W., Chen, H., J., Lee, D., S, *J. Mol. Catal. A*, **2012**, 363-364, 470.

57. Delannoy L, et al, *Appl. Catal. B*, **2010**, 94,117.

58. Lakshmanan, P., *Catalysis Surveys from Asia*, **2014**, 18, 2–3, 75–88.

59. Reina, T. R., M., et al, *J. Catal.*, **2015**, 326, 161–171.

60. Wang, L. C., Widmann, D., and Behm, R., *J. Catal. Sci. Techn.*, **2015**, 5, 925–941.

61. Reina, T. R., Ivanova, S., Centeno, M. A., Odriozola, J. A., *Int. J*. *Hydrogen Energy,* **2015**, 40, 1782–1788.

62. Flytzani-Stephanopoulos, M., *Acc. Chem. Res.*, **2014**, 47, 783–792.

63. Song, W., and Hensen, E. J. M., *ACS Catal.*, **2014**, 4, 1885–1892.

64. Li, L., Song, L., Zhu, L. F., Yan, Z., and Cao, X. B., *Catal. Sci*. *Technol*., **2018**, 8, 1277-1287.

65. Haruta, M., Tsubota, S., Kobayashi, T., Kageyama, H., Genet, M.J., Delmon, B., *J. Catal.*, **1993**, 144, 175.

66. Schaefer, A., et al, *J. Phys. Chem. C*, **2012**, 116, 4564.

67. Kim, W., B., et al, *Angew Chem Int*, **2005**, 44, 778.

68. Haruta, M., *Gold Bull.*, **2004**, 37, 1–2, 27-36.

69. Zanella, R., Giorgio, S., Henry, C.R., Louis, C., *J. Phys. Chem. B.,* **2002**, 106, 7634.

70. Nechayev, Y. A., *Geochem. Int.* **1986**, *23*, 32.

71. Machesky, M., L.; Andrade, W., O.; Rose, A., W., *Geochim. Cosmochim. Acta,* **1991**, *5*, 769.

72. Yuan, Y., et al, *J.Catal*., **1997**, 170, 191.

73. Prati, L., Villa, A., *Catalysts,* **2012**, *2*, 24-37.

74. Veith, G., et al, *Catal. Today,* **2007**, *122*, 248–253.

75. Han, Y.-F.; Kahlich, M., J.; Kinne, M.; Behm, R., J. Phys. Chem. Chem. Phys., **2002**, 4, 389-397.

76. Kahlich, M., J.; Gasteiger, H., A.; Behm, R., J., *J. Catal.*, **1997**, 171, 93-105.

77. Sirijaruphan, A.; Goodwin, J., G., Jr.; Rice, R., W., *J. Catal.*, **2004**, 227, 547-551.

78. Schubert, M., et al, *Phys. Chem. Chem. Phys.*, **2001**, 3, 1123-1131.

79. Liu, K.; et at, *Ind. Eng. Chem. Res.*, **2011**, 50, 758-766.

80. Huang, Y. Q.; Wang, A., Q.; Li, L.; Wang, X., D.; Su, D. S.; Zhang, T., *J. Catal.*, **2008**, 255, 144-152.

81. Liu, K., Wang, A., Zhang, T., *ACS Catal.*, **2012**, 2, 1165-1178.

82. Valden, M., Lai, X., Goodman, D., W., *Science*, **1997**, 281, 1647–1650

83. Qiu, Z., Guo, X., Mao, J., Zhou, R., *Appl. Surf. Sci.*, **2019**, 481, 1072–1079.

84. Bus E., Miller J., T., Van Bokhoven, J., A., *J. Phys. Chem. B*, **2005**, 109:14581.

85. Quinet E., et al, *J. Catal.*, **2009**, 268, 384.

86. Saavedra, J., et al, *Nat. Chem.*, **2016**, 8, 584–589.

87. Silva, I. C, Investigação in situ da influência reversível da não-estequiometria sobre o perfil da banda Raman do óxido de cério, Master Dissertation, **2015**.

88. Yashima, M. Catalysis by ceria and related materials. London: Imperial College Press, **2013**. 2nd ed, p. 1-45

89. Yao, S. et al, *Phys. Chem. Chem. Phys.*, **2014**, 16,17183.

90. Fisher, T. J., et al, *Nanoscale*, **2019**, 11, 4552-4561.

91. Li, Z., Catalysis by ceria and related materials. London: Imperial College Press, **2013**. 2nd ed, p. 295-359.

92. Mai**,** H. X. et al, *J. Phys. Chem. B*., **2005**,109, 24380-24385.

93. Esmailpour, A. A., et al, *Catal. Sci. Technol.*, **2019**, 9, 5979.

94. Suda, A., et al*, J. Ceram. Society Japan*, **2004**, 112, 11, 581-585.

95. Senanayake, S. D., Rodriguez, J. A.; Stacchiola, D., *Topics in Catalysis.* **2013**, 56, 1488-1498.

96. Vantomme, A., Yuan, Z. Y., Du, G. H., Su, B. L., *Langmuir*, **2005**, 21, 1132.

97. Ren, Z.; Peng, F.; Li, J., Liang, X., Chen, B., *Catalysts*., **2017**, 7, 48.

98. Yao, S. Y. et al., *J. A.; Phys. Chem.,* **2014**, 16, 17183-17195.

99. Song, W., Hensen, E., *J. M., Catal. Sci. Technol.,* **2013**, 3, 3020-3029

100. Hirano, M., Kato, E., *J. Am. Ceram. Soc.,* **1999**, 82 (3), 786-788.

101. Li, J. et al, *J. Mater. Chem. A*, **2014**, 2, 16459-16466.

102. Wu, H. et al, *J. Chem. Mater,* **2019**, 317, 2263-2268.

103. Elger, A. K. et al, *ACS Sens.*, **2019**, 46, 1497-1501.

104. Xiao, Z., et al, *Applied Surface Science*, **2018**, 455, 1037–1044.

105. Jia, H., et al, *J. Am. Chem. Soc.,* **2019**, 14113, 5083-5086.

106. Zhang, Y. C., et al, *Appl. Cat. B Environm.*, **2018**, 224, 101-108.

107. Um N., et al. Zero-Carbon Energy Kyoto. Green Energy and Technology. **2010** *Springer*, Tokyo.

108. Beaudoux, X., Virot, M., Chave, T., Durand, G., *Green Chem.*, **2016**,18, 3656-3668.

109. Suter, D., Banwart, S., Stumm, W., *Langmuir*, **1991**, 7, 809.

110. Conesa, J. C., *Surf. Sci.*, **1995**, 339, 337.

111. Thommes, M., et al, *Pure Appl. Chem.* **2015**, 8-9.

112. Kanazawa,T., et al, *SAE Technical Paper*, **2003**, 01, 0811.

113. Reddy, B.M., Thrimurthulu, G., Katta, L, *Catal. Lett.* **2011**, 141, 572–581.

114. Reddy B.M., Katta, L., Thrimurthulu, G., *Catal. Today*, **2011**, 175, 585-592.

115. Abdollahzadeh-Ghom, S., Zamani, C., Andreu, T., Epifani M., Morante, J.R., *Appl. Catal. B.: Environ.* **2011**, 108, 32-38.

116. Uzunoglu, A., Zhang, H.Y., Andreescu, S., Stanciu, L. A., *J. Mater. Sci.*, **2015**, 50, 3750-3762.

117. Piumeti, M., et al, *Catalysts*, **2017**, 7, 174.

118. Taniguchi, T., et al, *J. Phys. Chem. C*, **2009**, 113, 19789–19793.

119. Corma, A. Garcia, H., *Chem. Soc. Rev.*, **2008**, 37, 2096-2126.

120. Wojnicki, M., et al., *Hydrometallurgy,* **2012**, 127, 43-53.

121. Hönes, G., Huisl, W., Keim, R., Schwager, B., *Gmelin handbook of inorganic and organometallic chemistry*, **1992**, 8th ed. Springer-Verlag.

122. Haruta, M., *Chem. Rec.* **2003**, 3, 75-87.

123. Parks, G. A., *Chem. Rev.*, **1965**, 652, 177-198.

124. Zanella, R., Delannoy, L., Louis, C., *Appl. Catal. A Gen.,* **2005,** 291**,** 65-72.

125. Young, C. L., Clever, H. L., *IUPAC Solubility Data Series*, Oxford, England, **1979-1981**.

126. Standard X-ray Diffraction Pattern, Data for 71 substances, National Bureau of Standard, **1984**, JCPDS, *Library of Congress*, 53-61386, Washington, D.C.

127. Zhang, H., et al, *Front. Chem.,* **2019**, 7, 436.

128. Liang, J., et al, *Nanophotonics*, **2019**, 8(5), 771–786.

129. Prabaharan, D., M., D., M., et al, *Materials Research.,* **2016**; 19(2): 478-482.

130. Zhang, C. Michaelides, A., Jenkins, S. J., *Phys. Chem. Chem. Phys.*, **2011**, **13**, 22–33.

131. Tiancun, X., et al, *Catalysis Letters*, **1992**, 12, Issue 1–3, 287–29.

132. Pozdnyakova O., et al, *J. Catal.* **2006**, *237*, 1–16.

133. Koo, K. Y., Jung, U. H., Yoon, W. L., *Int. J. Hydrogen Energy*, **2014**, *39*, 5696-5703.

134. Widmann, D., et al, *ACS Catal.*, **2016**, 6, 5005−5011.

135. Valden, M.; Lai, X.; Goodman, D. W., *Science*, **1998**, 281, 1647–1650.

136. Laoufi, I., et al, *J. Phys. Chem. C*, **2011**, 115, 4673–4679.

137. Zanella, R., Dellanoy, L., Louis, C., *Applied Catalysis A: General*, **2005**, 291, 62–72.

7. APPENDIX – MICROSCOPY IMAGES

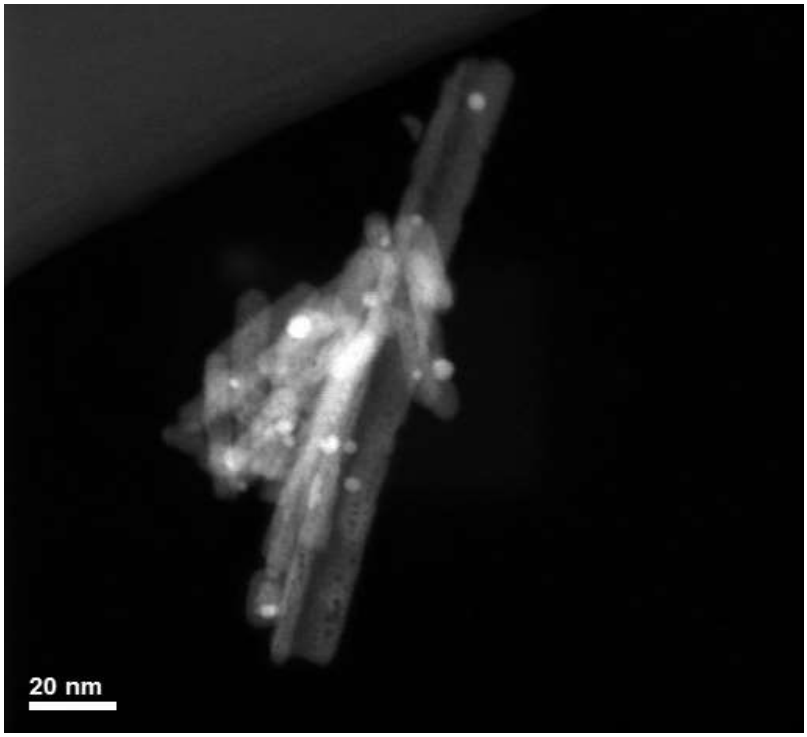

(a)

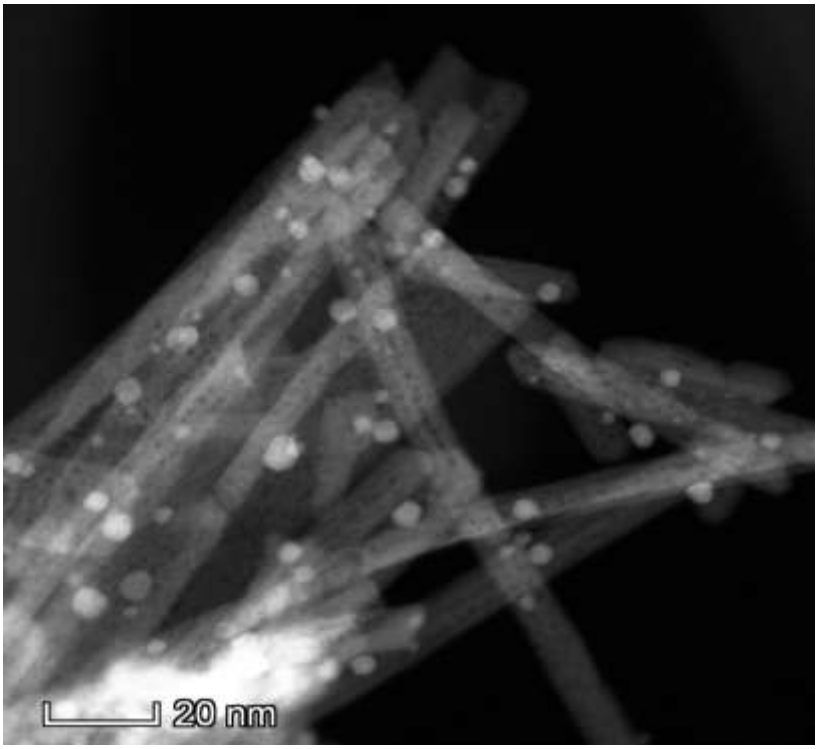

(b)

Figure 42. HAADF HRTEM images for sample Cat1 (NRCeO2_NaOH_573) (a) before and (b) after the catalytic test.

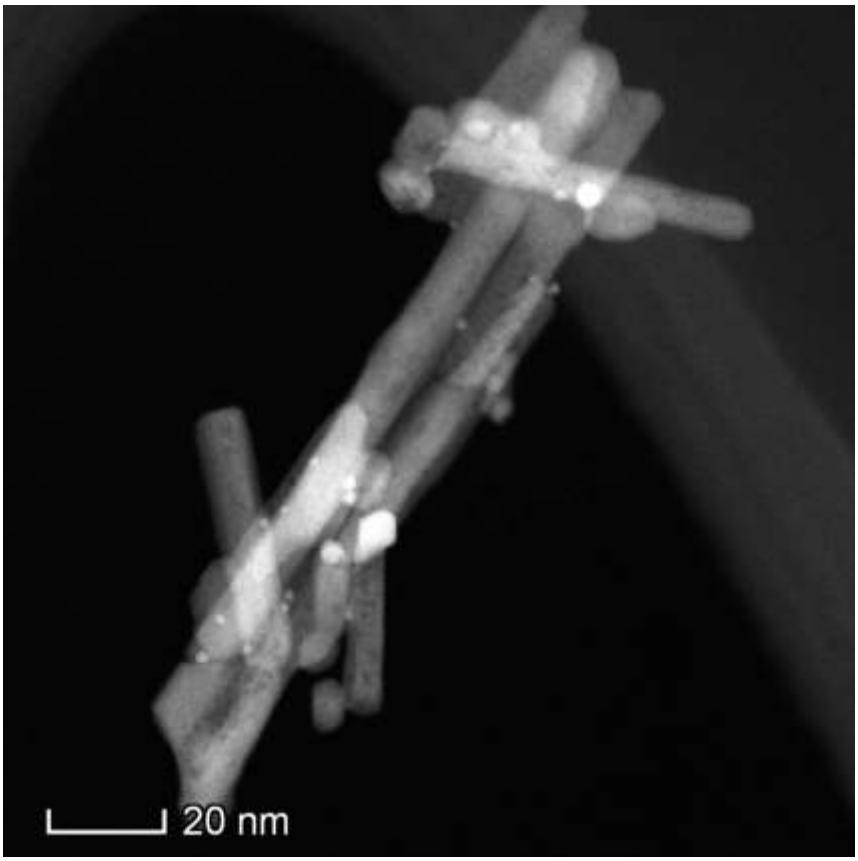

(a)

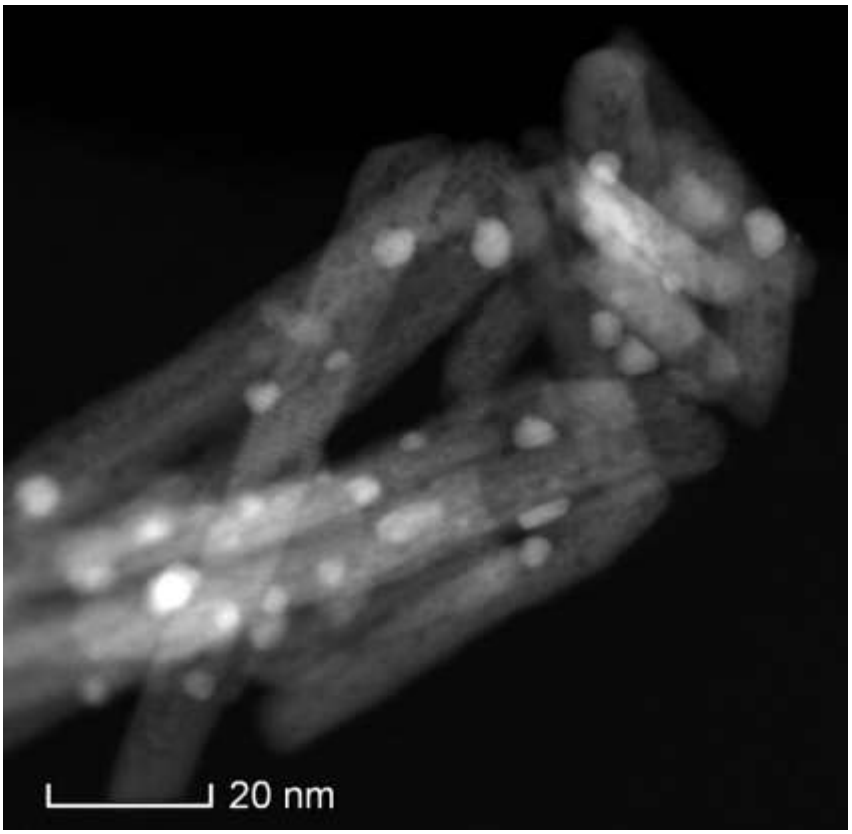

(b)

Figure 43. HAADF HRTEM images for sample Cat2 (LNRCeO2 _NaOH_573) (a) before and (b) after the catalytic test.

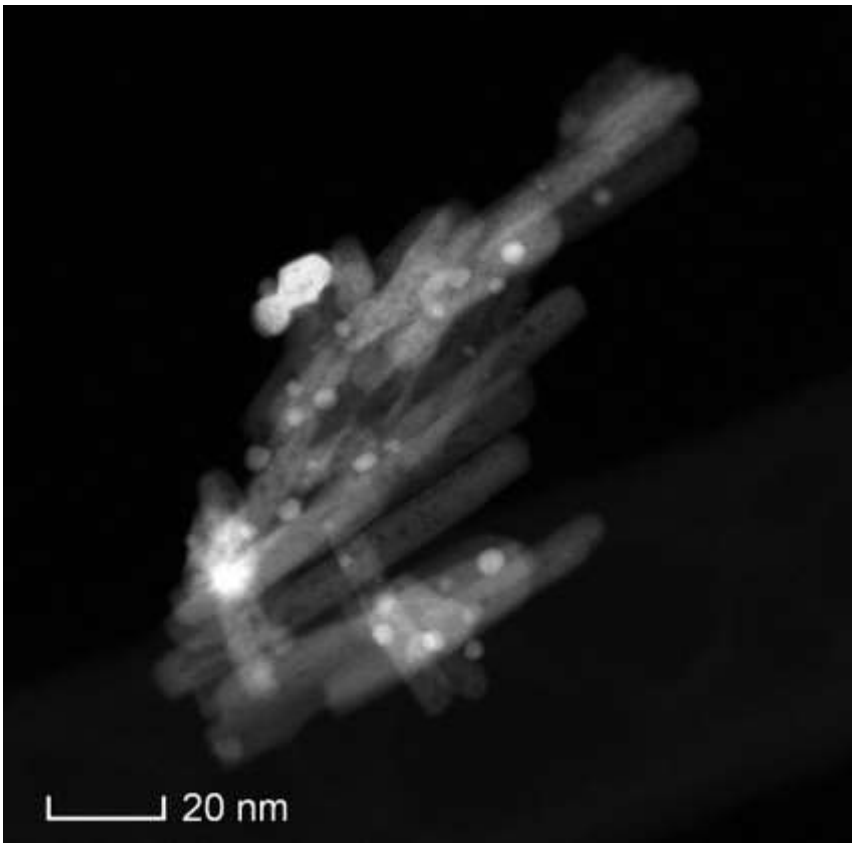

(a)

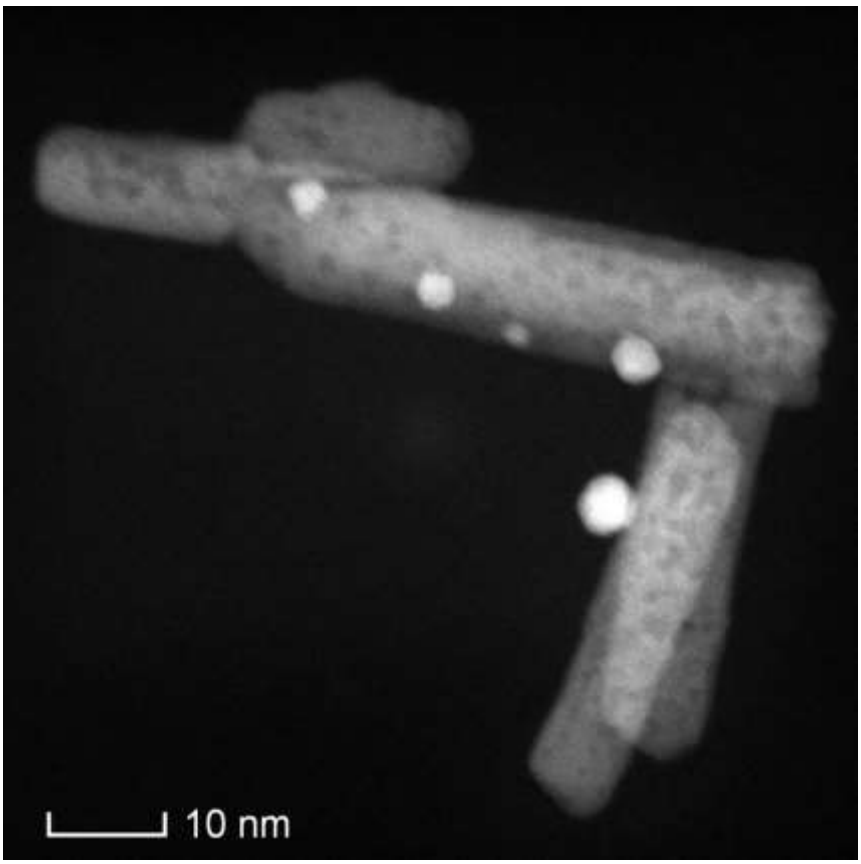

(b)

Figure 44. HAADF HRTEM images for sample Cat3 (NRCe0.8Zr0.2O2_NaOH_573) (a) before and (b) after the catalytic test.

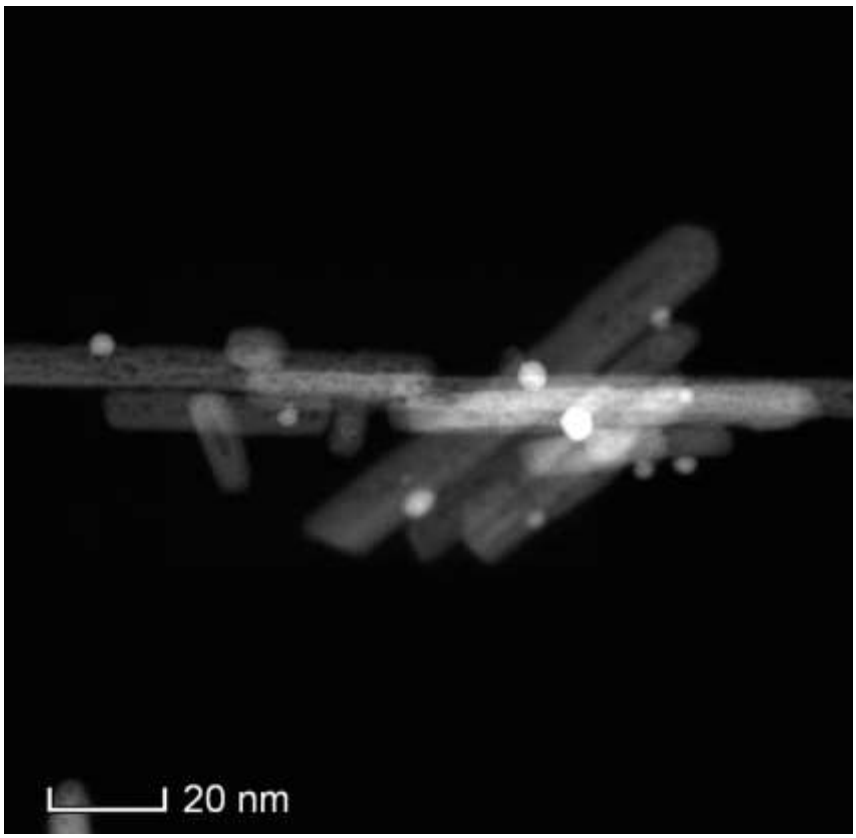

(a)

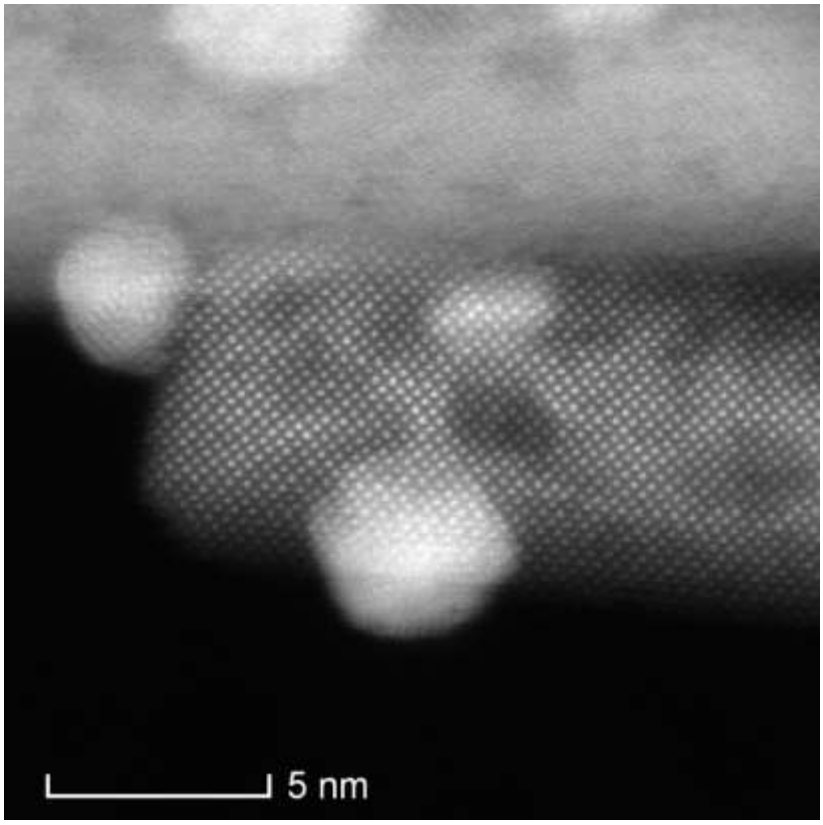

(b)

Figure 45. HAADF HRTEM images for sample Cat4 (LNRCeO2_urea_573) (a) before and (b) after the catalytic test.

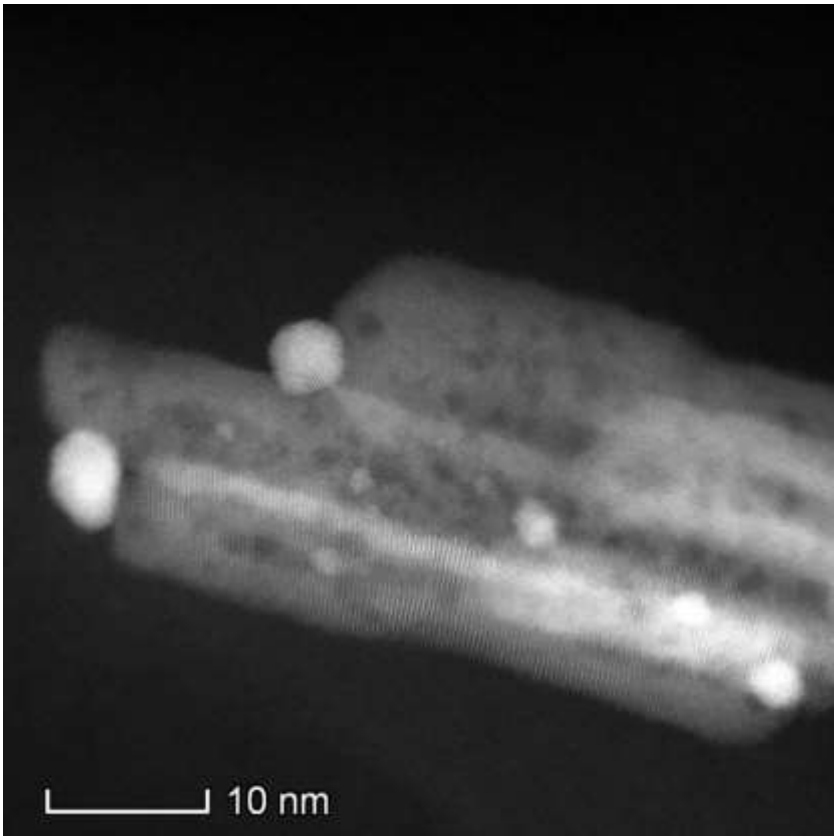

(a)

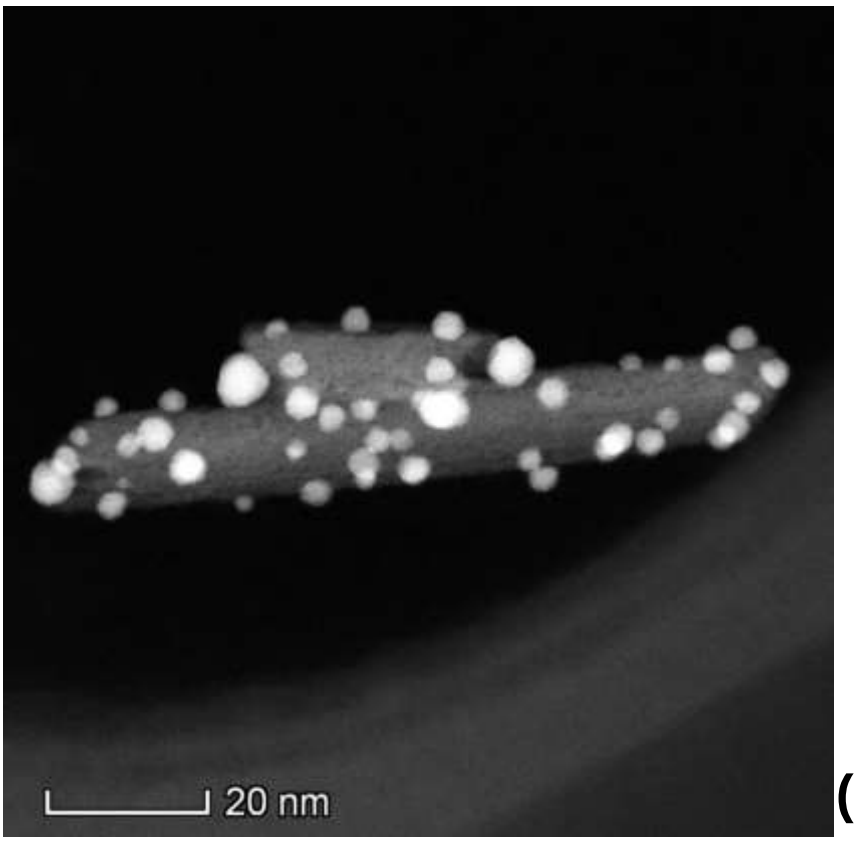

(b)

Figure 46. HAADF HRTEM images for sample Cat5 (LNRCeO2_NaOH_673)) (a) before and (b) after the catalytic test.